National and Kapodistrian University of Athens

Department of Astrophysics, Astronomy and Mechanics
Faculty of Physics

A thesis submitted for the degree of Doctor of Philosophy

Dusty Massive Stars in the Local Group

Mikola Britavskiy

Thesis Supervisors : **Prof. Despina Hatzidimitriou**
Dr. Alceste Z. Bonanos
Dr. Panos Boumis

Athens, January 2016

PhD Thesis

Dusty Massive Stars in the Local Group

Thesis Author : Mikola Britavskiy

Thesis Committee : Prof. Despina Hatzidimitriou
Dr. Alceste Z. Bonanos
Dr. Panos Boumis
Dr. Manolis Xilouris
Prof. Stelios Kazantzidis
Prof. Kanaris Tsinganos
Prof. Andreas Zezas

Contents

Abstract

The role of episodic mass loss in massive star evolution is one of the most important open questions of current stellar evolution theory. Episodic mass loss produces dust and therefore causes evolved massive stars to be very luminous in the mid-infrared and dim at optical wavelengths. Star forming dwarf irregular (dIrr) galaxies serve as ideal laboratories for investigating the evolution and mass loss phenomenon of red supergiants (RSGs), supergiants B[e] (sgB[e]), and luminous blue variables (LBVs) within the context of different metallicities of host galaxies. Also, RSGs may be used for abundance determinations in dIrrs. The extremely low number of spectroscopically confirmed RSGs and other types of dusty massive stars mentioned before, in external galaxies makes the identification of new stars of these types statistically significant. Increasing the statistics of spectroscopically confirmed evolved massive stars in the Local Group enables the investigation of the mass loss phenomena that occur in these stars in the late stages of their evolution.

We aim to complete the census of luminous mid-IR sources in star-forming dwarf irregular galaxies of the Local Group. To achieve this we employed mid-IR photometric selection criteria to identify evolved massive stars, such as RSGs and luminous blue variables (LBVs), by using the fact that these types of stars have infrared excess due to dust. The method is based on 3.6 μm and 4.5 μm photometry from archival *Spitzer* Space Telescope images of nearby galaxies and $J-$band photometry from 2MASS. We applied our criteria to 7 dIrr galaxies: Pegasus, Phoenix, Sextans A, Sextans B, WLM, IC 10 and IC

1613 selecting 124 point sources, which we observed with the VLT/FORS2, GTC/OSIRIS and duPont/WFCCD spectrographs in multi-object and long-slit spectroscopy modes.

We identified 28 RSGs, of which 21 are new discoveries, also 2 new emission line stars, and 8 carbon stars. Among the other observed objects we identified foreground giants, and background objects, such as a quasar and an early-type galaxy that contaminate our survey. We use the results of our spectroscopic survey to revise the mid-IR and optical selection criteria for identifying RSGs from photometric measurements. The optical selection criteria are more efficient in separating extragalactic RSGs from foreground giants than mid-IR selection criteria, however the mid-IR selection criteria are useful for identifying dusty stars in the Local Group. For some of the newly identified RSGs we measured the fundamental physical parameters by fitting their observational spectral energy distributions with MARCS stellar atmosphere models. This work serves as a basis for further investigation of the newly discovered dusty massive stars and their host galaxies.

This PhD thesis is organized as follows: Chapter 1 provides the scientific context of the present study. In Chapter 2 the procedure for selecting sources is presented. Descriptions of the observations and data reduction are presented in Chapter 3. Chapter 4 is devoted to the spectral analysis and the spectral type classification of the obtained spectra. Chapter 5 is devoted to presenting and discussing the results. Conclusions and future perspectives of the PhD thesis work are presented in Chapter 6. In Chapter 7 the acknowledgments and list of supporting materials (published papers, information about allocated telescope time, etc.) are presented.

Chapter 1

Introduction

The episodic mass loss phenomenon in evolved massive stars plays a critical role in stellar evolution theory. The upper limit to the masses of stars is thought to be $\sim$150 $M_\odot$ (Figer 2005; Oey & Clarke 2005), or as recently proposed, to be $\sim$300 $M_\odot$ (Crowther et al. 2010; Banerjee et al. 2012), the observed masses of carbon-rich Wolf-Rayet stars, the predicted endpoints of their evolution (see Georgy et al. 2012), do not exceed 20 $M_\odot$ (see review by Crowther 2007). Therefore, one or more mechanisms must cause these stars to shed very large amounts of mass in a very short time (e.g. episodic mass loss, binary evolution). The importance of investigating massive stars, especially dusty massive stars, comes from the observed phenomenon of episodic mass loss, which complicates modeling the evolution of these objects (Smith 2014). Classical line-driven wind theory (Kudritzki & Puls 2000), once thought to describe the mechanism responsible for removing the envelopes of massive stars, has been shown to be inadequate, both on theoretical grounds (due to wind clumping; Owocki & Puls 1999) and estimations based on spectral lines (Fullerton et al. 2006), which require reductions in the mass-loss rates by factors of 10 – 20. The phenomenon of episodic mass-loss is the common characteristic for 3 types of massive stars: red supergiants (RSGs), luminous blue variables (LBVs) and supergiants B[e] (sgB[e]).

The importance of episodic mass loss in massive stars has also come to the forefront in the (core-collapse) supernova community, following discoveries that emerged from recent untargeted supernovae searches and amateur surveys. These searches have established the new classes of luminous core-collapse supernovae (with $M_V < -20$ mag; Smith et al. 2007) and optical transients with luminosities intermediate between novae and supernovae (e.g. Prieto et al. 2008; Bond et al. 2009). In both cases, the presence of circumstellar material is inferred, implying a central role of episodic mass loss in the evolution of massive stars. The overluminous Type IIn SN 2010jl is a well-studied example of the first class, with a massive progenitor star of >30 $M_\odot$ surrounded by a dense circumstellar shell (Smith et al. 2011; Zhang et al. 2012; Ofek et al. 2014), which exploded in a low-metallicity galaxy (Stoll et al. 2011). Neill et al. (2011) and Stoll et al. (2011) have presented tantalizing evidence that overluminous supernovae occur in low-metallicity host galaxies, implying that such supernovae dominated the metal-poor early Universe. Furthermore, there is evidence for mass-loss rates as high as $\approx 10^{-2}$ $M_\odot$ yr^{-1} in Type IIn supernovae (Kiewe et al. 2012; Fox et al. 2013). SN 2008S, a well-studied example of the class of intermediate-luminosity optical transients, was found to have a dust-enshrouded progenitor (8 – 10 $M_\odot$; Prieto et al. 2008) in pre-explosion *Spitzer* images of the host galaxy NGC 6946. Late time imaging reveals that it is ≈15 times fainter than the progenitor in the mid-IR and is undetected in the optical and near-IR (Adams et al. 2015). Finally, the case of SN 2009ip involves a 50 – 80 $M_\odot$ progenitor that underwent episodic mass loss. The final activity included a series of eruptions in 2009 and 2010 until its last observed explosion in August-September 2012, which resembled a Type IIn supernova (e.g. Mauerhan et al. 2013; Pastorello et al. 2013; Smith et al. 2013).

The supernovae and transients described above strongly suggest that episodic mass loss in massive stars is central to their evolution and has significant implications for the enrichment of the interstellar medium and the chemical evolution of the early Universe. We have therefore initiated a survey that aims to provide a census of stars that have undergone episodic mass loss by studying luminous mid-IR sources in a number of nearby galaxies (Khan et al. 2010, 2011, 2013). The ultimate goal of the survey is to investigate the role of episodic mass loss in massive stars, by using the fact that (a) episodic mass loss in evolved massive stars produces dust and therefore causes these sources to be very luminous in the mid-infrared, and (b) there are abundant archival *Spitzer* images of nearby galaxies for which the infrared stellar population remains unexplored.

In this work, we take advantage of mid-IR photometry from *Spitzer* archival data and the "roadmap" provided by Bonanos et al. (2009, 2010) for interpreting luminous, massive, resolved stellar populations in nearby galaxies. These works studied 1268 and 3654 massive stars with known spectral types in the Large Magellanic Cloud (LMC) and Small Magellanic Cloud (SMC), respectively, and found that the brightest mid-IR sources in the LMC and SMC are luminous blue variables, red supergiants, and supergiants B[e], according to their intrinsic brightness and because they are surrounded by their own dust (see Chapter 2).

The first attempt to define the selection criteria for identifying dusty massive stars in nearby galaxies in the mid-infrared was described in Britavskiy et al. (2014) (Paper I). As a result of this work 5 new RSGs from 8 selected candidates in the dIrr galaxies Sextans A and IC 1613 were spectroscopically confirmed, providing evidence of the success of mid-IR selection criteria for dusty massive stars. In the next study, Britavskiy et al. (2015) (Paper II) identified 13 RSGs, of which 6 are new discoveries, also 2 new emission line stars, and 1 candidate yellow supergiant. These two studies form the base of this PhD Thesis, see the Appendix for more information about these papers and the papers that are in preparation. The work which is in preparation is devoted to finalizing census of RSGs in IC 10, IC 1613, and Sextans B dIrr galaxies, together with a determination of fundamental parameters of all RSGs that have been identified in these papers.

The first step in the identification of such rare stars is found in the selection process of these types of objects from photometric catalogs. A systematic search for massive stars in the Local Group became possible with the availability of high quality *BVRI* photometry. Massey et al. (2006, 2007c) presented optical photometry for seven star-forming dIrrs (IC 10, NGC 6822, WLM, Sextans B, Sextans A, Pegasus, and Phoenix), M31 and M33, which served as a basis for further works devoted to the identification of new RSGs (Massey et al. 2009; Levesque & Massey 2012; Drout et al. 2012; Levesque 2013), LBVs (Massey et al. 2007b; Humphreys et al. 2014; Kraus et al. 2014), and Wolf-Rayet stars (WR, Neugent & Massey 2011) in these galaxies. In all these listed works the selection of targets was based on optical *BVRI* photometry, however, deep optical surveys exist for a small number of dIrrs. Moreover, dusty stars appear brighter in the infrared rather than in optical colors as they exhibit infrared excess. Thus, infrared surveys should, in principle, provide advantages to identifying these types of stars.

This fact can be seen in the example of the two largest galaxies of the Local Group, besides the Milky Way, M31 (D=0.78 Mpc, Stanek & Garnavich 1998) and M33 (D=0.96 Mpc, Bonanos et al. 2006) which have been extensively observed across many wavelengths, including the mid-IR by *Spitzer*. Both galaxies were also observed in the optical as part of the Local Group Survey (Massey et al. 2006), which made public deep multi-band images and *UBVRI* stellar catalogs of 371,781 and 146,622 stars in M31 and M33, respectively. Thompson et al. (2009) used the Spitzer data to search for sources similar to the progenitors of the SN 2008S and the NGC300 transients (see Prieto et al. 2008; Bond et al. 2009). They found that more luminous, but less red sources, although rare, are present in larger numbers (see Figure 1.1), in some cases corresponding to already spectroscopically (optically) classified LBVs and other stars. However, many of the most luminous mid-IR sources in M33 were not previously recognized because they are faint in optical colors. The two M33 objects "closest" to η Car (Humphreys & Davidson 1994) in the mid-IR CMD published by Thompson et al. (2009), one is the known compact, young star cluster IC 133 (spatially unresolved by *Spitzer*, but immediately recognized by its mid-IR SED-too cold to be a point source), but the other one, which was called "Object X", is the brightest mid-IR point source in all of M33 and the subject of Khan et al. (2011).

In the next 3 sections we present an overview for each type of dusty massive star, with highly possible episodic mass-loss phenomena, which we targeted in this thesis.

1.1 Red supergiants

The RSGs are among the most numerous and luminous mid-IR populations of the massive stars family, and have some of the highest mass-loss rates observed in stars (e.g. VY CMa, 2×10^{-4} $M_{\odot}$ yr^{-1}; Danchi et al. 1994). In the final stages of evolution, RSGs lose a significant fraction of their mass at rates $\dot{M} \sim 10^{-3}$ to 10^{-6} $M_{\odot}$ yr^{-1} (Jaeger et al. 1988; van Loon et al. 2005; Mauron & Josselin 2011a). For a long time RSGs were found to have lower temperatures and higher luminosities than predicted by the Geneva evolutionary models (Massey 2003; Massey & Olsen 2003); however, this disagreement was apparently solved by using the modern MARCS model atmospheres (Levesque et al. 2005). The improvement was based on the new treatment of the opacity of molecular bands (e.g. TiO), which are dominant in the optical region of M- and K-type stars. However, Davies et al. (2013) reappraised the temperatures of red supergiants in the Magellanic Clouds, finding temperatures from TiO lines to be systematically lower by several hundred Kelvin than those derived from the continuum or integrated fluxes. These authors concluded that the TiO bands do not provide reliable temperatures of RSGs at low metallicities and that their temperatures are higher than previously thought.

The mean spectral type of a RSG in a galaxy is a function of metallicity, as first reported by Elias et al. (1985) and confirmed by recent studies (e.g. Levesque et al. 2006; Levesque & Massey 2012). This effect is mainly due to the shift of the Hayashi limit to warmer temperatures with decreasing metallicity. In addition, at lower metallicities, the TiO bands are weaker, yielding earlier spectral types. The investigation of RSGs in the Local Group spans the following galaxies: M33 (Drout et al. 2012; Massey 1998), the

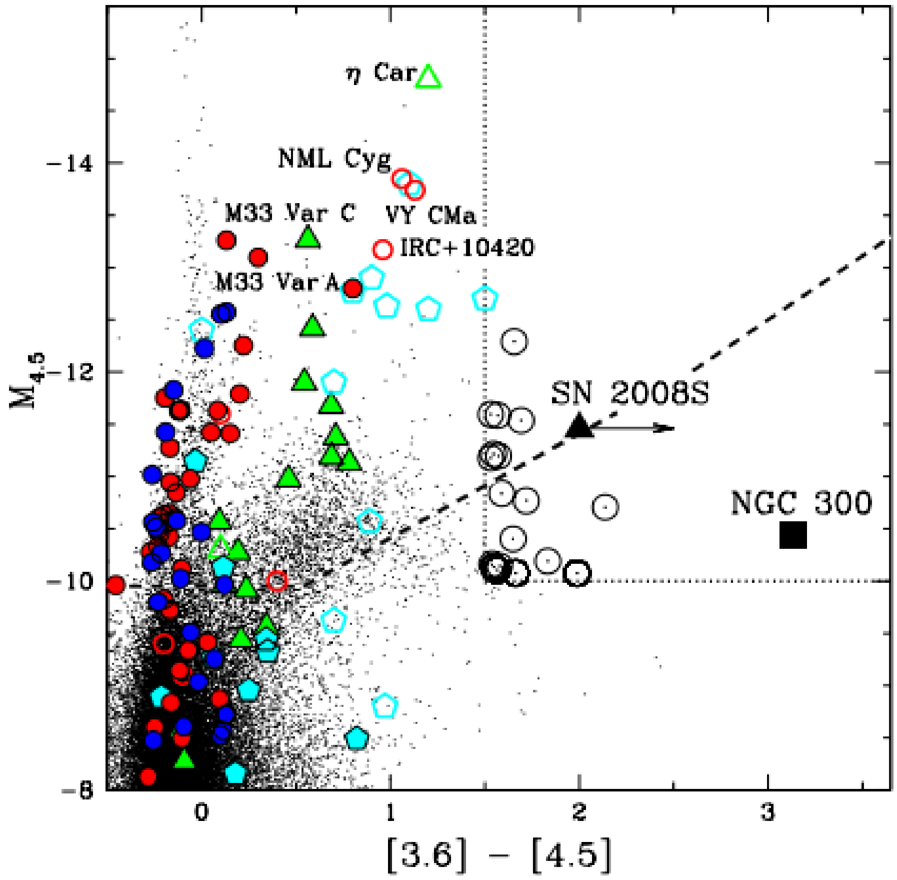

Figure 1.1: The $M_{4.5}$ magnitude versus [3.6] – [4.5] CMD of stars in M33 (small points) taken from Thompson et al. (2009). The circled points in the region isolated by the dotted lines are the closest analogs in M33 to the SN2008S (black triangle) and NGC 300 (black square) progenitors. Outside this region, filled symbols are optically-selected stars in M33 from Massey et al. (2006) and open symbols are Galactic stars. Green triangles, cyan pentagons and red circles are LBV stars (including outbursts like η Carina), WR stars, and RSGs/cool hypergiants, respectively.

Magellanic Clouds (Massey & Olsen 2003), M31 (Massey 1998; Massey et al. 2009), and WLM (Levesque & Massey 2012). All these works concluded that we have to increase the statistics of identified RSGs at a range of metallicities, because these stars are one of the keys for improving evolutionary models of the late stages of massive stars. Recent works have selected candidate RSGs using optical criteria, mainly from $B-V$ and $V-R$ indices (see Section 4). In this work, we explore mid-IR selection criteria for RSGs and other types of dusty evolved massive stars. The first mid-IR studies of red supergiants date back half a century (Danielson et al. 1965; Johnson 1967), but it was not until the *Spitzer* era when systematic studies of the most luminous mid-IR populations (Buchanan et al. 2006; Kastner et al. 2008) and of extreme dust-enshrouded massive stars (Khan et al. 2010, 2013; Thompson et al. 2009) began. The present work differs in the mid-IR bands used, because we aim to provide selection criteria for RSGs and other obscured massive stars that can be applied to archival *Spitzer* data that are available for a large number of nearby galaxies (e.g. from SINGS; Kennicutt et al. 2003).

1.2 B[e] supergiants

Supergiant B[e] stars, or stars showing the B[e] phenomenon (Allen & Swings 1972, 1976), are a distinct class of B-type stars exhibiting forbidden emission lines (e.g. $[FeII]$, $[OI]$) with log $L/L_\odot > 4.0$. They are thought to be surrounded by dusty equatorial tori, making them bright IR sources, while gas in these tori give rise to forbidden emission lines. A two-component wind model with a hot polar wind and a slow, cool equatorial disk wind has been proposed to explain them (Zickgraf et al. 1985) but theoretical models of the disk have so far achieved limited success (Porter 2003; Kraus et al. 2007; Zsargó et al. 2008).

The optical spectra of these objects typically display strong Balmer line emission, together with emission of low-ionized metals from both permitted and forbidden transitions,

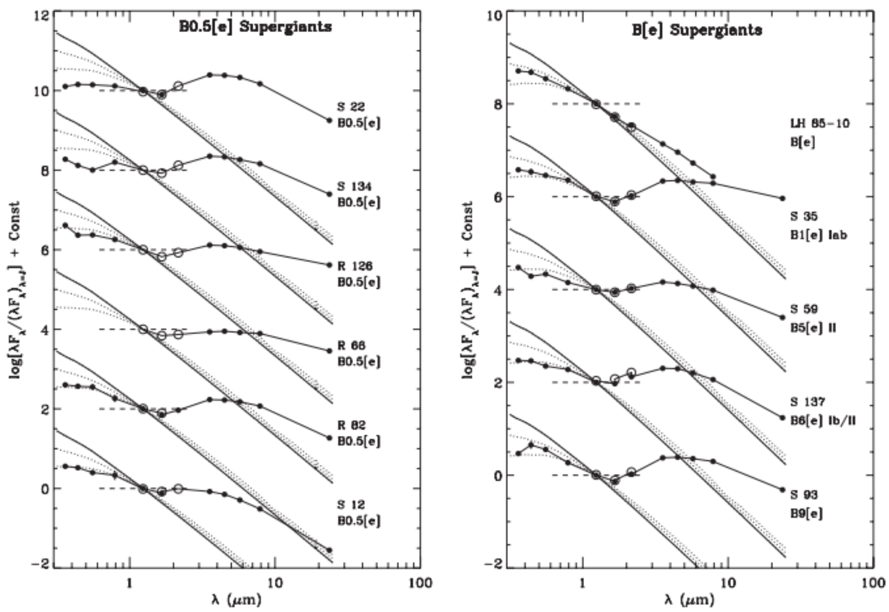

Figure 1.2: Representative SEDs of 11 sgB[e] stars in the LMC, normalized by their J-band fluxes (dashed line) and offset for display purposes (from Bonanos et al. 2009). The MCPS, IRSF, and SAGE measurements are shown as filled circles; the 2MASS and OGLE measurements as open circles. Infrared excesses are detected in most stars.

and a strong mid-infrared excess. Examples of SEDs of 11 known sgB[e] in the LMC are presented in Figure 1.2 (from Bonanos et al. 2009). The mid-IR "bump", or mid-IR excess between 8 and 24 μm, serves as a sign of sgB[e] stars. In general, there are known 5 B[e] supergiants in the Milky Way (Zickgraf 1998), 12 in the LMC (Bonanos et al. 2009), 7 in the SMC (Bonanos et al. 2010).

Supergiant B[e] stars and LBVs are located in a similar region on the Hertzsprung-Russell (HR) diagram (see Figure 1.3), yet the existence of an evolutionary connection remains unclear.

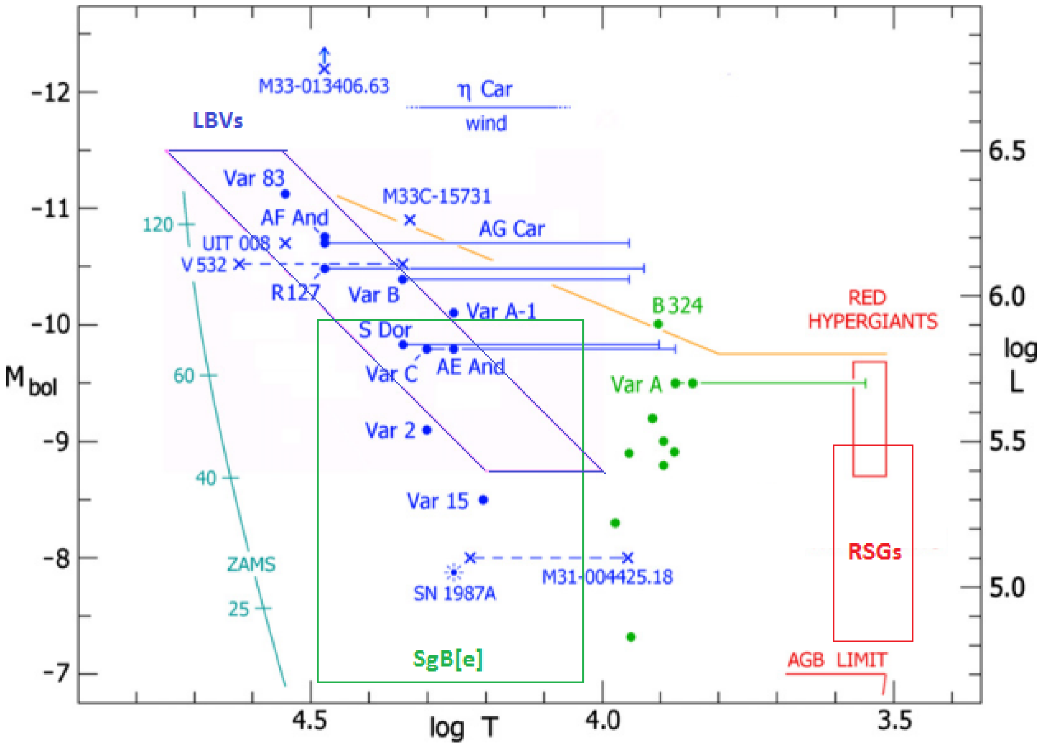

Figure 1.3: Schematic HR diagram (from Humphreys et al. 2014) comparing the position of LBVs (blue shape), sgB[e] (green shape), and RSGs (red shape) regions. Positions of known LBVs (blue dots) and post-red supergiants candidates (green dots) are taken from Humphreys et al. (2014).

1.3 Luminous blue variables

Luminous Blue Variables (LBV) are some of the most massive stars in one of the final stages of evolution, which suffer irregular eruptions (Humphreys & Davidson 1994). This class of stars was first defined by Conti (1984) and they are among the rarest of stars - only about 40 stars are known in the Local Group. The position of bona-fide LBVs on the HR diagram is illustrated in Figure 1.3 (Humphreys et al. 2014). LBVs are a rare class of luminous stars which undergo episodic mass loss and represent a transitional phase between the most massive O stars and the WR stage (Langer et al. 1994). Smith & Tombleson (2015) suggest that LBVs are products of binary evolution, however, they are found as isolated objects, without a second component. Namely, LBVs are likely the mass gainers in binary Roche Lobe overflow, because their ages and initial masses disagree with the stars around them.

The archetype LBVs in the Milky Way are the stars η Carinae and P Cygni. Observations of nebulae around these stars reveal very high ejecta masses, of order 10 $M_{\odot}$, and evidence of multiple ejections on the timescales of order 10^3 yr. LBV eruptions might be crucial for the evolution of massive stars but the LBV mass loss mechanism remains unknown. Massive shells of $0.01 - 20$ $M_{\odot}$ around LBVs indicate that these stars expel a large fraction of their initial mass in only a few years. There is also growing evidence that LBV-like eruptions can precede SNe Type IIn (e.g., SN 2005gj, SN 2005gl, SN 2006jc). The best studied LBV stars in the Milky Way are AG Car, P Cygni, HR Car, and in the LMC are S Dor and R71. The optical spectra of this type of object typically show prominent emission lines of H, He I, Fe II, very often with "P Cygni" line profiles. The P Cygni profiles are asymmetric profiles with broad wings, and double or split hydrogen emission lines, which are all indicators of winds, mass loss and outflows. LBVs are rare enough, and this short evolutionary phase of massive stars is poorly constrained observationally. There are known 10 LBVs in Milky Way, 16 in LMC, 2 in SMC, 4 in M31, 6 in M33.

Thus it's extremely important to expand the sample of known LBVs in the Local Group. This fact is one of the motivating factors of this PhD Thesis.

1.4 Stellar mass loss mechanism

Mass loss ($\dot{M}$) serves as an one of the main drivers of the evolution of massive stars. The role of this phenomenon is significant and there is no reliable theory how to take it into account in a stellar evolutionary models. During their lifetime, massive stars may lose up to 90% of their initial mass through stellar winds (Maeder & Meynet 1991). Stellar wind, especially a stellar wind of massive stars, is explained by intense stellar radiative output, i.e. high photon momentum that can drive stellar material to the circumstellar medium. This strongly impacts their internal structure and their evolution. Meynet et al. (2015) showed that changing the mass loss rate by a factor of ten only in the red supergiant phase can significantly affect the end point of stellar evolution. A star may become a supernova either as a red or as a blue supergiant depending on the mass loss history in the red supergiant phase.

According radiation driven wind theory, the resulting mass loss should be scaled with a power of the luminosity. Because no physical model exists, diverse empirical parameterizations are used in stellar evolution codes for estimating $\dot{M}$ as a function of basic stellar characteristics, i.e. mass, luminosity, and effective temperature. An important example is the empirical law built by de Jager et al. (1988). The formulation that was presented later by Nieuwenhuijzen & de Jager (1990) for this law is described by the formula:

$log\dot{M} = -7.93 + 1.64 \times logL + 0.16 \times logM - 1.61 \times log(T_{eff})$.

This law was based on observational estimates of $\dot{M}$ for stars located over the whole H-R diagram, including 15 RSGs (Mauron & Josselin 2011b). Typical values of mass loss rates for RSGs are 10^{-7} - 10^{-4} $M_{\odot}$ yr^{-1}. Figure 1.4 presents the Jager law together with well-known galactic RSGs, where the fact that more luminous stars have on average

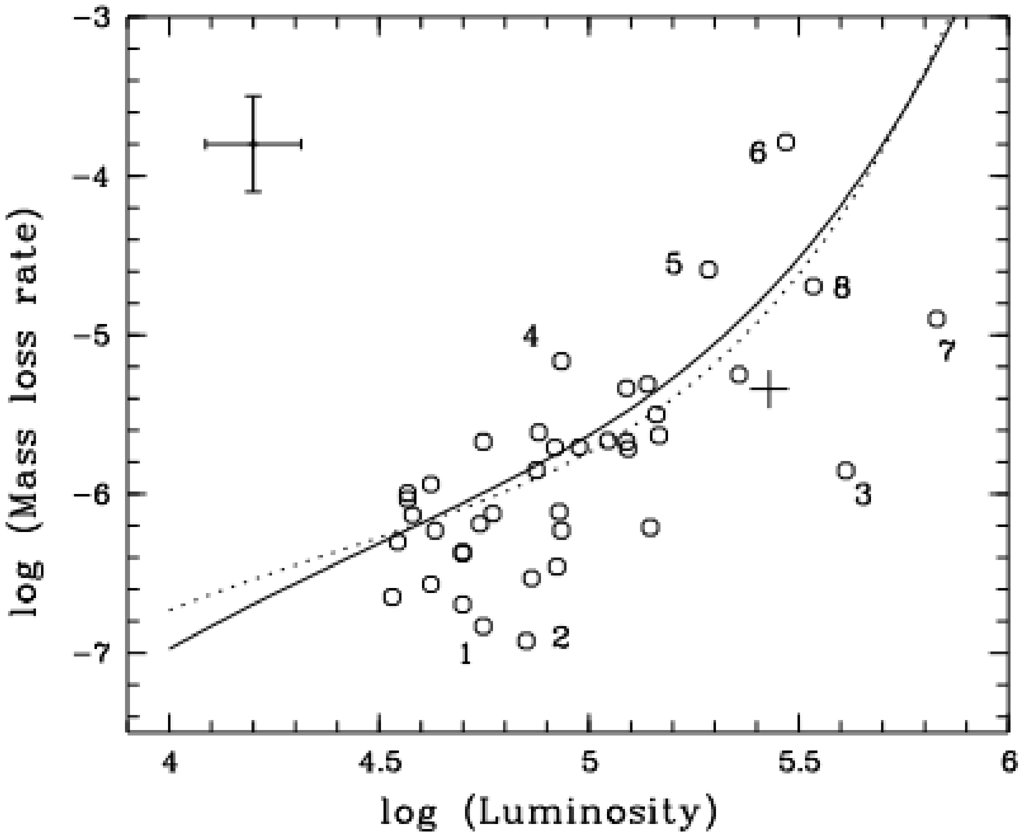

Figure 1.4: Comparison of de Jager rate (taken from Mauron & Josselin 2011b, plotted for T_{eff} = 3500 K and 4000 K) with mass-loss rates of 39 RSGs. The mass-loss rates are based on the study of dust and obtained with Jura's formula. The labels indicate a few well known RSGs as follows: 1: α Ori; 2: α Sco, 3: μ Cep, 4: S Per, 5: PZ Cas, 6: VY CMa, 7: EV Car, 8: VX Sgr. The small cross represents EV Car if a smaller distance of 2.5 kpc is adopted. At the upper left corner, error bars represent uncertainties of ±30 percent in luminosity, and a factor of ±2 in $\dot{M}$.

higher mass loss rates, is confirmed observationally. However, taking into account a large discrepancy in the prediction of the mass loss rates for each individual RSG, according to this Figure, the theory of mass loss rates of red supergiants remain poorly constrained empirically, not to mention that there are no theoretical models of the mass loss mechanism.

Concerning the LBV phase, mass-loss rates characterized by values $\approx 10^{-5}$ - 10^{-3} $M_{\odot}\ yr^{-1}$, associated with visual/near-IR spectroscopic and photometric variabilities. The episodic mass loss phenomena for such kind of stars have $\dot{M} \geq 10^{-2}\ M_{\odot}\ yr^{-1}$.

The occurrence of this phase during the massive stars evolution and the mass-loss mechanism are still not well understood, mostly because of the rarity of LBVs in our Galaxy. However, some systematic works (e.g. Vink et al. 2002, Owocki 2004) describing the "quiescent" phase of mass loss, show that the dominant driving mechanism of LBV winds is radiation pressure on spectral lines (line-driven mechanism). Which in turn, depends on effect of stellar rapid rotation, and the magnetic field of the star (e.g. Sundqvist et al. 2012b). For the large mass loss eruptions i.e. episodic mass loss phenomena, the theoretical modeling is absent due to unknown and unpredictable nature of such events during the LBV phase. One of the scenario suggested by Smith & Owocki (2006), that large mass eruptions occurs by continuum-driven mechanism.

Chapter 2

Target selection

2.1 Dwarf irregular galaxies

The Local Group includes the Milky Way, M31, their satellites, and their neighbors, but it is ever expanding to include the far richer sample of objects that fall within the loosely defined part of the universe referred to the Local Volume (McConnachie 2012). The Local Group comprises more than 54 galaxies, the overwhelming majority of nearby galaxies are dwarf galaxies (see Figure 2.1).

According to McConnachie (2012), dwarf galaxies, based on their morphological and star formation history properties, are divided into dwarf spheroidals (dSphs), dwarf irregulars (dIrrs), and transition (dIrr/dSph) galaxies. However, only dIrrs are gas rich and show evidence of H II regions that are sites of current massive star formation. Local Group dIrrs galaxies with high star-formation rates ($\gtrsim 0.003\ M_{\odot}\ yr^{-1}$) serve as ideal laboratories for observations of all types of massive stars, as they are typically located in one compact region on the sky and are convenient for observations in multi-object spectroscopy mode. Different properties of dIrrs in the Local Group provide the opportunity to investigate the population and evolution of massive stars within the context of the different metallicities of their host galaxies (from [Fe/H] = -0.5 dex in the LMC, to [Fe/H]

= -1.85 dex in Sextans A).

There are a couple of photometric surveys which cover dwarf irregular galaxies. Accurate optical photometry survey in *UBVRI* colors for 7 dIrrs with ongoing star formation are presented in Massey et al. (2007d). This survey is based on observations at 4m telescopes at Kitt Peak National Observatory (KPNO) and Cerro Tololo Inter-American Observatory of the galaxies: IC 10, NGC 6822, WLM, Sextans B, Sextans A, Pegasus, and Phoenix. This work formed the basis for optical selection criteria for identifying dusty massive stars in the Local Group (see next Section). However, for our work we mainly used selection criteria based on mid-IR photometry.

We selected evolved massive star candidates from published *Spitzer/IRAC* photometry (Boyer et al. 2009) of 7 nearby irregular dwarf galaxies with relatively high star formation rates, namely: IC 10, IC 1613, Pegasus, Phoenix, Sextans A, Sextans B and WLM. The selection of galaxies was made by taking into account the occurrence of recent star-formation episodes (Mateo 1998). All program galaxies have a few recent star formation populations (Tolstoy 1999; Hodge et al. 1999), apart from the low-mass Phoenix galaxy, which has one central, young (100 Myr) stellar population zone (Martínez-Delgado et al. 1999). Basic information about the program dIrr galaxies such as distances, distance moduli, systemic radial velocities and metallicities are presented in Table 2.1. The distance, distance moduli, systemic radial velocities and metallicities are taken from McConnachie (2012). The second systematic RV value for Phoenix is from Gallart et al. (2001).

2.2 Selection criteria

Identifying RSGs and other dusty massive stars in a photometric survey is a challenging task. The contamination from foreground stars, primarily Milky Way disk dwarfs and halo giants is significant for RSGs. The work of Massey (1998) showed success in distinguishing extragalactic RSGs from foreground contaminants that originally identified a

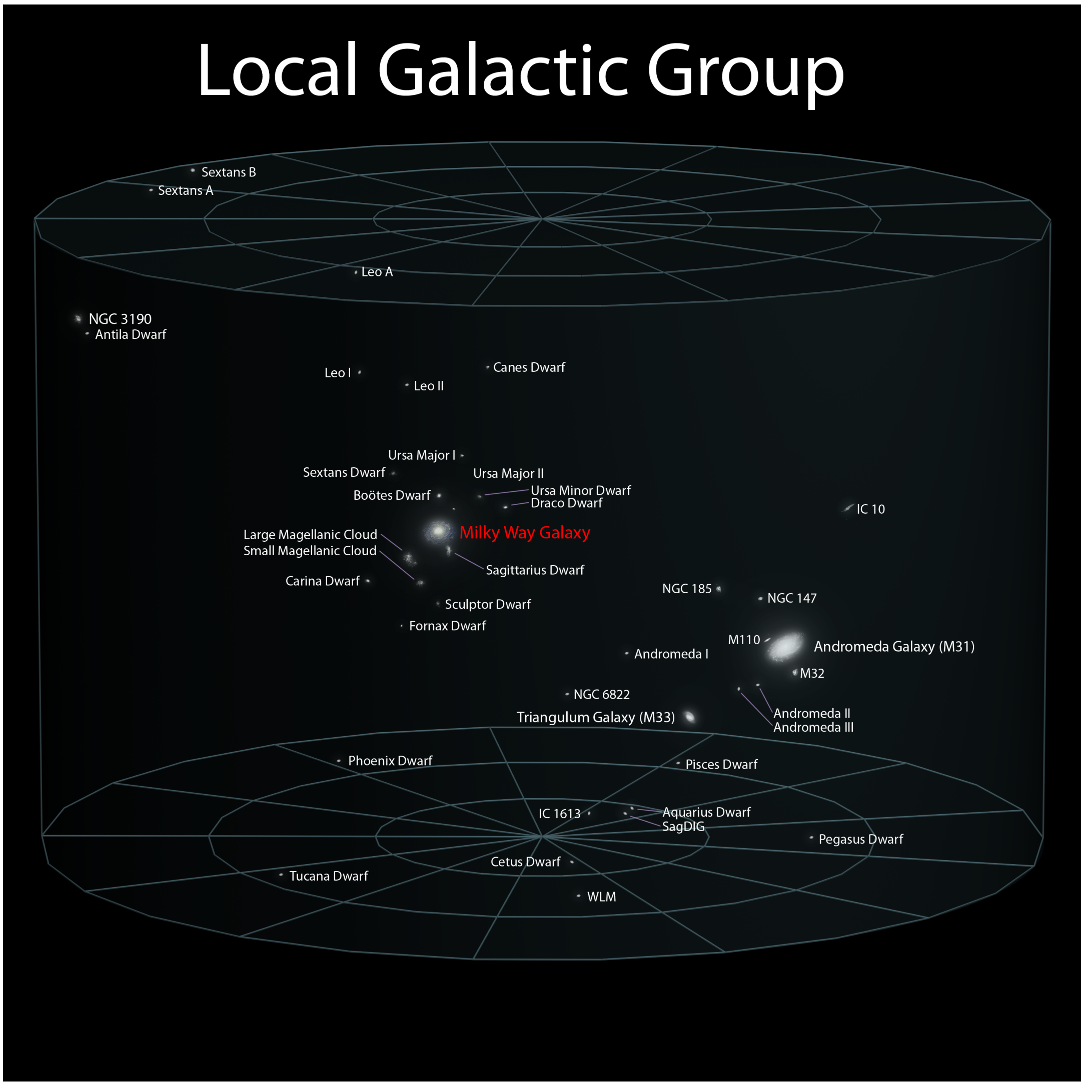

Figure 2.1: Local Group galaxies map. (Image credit: Andrew Z. Colvin.)

Table 2.1: Target galaxy properties.

Name	Distance (kpc)	Distance modulus (mag)	Radial velocity (km s^{-1})	$[Fe/H]$ (dex)
IC 10	794±44	24.27±0.18	−348±1	−1.28
IC 1613	755±42	24.39±0.12	−233±1	−1.60
Pegasus	920±30	24.82±0.07	−183±5	−1.40
Phoenix	415±19	23.09±0.10	−13±9, −52±6	−1.37
Sextans A	1432±53	25.78±0.08	+324±2	−1.85
Sextans B	1426±20	25.60±0.03	+304±1	−1.60
WLM	933±34	24.85±0.08	−130±1	−1.27

sample of RSGs in M31, M33 and NGC 6822 using the two-color method, applying a cutoff line in the $V - R$ versus $B - V$ diagram that separates RSGs (above the line) from foreground dwarf contaminants (below the line) due to surface gravity effects. Figure 2.2 presents the two-color diagram for M31 which illustrates the optical BVR selection criteria. The value of $V - R$ color is sensitive primarily to effective temperature, while $B - V$ is sensitive both to effective temperature and surface gravity. At a given $V - R$, stars with larger $B - V$ values are expected to be supergiants (Massey et al. 2009).

However, as it was mentioned in the first chapter, we initiated the census of RSGs and other dusty massive stars, selecting them using the mid-IR colors, as infrared excess of such dusty objects serves as an advantage to identifying them in mid-IR wavelength region.

The first systematic study of the mid-IR properties of massive stars in any galaxy was carried out by Bonanos et al. (2009, 2010) for the Large and Small Magellanic Clouds (at 0.5 $Z_{\odot}$ and 0.2 $Z_{\odot}$, respectively). The motivation was threefold: (1) to use the infrared excesses of massive stars to probe their winds, circumstellar gas, and dust, (2) investigate the dependence of their properties on metallicity, and (3) to provide a "roadmap"

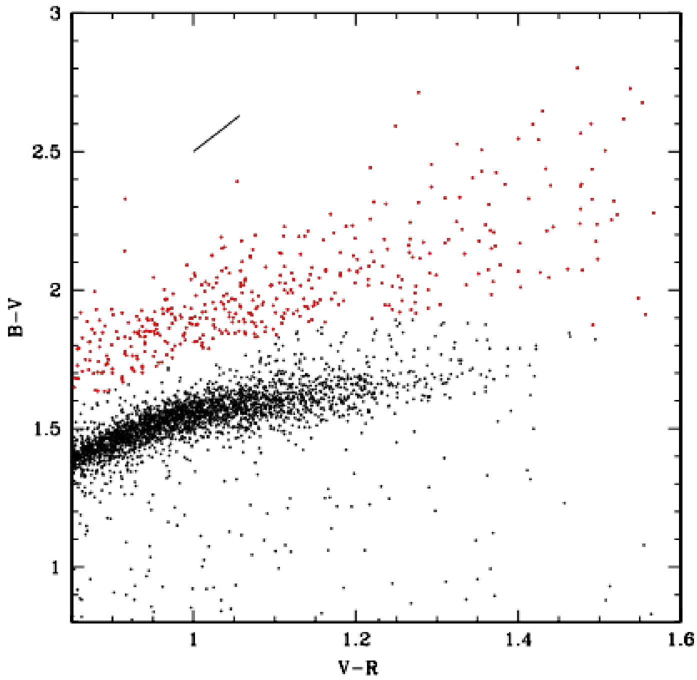

Figure 2.2: Two-color diagram showing the separation of candidate RSGs (red) from foreground stars (black). Stars with lower surface gravities (i.e., RSGs) will have larger $B-V$ values than stars with higher surface gravities (foreground dwarfs) for a given $V-R$. A reddening line corresponding to a "typical" $E(B-V) = 0.13$ for early-type stars in M31 (Massey et al. 2007b) is shown in the upper left (from Massey et al. 2009).

for studies of other, more distant, galaxies. The method involved compiling a catalog of massive stars with known spectral types from the literature (1750 stars in the LMC and 5324 stars in the SMC), and cross-matching them with the SAGE and SAGE-SMC photometric databases, which resulted in a multi-band photometric catalog from 0.3 to 24μm (1286 matches in the LMC and 3654 matches in the SMC). This work increased by an order of magnitude the number of spectroscopically classified, massive stars for which mid-infrared photometry was available, and provided spectral energy distributions for all known types of hot and cool massive stars. The resulting infrared color-magnitude diagrams illustrated that the sgB[e], RSGs, and LBVs are among the brightest infrared point sources in the Clouds, due to their intrinsic brightness, and at longer wavelengths, due to dust. An illustration of this can be found on the mid-IR $[3.6] - [4.5]$ and $[3.6] - J$ CMDs for the LMC, showing the position of different types of spectroscopically confirmed massive stars, which are presented in Figures 2.3 and 2.4. Furthermore, the spectral energy distribution (SED) shapes of sgB[e] were found very similar, in contrast to the variety of SED shapes observed among the LBVs, which are likely related to the time since the last outburst event and the amount of dust formed. Armed with these studies we can select the candidate RSG, LBVs and sgB[e] stars in a sample of nearby galaxies, which we will confirm with follow-up optical and near-infrared photometry and spectroscopy. These should yield additional RSGs, LBVs and sgB[e] stars, or other classes of dusty massive stars.

Our selection was based on mid-infrared colors and the exact criteria depend on the types of massive stars targeted.

In this work, our primary aim is to identify RSGs, therefore we selected sources that satisfied the following criteria:

i) $M[3.6] < -9$ mag

ii) $J - [3.6] > 1$ and $[3.6] - [4.5] < 0$ (based on Bonanos et al. 2009, 2010)

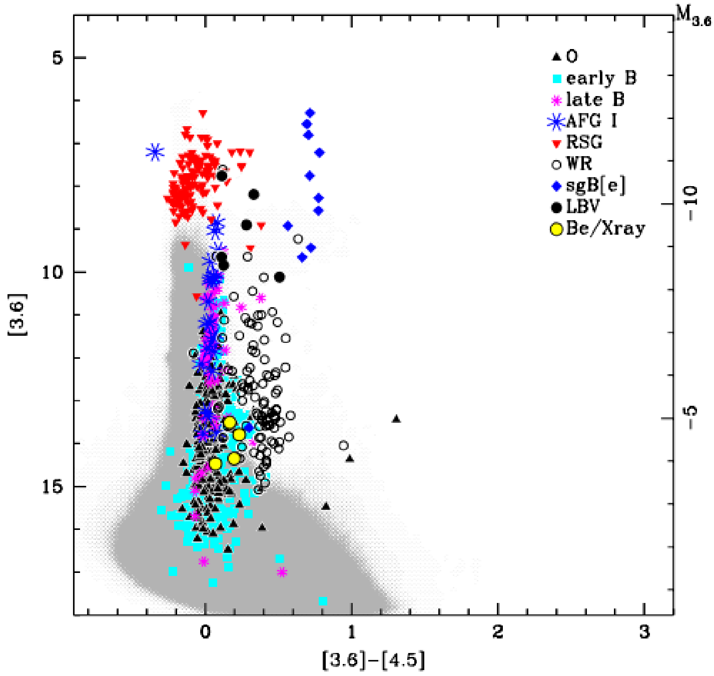

Figure 2.3: [3.6] vs. [3.6] − [4.5] CMD for massive stars in LMC (from Bonanos et al. 2009). Different symbols denote different spectral types. The sgB[e], RSG, and LBVs are among the most luminous stars at 3.6μm.

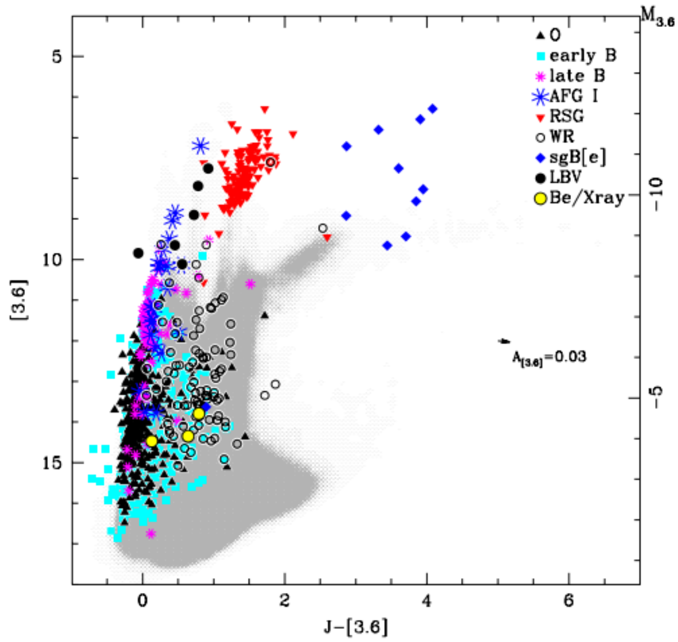

Figure 2.4: Same as Figure 2.3, but for the [3.6] − *J* vs. [3.6] CMD (from Bonanos et al. 2009).

iii) $J - H > 0.65$ and $H - K < 0.6$ (based on Rayner et al. 2009).

We also selected other luminous sources such as candidate LBVs and sgB[e] as stars with $[3.6] - [4.5] > 0.15$ mag (Bonanos et al. 2009, 2010). Moreover, in order to find prominent candidates for LBVs it is necessary to search for $H\alpha$-emitting sources. In case of investigations of LBVs population in dIrr galaxies the ideal survey of $H\alpha$ emission objects could be found in Massey et al. (2007b).

All of our candidates were also searched in VizieR using a 2″ radius, for matches in other optical and near-IR photometric catalogs to eliminate known foreground stars, H II regions, galaxies, and radio sources. We also checked the proper motions of sources in VizieR to decrease the probability of selecting foreground objects.

Additional bright IR sources at smaller $[3.6] - [4.5]$ color were observed when it was possible to add slits on the FORS2 spectroscopic masks (multi-object MXU mode) without compromising the main targets. Following Bonanos et al. (2009, 2010), the selection criteria presented above include LBVs, sgB[e]s, WR stars, and RSGs, but exclude normal OB stars. In the case of the Phoenix galaxy, since all targets were relatively faint, we selected candidates with absolute magnitude $M_{3.6\mu m} < -6$ mag, in order to fill the rest of the free space on the multi-object mask (MXU). During the three years of the project, in total 135 stars were selected and observed in 7 dIrr galaxies under the different observational sets. Among observed targets there are 124 unique: 12 in IC 10, 6 in IC 1613, 19 in Pegasus, 14 in Phoenix, 18 in Sextans A, 5 in Sextans B, 50 in WLM.

It should be noted that after the observations were carried out, new mid-IR photometry became available from the DUSTiNGS survey (DUST in Nearby Galaxies with *Spitzer*, Boyer et al. 2015b). This survey includes 3.6 and 4.5-μm imaging of 50 nearby dwarf galaxies within 1.5 Mpc, aiming to identify dust-producing asymptotic giant branch (AGB) stars. Deep images were obtained with the IRAC camera onboard *Spitzer* telescope during the post-cryogen phase on 2 epochs, with an average difference of 180 days. Since the new photometry from DUSTiNGS has better accuracy, we used the new [3.6] and

[4.5] values (Epoch 1) for our analysis, which vary from the old ones by 0.05 - 0.2 mag in both [3.6] and [4.5] bands, even though the selection process was based on the published photometry from Boyer et al. (2009). Given that the spatial resolution of *Spitzer*/*IRAC* photometry at [3.6] and [4.5] bands is 2", which corresponds to $\approx$ 10 pc at a distance 1 Mpc, it is unlikely to have 2 bright mid-IR sources in this area.

Chapter 3

Observations and data reduction

3.1 Observations with the GTC and du Pont telescopes

3.1.1 Longslit mode

The first set of observations of selected targets were performed in longslit mode for 6 RSG candidates in Sextans A and 2 candidates in IC 1613. These observations serve as a basis for our first paper of this PhD Thesis (Britavskiy et al. 2014). Our targets in Sextans A were observed with the 10.4 m Gran Telescopio Canarias (GTC) using the OSIRIS spectrograph in longslit mode during several nights in January 2013. For our observations we used the R1000R grism with the 1.2″ slit. The resolving power provided by this combination was R ≈ 1100 with an average signal-to-noise ratio (S/N) ≈ 100 and the spectral range extended from 5100 Å to 10000 Å.

Targets from the dwarf galaxy IC 1613 were observed with the 2.5 m du Pont telescope at Las Campanas Observatory, Chile. The WFCCD with the 400 lines/mm grism and 1.6″ slit, gave a resolution of FWHM ≈ 8 Å at 6000 Å (R ≈ 800). The names, optical, near-IR, and mid-IR magnitudes and colors of the six selected stars in Sextans A and 2 in IC 1613, for which longslit spectroscopy were carried out, are given in Table 3.1.

Characteristics of observations of targets in Sextans A and IC 1613 in longslit mode, such as the coordinates, UT date, exposure time, and S/N for each object are presented in Table 3.2. The reduction and extraction of the spectra were performed by standard IRAF[1] procedures, i.e. dark subtraction, division by the flat fields, wavelength calibration, spectra extraction, continuum placement, and normalization.

The schematic algorithm of how data reduction and data extraction process were performed for the spectral data obtained with the GTC and du Pont telescopes is presented in Figure 3.1 (it should be noted, this algorithm was not used for spectral data obtained with the VLT telescope, as an automatic data reduction pipeline for each instrument is available). In this block diagram the IRAF's routines that have been used for different purposes are emphasized by italic font. In brief, the RAW images obtained from the telescopes, consist of 4 different observational blocks. Three of them are calibration images: ThAr calibration lamps, bias images and flat field images. The last block of observations is the science images of observed targets, namely, pre images, slit images, and the images of target spectra. For each type of observational block we applied different functions to produce the final combined image, which we used for spectra extraction. For example, the function *imcombine* was used adding the RAW science images and ThAr lamps images, *darkcombine* were use for the constructing "master bias" image as a average of bias images. The *flatcombine* and *response* functions were used to make the average, and the normalisation of flat field images respectively. Then, we used function the *ccdproc* for final reduction of the spectra images, and the function *apall* for the extraction of the spectra from the CCD images. More details are presented in Figure 3.1.

[1] IRAF is distributed by the National Optical Astronomy Observatory, which is operated by the Association of Universities for Research in Astronomy (AURA) under cooperative agreement with the National Science Foundation.

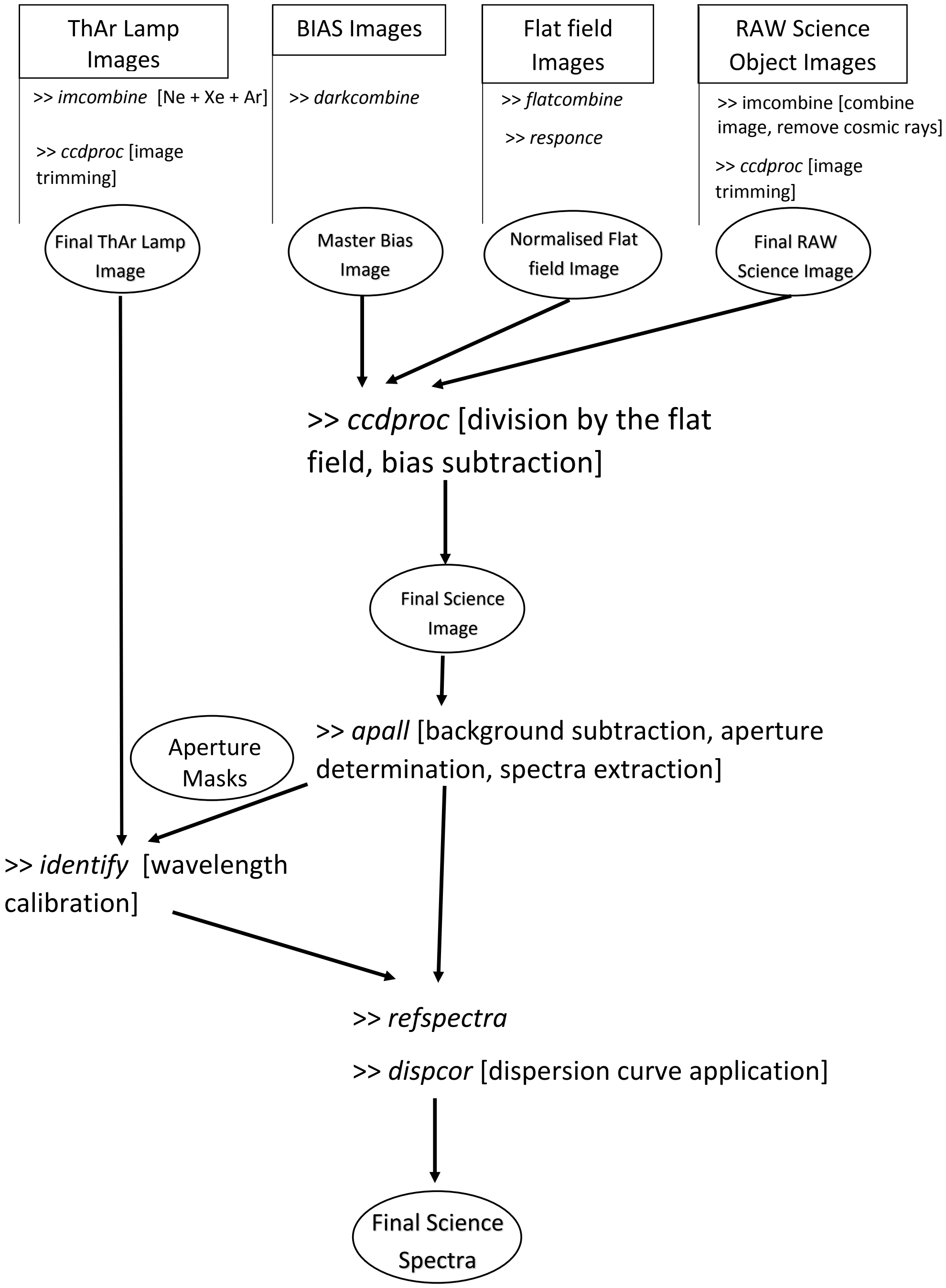

Figure 3.1: The schematic block diagram describing the data reduction process of spectral data, which have been observed in longslit mode with the GTC and du Pont telescopes.

Table 3.1: Photometry and color indices of the program stars which were observed in longslit mode (see Britavskiy et al. 2014).

Star Name	V (mag)	$B-V$ (mag)	$V-R$ (mag)	M[3.6]* (mag)	[3.6] − [4.5] (mag)	$J-[3.6]$ (mag)	$J-H$ (mag)	$H-K$ (mag)	Q1	Q2
Sex A 1	18.547	1.493 ± 0.008	1.017 ± 0.005	−11.31	0.052	1.05 ± 0.05	0.932 ± 0.069	0.175 ± 0.116	0.30	0.53
Sex A 2	19.097	1.484 ± 0.011	0.986 ± 0.006	−10.71	0.121	1.20 ± 0.08	0.900 ± 0.108	−0.034 ± 0.181	0.25	−0.28
Sex A 3	18.650	0.835 ± 0.006	0.485 ± 0.005	−9.40	0.049	0.53 ± 0.16	0.451 ± 0.281	1.632 ± 0.227	0.61	–
Sex A 4	18.295	1.860 ± 0.008	0.935 ± 0.005	−11.11	−0.064	1.08 ± 0.05	0.902 ± 0.084	0.058 ± 0.135	0.30	0.40
Sex A 5	18.322	1.802 ± 0.008	0.918 ± 0.005	−11.11	−0.027	1.16 ± 0.06	0.763 ± 0.075	0.176 ± 0.114	0.32	0.61
Sex A 6	18.596	1.899 ± 0.009	0.992 ± 0.005	−11.11	−0.004	1.26 ± 0.06	0.883 ± 0.090	0.001 ± 0.155	0.26	−0.18
IC 1613 1	18.98†	–	–	−9.25	−0.05	3.26 ± 0.05	0.337 ± 0.087	0.973 ± 0.091	−0.53	−10.38
IC 1613 2	17.258	1.513 ± 0.006	0.778 ± 0.011	−11.02	−0.009	0.90 ± 0.03	0.692 ± 0.037	0.212 ± 0.044	0.32	0.65

∗ The distance modulus that we used is 25.61 ± 0.07 mag for Sextans A (Dolphin et al. 2003), and 24.32 ± 0.06 mag for IC 1613 (Dolphin et al. 2001). † Several independent estimates of magnitude and colors are available for this star (e.g. $V = 17.97$; 19.33). Details in Section 4.2.

Table 3.2: Log of observations (coordinates, UT date, exposure time, signal-to-noise ratio), derived radial velocities, CaT* indices, and spectral types. $\mathrm{RV}_{Sex\ A} = 323$ km s^{-1} and $\mathrm{RV}_{IC\ 1613} = -238$ km s^{-1}.

Star Name	DUSTiNGS ID	R.A. (J2000)	Dec (J2000)	UT Date (HJD-2450000)	Exp. time (sec)	S/N	RV ± σ_{RV} (km s^{-1})	CaT* ± σ_{CaT*}	Spectral classification	Luminosity classification
Sex A 1	94113	152.742211	−4.702496	6326.73523	600	100	−10 ± 18	4.2 ± 1.2	Late M	III-V
Sex A 2	88542	152.749997	−4.651711	6320.57939	500	120	3 ± 22	4.2 ± 1.1	Late M	III-V
Sex A 3	59443	152.792892	−4.701834	6330.52805	600	50	273 ± 18	4.3 ± 1.4	F	III-V
Sex A 4	106505	152.72426	−4.68539	6298.62638	500	150	368 ± 15	10.7 ± 2.2	Early K	I
Sex A 5	72683	152.77316	−4.69916	6300.71179	500	80	352 ± 21	10.2 ± 2.3	Early K	I
Sex A 6	98112	152.73636	−4.67753	6320.54736	500	120	305 ± 27	9.5 ± 2.2	Late K	I
IC 1613 1	161666	16.158911	2.112404	6299.54371	1200	14	−184 ± 25	10.9 ± 2.9	M0 – 2	I
IC 1613 2	119457	16.210361	2.106991	6301.57033	1800	24	−186 ± 7	15.9 ± 2.5	M2 – 4	I

Table 3.3: Journal of observations at GTC-OSIRIS spectrograph in MOS mode.

ID	MJD (JD – 2400000.5)	Exp. (s)	Observed targets
IC 10	56928.88963	2000	12
Sextans B	57014.17851	2000	5
IC 1613	57007.91051	1300	6

3.1.2 Multi-object mode

The second set of observations with the GTC telescope were carried out in multi-object spectroscopy mode (MOS) in September and December 2014. For these observations we used the OSIRIS spectrograph with the same set up parameters as in longslit mode observations, i.e. R1000R grism with the 1.2″ slit. The resolving power was R ≈ 1100 with the wavelength range from 5100 Å to 10000 Å. The field of view of the available MOS OSIRIS masks (7.5'x6') was suitable to cover each dIrr galaxy with 1 field. The journal of observations, i.e. the time of observation (MJD), exposure time, number of observed targets are given in Table 3.3.

3.2 Observations with the ESO-VLT

The most numerous sample of selected targets was observed with the FORS2 spectrograph at ESO's Very Large Telescope (VLT) during 3 observing runs (program IDs 090.D-0009, 091.D-0010, and 095.D-0313). In the Appendix all information about allocated telescope times which we used in this PhD Thesis are presented. The observations were carried out in multi-object spectroscopy mode, which maximizes the number of selected targets in one observational set. For each galaxy the observations were performed in one MXU field, apart from observations of Sextans A and WLM, where observations were performed in two MXU fields. In Sextans A, one MXU field was observed twice, while for WLM the observations were performed in two different observational fields. The journal of observations, i.e. the time of observation (MJD), exposure time, number of observed targets are given in Table 3.4.

For the proposals 090.D-0009 and 091.D-0010, 43 high priority targets were selected, however, to fill the free space on the MXU masks we added 36 more targets. These additional targets were selected among the brightest sources in the [3.6] band, however, quite often they were fainter than the magnitude cut-off criteria ($M_{3.6\mu m} \leq -9$ mag), and they did not always satisfy our selection criteria in terms of the [3.6] − [4.5] color. Also, 10 of these additional targets have been reported as candidate carbon stars based on their photometry (Battinelli & Demers 2000, 2004; Menzies et al. 2008).

The proposal 095.D-0313 concentrated only on the WLM galaxy in order to complete the census of luminous IR stars in this galaxy. To avoid the slit overlaps in the compact WLM field we proposed to create 3 masks for the same one field (6.8’x6.8’) with different targets in each of them, however only one mask was observed. We selected 55 targets, however, only 23 were observed because this observational set was not completed during the service mode observations.

The data reduction of the observed targets was performed with the FORS pipeline recipes version 4.9.23 under ESO *Reflex* workflows version 2.6 (Freudling et al. 2013). With the help of this pipeline 1D spectra were automatically extracted from the raw image. The reduction process included standard procedures such as bias subtraction, flat field division, background subtraction and wavelength calibration. For each field, spectra were obtained four times and combined using the IRAF[2] *scombine* routine. The final average extracted 1D science spectra were normalized using the *continuum* procedure. All spectra were flux calibrated using MOS (moveable slit) mode observations of the flux standard

[2]IRAF is distributed by the National Optical Astronomy Observatory, which is operated by the Association of Universities for Research in Astronomy (AURA) under cooperative agreement with the National Science Foundation.

Table 3.4: Journal of observations at VLT-FORS2 spectrograph in MOS mode.

ID	MJD (JD − 2400000.5)	Exp. (s)	Observed targets
Pegasus	56487.34940	4x660	19
Phoenix	56279.13559	4x660	14
Sextans A (Set 1)	56360.08635	4x660	15
Sextans A (Set 2)	56423.08622	4x660	15
WLM (Objects 1-18)	56279.08819	4x660	18
WLM (Objects 19-31)	56280.10188	4x660	13
WLM P95	57260.15575	4x1200	23

stars. The spectra have an average signal-to-noise ratio (S/N) ≈ 20 and a spectral range from 4300 Å to 9000 Å. It should be noted that we did not achieve this wavelength range for all spectra due-to limited space for slits on the CCD in MOS mode; some of them have a shorter range, which made spectroscopic analysis difficult. The resolving power varies from R ≈ 400 at 5000 Å to R ≈ 680 at 8600 Å. The information about all telescope proposals that were included in this PhD Thesis are listed in the Appendix.

The list, spectral analysis, and classifications of all selected and successfully observed targets are presented in the next Chapter.

Chapter 4

Spectral classification and analysis

The analysis of the spectra of our targets was based on the determination of the following three characteristics:

i) the radial velocity - we measured the radial velocities (RVs) from the calcium II triplet lines ($\lambda\lambda$ 8498, 8542, 8662 Å), which provide an important way to distinguish extragalactic objects from foreground ones.

ii) the spectral type - we expect the RSG candidates to have a K or M spectral type, which are simple to distinguish by the strength of their optical TiO bands.

iii) the luminosity class - we used the strength of the Ca II triplet, which is a good luminosity indicator for late-type stars, because it is sensitive to log g, but weakly dependent on metallicity (Massey 1998).

To measure RVs, we cross-correlated spectral templates from the NASA Infrared Telescope Facility spectral library for cool stars (Rayner et al. 2009) against our spectra using the IRAF task *fxcor*. Before applying this method we first normalized the whole spectra using a fifth-order cubic spline, then we cut the Ca II region ($\lambda\lambda$ 8380 – 8800 Å) and normalized it again to a relative flux near 1. The template spectral resolution was decreased to the value of the resolution of our spectra by convolving with a Gaussian function.

We determined the spectral type with the help of the ESO UVES Paranal Observatory Project (POP) library of high-resolution spectra across the H-R diagram (Bagnulo et al. 2003). This high-resolution library contains a broad range of spectral types from F2 to M6 and luminosity classes ranging from dwarfs (V) to supergiants (I). We decreased the resolution of the templates from R $\approx$ 70000 to R = 1000, in case of GTC and du Pont spectroscopic data, and to R = 500 in case of VLT observations, to match our observed spectra. At these resolutions it is quite difficult to distinguish the lines that are indicators of the spectral type - instead of lines, we only have blends. Nevertheless, the comparison with templates provides us with the opportunity to investigate the behavior of the TiO bands, which are very strong for K and M spectral types. The accuracy of our spectral type classification is at the level of distinguishing late/early spectral subtypes. Our spectra are also of sufficient quality for further luminosity classification, namely for separating the supergiants from giants.

The classification of red supergiants in the optical/near-IR region has been explored by several authors. Different criteria have been proposed depending on the available resolution. The spectral classification of low-resolution spectra is described in Ginestet et al. (1994), Negueruela et al. (2011, 2012a), and Massey (1998), who presented a classification of RSGs in M31 and M33. However, the resolution of our spectra is not high enough to identify luminosity-sensitive features (Fe, Ti) apart from the Ca II triplet, which we used for identifying RSGs in our sample.

We applied two methods, which are based on the Ca II triplet, to confirm our classification: (i) the investigation of the continuum level around the Ca II region and (ii) a quantitative profile analysis of the Ca II triplet. The first method uses templates of cool stars (Rayner et al. 2009) to compare of the Ca II region continuum shape. By shape we mean the average continuum, which consists of blends where we cannot separate the individual lines of the elements. In this step we confirm our spectral type classification because the level of the continuum around the calcium triplet region is quite sensitive to temperature, mainly because of the TiO bands, as mentioned above. The second method of our analysis was to quantitatively analyze of the Ca II triplet profiles to confirm the luminosity classification. We used the empirical calibration of the near-IR index CaT* (defined by Cenarro et al. 2001), which measures the Ca II triplet strength, corrected for the contamination from Paschen lines. This index is quite universal with small limitations on the properties of the input spectra and applies to a wide range of metallicities.

As an example in Figure 4.1 we present the Ca II triplet region for all our targets that have been observed with GTC/OSIRIS and du Pont/WFCCD spectrographs in longslit mode (Britavskiy et al. 2014). The first two spectra (from top to bottom) are taken from the IRTF atlas (Rayner et al. 2009), demonstrating the difference between the strength of the Ca II features for a K supergiant and a bright giant. The next two spectra have an RV near zero therefore these objects are foreground M dwarfs or giants. The other spectra indicate extragalactic objects, as deduced from their radial velocities and depths of Ca II triplet lines.

For spectra which have a high enough quality to resolve the Fe I, Ti I, and the TiO bands we accomplished accurate classification using the criteria described in Negueruela et al. (2012b). The relations between the strengths of the Ti I and Fe I in the Ca II triplet region enable the determination of the spectral type. For example, we explain the detailed spectroscopic analysis for the two RSG spectra in IC 1613, which were observed with the du Pont telescope. We found several criteria for the classification of these two stars (see Fig. 4.2): the strength of the 8514 Å feature compared with Ti I 8518 Å is an indicator of high luminosity, while the TiO bandhead features at 8442 Å and 8452 Å visible in IC 1613 2 are a sign of M4 type. The fact that the line Fe I 8611 Å is stronger than Fe I 8621 Å, which is usually contaminated by the 8620 Å diffuse interstellar band, indicates the extragalactic nature of these stars. In M-type spectra the relative strength of the various Ti lines indicates how late the spectral type is. In particular, the strength of Ti I 8426 Å and of the TiO features at 8432 Å blended with the Ti I 8435 Å line becomes similar to the

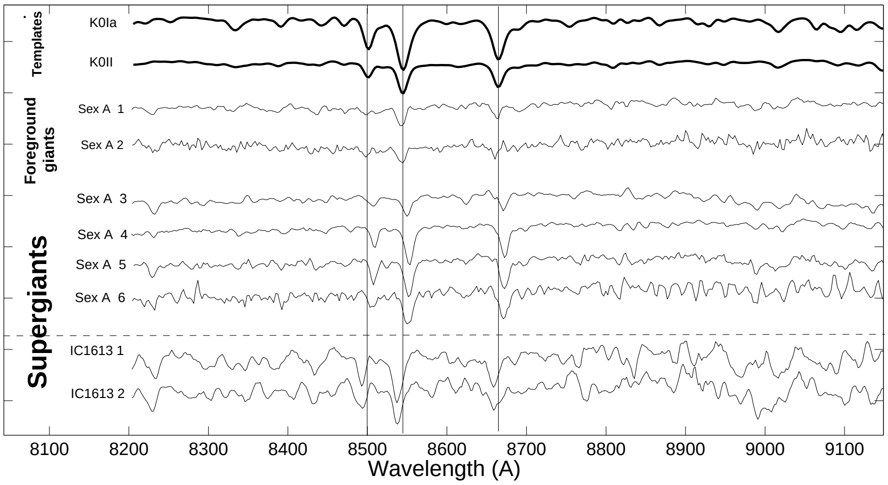

Figure 4.1: Ca II triplet region for all the targets which have been observed with the du Pont and GTC telescope in longslit mode. The upper two objects are templates from Rayner et al. (2009). Vertical lines show the rest wavelength position of the calcium triplet ($\lambda\lambda$ 8498, 8542, 8662 Å), relative to which the Doppler shifts of spectra are measured. We conclude that Sex A (3,4,5,6) and IC 1613 (1,2) are extragalactic objects (Britavskiy et al. 2014).

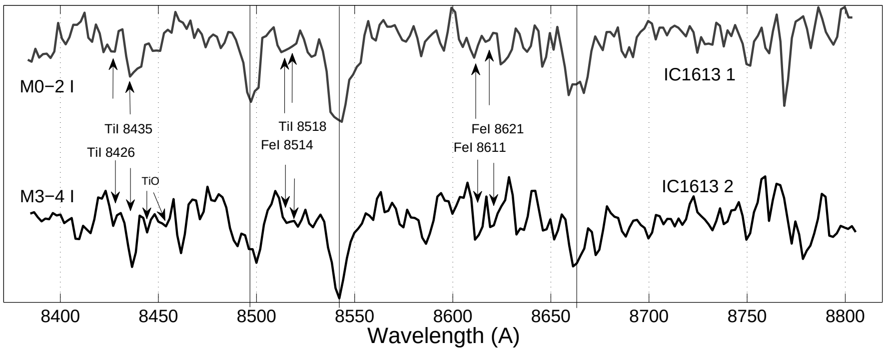

Figure 4.2: Ca II triplet spectral region of the IC 1613 targets. Using the criteria described by Negueruela et al. (2012b), we find a spectral type M0-2 I for IC 1613 1 and M2-4 I for IC 1613 2 (Britavskiy et al. 2014).

TiO 8660 Å / Ca II 8662 Å features and can be used as an indicator of spectral type. We therefore find a M0–2 I classification for IC 1613 1 and M2–4 I for IC 1613 2.

The next paragraph is devoted to the analysis of spectra that were obtained from the du Pont and GTC telescopes in longslit mode (from Britavskiy et al. 2014). The resulting radial velocities are presented in Table 3.2. The stars Sex A (3, 4, 5, 6) and IC 1613 (1, 2) have radial velocities that confirm their extragalactic nature. Sex A (1, 2) have radial velocities near 0 and a weak Ca II triplet, thus we conclude that they are foreground giants. The resulting spectral type classification is shown in Fig. 4.12. The targets observed on the du Pont telescope (the targets from IC 1613) have a resolution $FWHM = 8$ Å, while the spectral resolution of the Cenaro spectra library, from which these indices have been determined, is $FWHM = 1.5$ Å. We do not pretend to have computed the real CaT* indices, we have measured only a quantitative characteristic value of the depth of the Ca II triplet of our sample. We calculated indices and errors by using the indexf (Cardiel 2010) program package. Results are shown in Table 3.2. For foreground giants this index is half that of supergiants and agrees with the empirical fitting-function library (Cenarro et al. 2002) for stars that have the same spectral type and metallicity. The CaT* index measurements therefore confirm the supergiant nature of 5 stars.

The resulting spectral type classification of targets which were observed on VLT/-FORS2 spectrograph, their CaT index, when available, are shown in Tables 4.1, 4.2, 4.3, 4.4, 4.5 and 4.6. The list of targets that were observed with the GTC/OSIRIS spectrograph in multi-object spectroscopy mode are presented in Tables 4.7, 4.8, and 4.9. These tables list a running ID number and ID from the DUSTiNGS of all observed targets, their coordinates, radial velocities (RV), optical magnitude and colors (from Massey et al. 2007c), absolute [3.6] magnitude ($M_{[3.6]}$, computed using the distance in Table 2.1), [3.6] − [4.5] colors, the final spectral classification and notes. In cases where it was not possible to determine the luminosity class, e.g. the spectrum did not include the Ca II triplet region, we provide only the spectral type. In the column "Notes" other spectroscopic information from the literature is listed. The label "Unclassified" was used for the targets with low quality spectra or spectra with high noise that did not allow a spectral type determination.

Figures 4.3 – 4.9 present the color-magnitude diagrams (CMD) and spatial distribution of our targets in the seven program galaxies. In the $M_{[3.6]}$ vs. [3.6] – [4.5] CMDs we keep the same formalism of object classification (labels) as we used in Tables 4.1 – 4.9. On each CMD we marked the regions that satisfy our photometric selection criteria in light grey. The region on the left part corresponds to the area where RSGs are expected ($[3.6]-[4.5] < 0$), the region on the right corresponds to the LBV and sgB[e] stars ($[3.6] - [4.5] > 0.15$). The value of the absolute magnitude cut-off varies from galaxy to galaxy. For example, the cut-off was decreased to $M_{3.6} < -6$ mag in Phoenix, since all targets in this galaxy are relatively faint in comparison with the other galaxies. In WLM, the cut-off was changed to $M_{3.6} < -8$ mag to select more targets in the LBV region, since 2 MXU masks were available per field. All unclassified objects are faint and have large error bars in the [3.6] – [4.5] color, in comparison with the objects for which spectral classification was performed successfully. In some cases the absolute magnitude of the targets is below the magnitude selection criteria cut-off $M_{3.6} < -9$ mag. This discrepancy is due to the fact that the selection was based on older photometry, while the CMDs plot the more accurate DUSTiNGS photometry.

The analysis of the spatial distribution of observed targets shows us that the majority of foreground and background objects are located outside the main body of dIrrs. Thus, we can conclude that an additional check of the position of candidates with respect to the host galaxy body will help avoid contamination of foreground or background objects.

Table 4.1: Characteristics and classification of observed targets in Phoenix.

Name	DUSTiNGS ID	R.A.(J2000) (deg)	Decl.(J2000) (deg)	RV (km s^{-1})	V (mag)	$B-V$ (mag)	$V-R$ (mag)	$M_{[3.6]}$ (mag)	[3.6] − [4.5] (mag)	Spectral class	Notes
1†	163185	27.72029	−44.44337	–	22.27±0.04	1.04±0.17	0.89±0.05	−7.16±0.03	−0.18±0.09	–	Unclassified
2†	132464	27.77338	−44.43438	–	–	–	–	−7.04±0.03	−0.43±0.11	–	Unclassified
3†	124582	27.78666	−44.42456	–	–	–	–	−8.54±0.03	−0.20±0.05	Carbon star	MFW2008
4†	119803	27.79501	−44.41927	−122±11	19.50±0.01	1.17±0.01	0.64±0.01	−6.51±0.07	−0.08±0.20	K1-2 I	CaT=7.8±0.1
5†	155842	27.73286	−44.41641	–	18.04±0.01	1.12±0.01	0.73±0.01	−8.08±0.04	−0.03±0.05	K3-4	–
6†	126900	27.78269	−44.41072	−66±14	16.44±0.01	0.68±0.01	0.41±0.01	−8.55±0.04	−0.03±0.06	G II, For.	CaT=3.8±0.2
7†	115117	27.80300	−44.40274	−30±9	18.74±0.01	1.06±0.01	0.69±0.01	−7.25±0.04	−0.00±0.08	K II, For.	CaT=3.6±0.1
8†	164291	27.71847	−44.39964	–	19.31±0.01	1.63±0.02	0.57±0.01	−8.62±0.03	0.27±0.04	–	Defect spectrum
9†	151578	27.74011	−44.39561	–	–	–	–	−6.40±0.20	0.37±0.31	–	Unclassified
10†	123859	27.78807	−44.48292	–	–	–	–	−7.13±0.04	−0.10±0.10	–	Unclassified
11†	153862	27.73609	−44.47420	–	20.39±0.01	1.41±0.02	1.14±0.01	−7.76±0.03	0.04±0.05	M2-4	–
12	143442	27.75407	−44.47075	–	–	–	–	−8.45±0.03	0.38±0.05	Carbon star	MFW2008, VAR
13	138078	27.76355	−44.46954	–	19.47±0.01	1.49±0.01	0.57±0.01	−7.99±0.04	0.24±0.04	K2-3	–
14	134407	27.76993	−44.45805	–	18.41±0.01	1.54±0.01	1.05±0.01	−9.18±0.04	0.04±0.05	M4-6	–

† – targets added to fill the free space on the MXU mask. "MFW2008" refers to photometric candidates for AGB stars, according to Menzies et al. (2008). Targets with the comment "VAR" refer to newly identified dusty variable AGB stars from Boyer et al. (2015a). For. – Foreground giants.

Table 4.2: Characteristics and classification of observed targets in Pegasus.

Name	DUSTiNGS ID	R.A.(J2000) (deg)	Decl.(J2000) (deg)	RV (km s^{-1})	V (mag)	$B-V$ (mag)	$V-R$ (mag)	$M_{[3.6]}$ (mag)	[3.6] − [4.5] (mag)	Spectral class	Notes
1	116706	352.14938	14.73709	−257±18	20.72±0.02	2.22±0.08	1.11±0.02	−9.15±0.03	−0.11±0.07	M0-2 I	CaT=13.4±0.1
2 †	113755	352.15274	14.74885	–	–	–	–	−9.01±0.04	0.19±0.05	Carbon star	BD2000
3	111150	352.15588	14.72926	–	–	–	–	−9.08±0.03	−0.12±0.08	–	Unclassified
4	105161	352.16320	14.73414	−121±18	19.55±0.01	1.22±0.01	0.75±0.01	−9.59±0.05	0.43±0.05	K3-4 II, For.	CaT=7.3±0.2
5 †	101247	352.16760	14.74385	–	–	–	–	−9.21±0.04	0.55±0.05	–	Unclassified, VAR
6 †	96974	352.17285	14.74603	–	–	–	–	−9.10±0.03	0.35±0.05	–	Unclassified
7 †	92668	352.17810	14.73468	–	–	–	–	−9.24±0.04	0.69±0.05	–	Unclassified
8	84798	352.18787	14.72049	−143±18	18.71±0.01	1.59±0.01	1.02±0.01	−10.36±0.05	−0.02±0.06	M0-2 II, For.	CaT=5.4±0.1
9	79037	352.19500	14.75781	−129±20	–	–	–	−8.60±0.03	0.53±0.05	–	Unclassified, CaT=4.9±0.1
10†	76368	352.19830	14.75453	–	22.51±0.14	−0.01±0.19	0.30±0.21	−7.99±0.07	0.64±0.15	–	Unclassified
11†	72499	352.20322	14.73991	–	–	–	–	−8.56±0.04	−0.30±0.26	–	Unclassified
12	158441	352.09976	14.75298	–	20.23±0.01	1.71±0.03	1.08±0.01	−9.24±0.05	0.05±0.06	M0-2	–
13	152193	352.10730	14.74175	–	20.29±0.01	1.75±0.03	1.31±0.01	−9.93±0.04	0.09±0.06	M4-6 II, For.	CaT=3.7±0.1
14	138824	352.12320	14.74264	–	20.12±0.02	1.79±0.04	0.83±0.02	−9.90±0.03	0.19±0.04	Late G	–
15	136294	352.12616	14.74971	−248±25	20.68±0.01	2.07±0.07	1.05±0.01	−9.25±0.04	−0.12±0.06	K4-5 I	CaT=12.1±0.1
16	133060	352.12994	14.71921	–	20.16±0.02	1.49±0.04	0.66±0.02	−9.15±0.02	0.19±0.03	K2-3	–
17†	131093	352.13229	14.74073	–	20.55±0.01	1.76±0.05	0.72±0.02	−8.47±0.13	-0.55±0.25	–	Unclassified
18	127165	352.13702	14.70060	−131±20	18.41±0.01	1.43±0.01	0.87±0.01	−9.99±0.04	−0.03±0.06	K2-4 III, **For.**	CaT=6.8±0.1
19†	124505	352.14023	14.73872	–	–	–	–	−9.59±0.03	0.14±0.04	–	Unclassified

† – targets added to fill the free space on the MXU mask. "BD2000" refers to photometric candidates for AGB stars, according to Battinelli & Demers (2000). Targets with the comment "VAR" refer to newly identified dusty variable AGB stars from Boyer et al. (2015a). For. – Foreground giants.

Table 4.3: Characteristics and classification of observed targets in Sextans A.

Name	DUSTiNGS ID	R.A.(J2000) (deg)	Decl.(J2000) (deg)	RV (km s^{-1})	V (mag)	$B-V$ (mag)	$V-R$ (mag)	$M_{[3.6]}$ (mag)	[3.6] − [4.5] (mag)	Spectral class	Notes
1	77330	152.76654	−4.70795	258±19	20.03±0.01	1.76±0.02	0.85±0.01	−9.59±0.04	−0.31±0.16	K1-3 I	CaT=12.7±0.2
2	74652	152.77032	−4.71814	–	20.70±0.01	1.62±0.06	0.85±0.02	−9.96±0.02	0.27±0.03	Late G−K	–
3	72683	152.77316	−4.69916	291±19	18.32±0.01	1.80±0.01	0.91±0.01	−11.37±0.03	−0.08±0.05	K1-3 I	Early K RSG, BBM2014, CaT=11.5±0.1
4	70373	152.77670	−4.70510	258±21	19.58±0.01	1.44±0.02	0.77±0.01	−9.59±0.04	−0.25±0.19	G-F?	YSG candidate, CaT=11.4±0.1
5	67272	152.78140	−4.70179	–	20.90±0.01	1.09±0.06	0.69±0.02	−9.55±0.03	0.14±0.07	–	Unclassified
6	62499	152.78842	−4.71166	–	–	–	–	−8.86±0.06	0.34±0.10	Late G-K	–
7	115101	152.71196	−4.68491	–	–	–	–	−9.37±0.04	−0.05±0.11	–	Unclassified
8	106505	152.72426	−4.68539	217±14	18.29±0.01	1.86±0.01	0.93±0.01	−11.29±0.03	−0.09±0.05	K1-3 I	Early K RSG, BBM2014, CaT=12.4±0.1
9	102187	152.73050	−4.71217	200±22	19.93±0.01	1.58±0.02	0.81±0.01	−9.34±0.05	−0.02±0.09	K1-3 I	CaT=11.8±0.1
10	98470	152.73587	−4.70284	214±27	19.85±0.01	1.45±0.01	0.75±0.01	−9.32±0.04	−0.08±0.08	K1-3 I	CaT=11.0±0.3
11	98112	152.73636	−4.67753	281±23	18.59±0.01	1.89±0.01	0.99±0.01	−11.24±0.03	−0.05±0.05	K3-5 I	Late K RSG, BBM2014, CaT=12.1±0.2
12	96477	152.73883	−4.67685	–	19.35±0.01	1.52±0.01	0.79±0.01	−9.91±0.03	−0.09±0.08	–	Unclassified
13	94601	152.74149	−4.66321	–	20.00±0.01	1.59±0.03	0.70±0.01	−10.15±0.03	0.30±0.05	–	Unclassified
14	90437	152.74760	−4.66993	–	20.56±0.02	1.34±0.08	0.64±0.02	−10.16±0.03	0.35±0.04	–	Unclassified
15	88681	152.75012	−4.65169	–	19.09±0.01	1.48±0.01	0.98±0.01	−10.96±0.03	0.14±0.04	M0-2 II, For.	Late M giant, BBM2014

"BBM2014" – refers to targets previously observed by Britavskiy et al. (2014). For. – Foreground giants.

Table 4.4: Characteristics and classification of observed targets in WLM.

Name	DUSTiNGS ID	R.A.(J2000) (deg)	Decl.(J2000) (deg)	RV (km s^{-1})	V (mag)	$B-V$ (mag)	$V-R$ (mag)	$M_{[3.6]}$ (mag)	[3.6] − [4.5] (mag)	Spectral class	Notes
1	81399	0.51547	−15.45649	–	22.26±0.04	0.97±0.09	1.17±0.05	−8.49±0.03	−0.09±0.11	–	Unclassified, 2 obs.
2	74034	0.52545	−15.44786	–	21.87±0.03	1.15±0.11	0.48±0.05	−8.48±0.04	−0.25±0.11	–	Unclassified
3†	77883	0.52019	−15.44624	–	–	–	–	−8.97±0.03	−0.17±0.09	–	Unclassified
4†	100786	0.49050	−15.44401	–	22.50±0.09	0.27±0.13	0.70±0.09	−6.10±0.12	0.11±0.16	–	Unclassified
5†	117303	0.46916	−15.43916	–	–	–	–	−8.87±0.04	0.29±0.08	–	Unclassified
6†	99211	0.49273	−15.43183	–	21.64±0.01	1.47±0.12	0.93±0.02	−6.83±0.20	0.61±0.25	–	Unclassified
7†	120017	0.46540	−15.42686	–	–	–	–	−8.85±0.04	0.30±0.07	Carbon star	BD2004, VAR
8†	85266	0.51034	−15.42175	–	22.33±0.05	0.31±0.07	0.48±0.06	−8.69±0.04	0.01±0.09	–	Unclassified
9†	97873	0.49439	−15.41839	–	21.42±0.02	0.50±0.03	0.89±0.02	−8.85±0.03	0.24±0.08	–	Unclassified, VAR
10†	99256	0.49260	−15.49980	–	22.61±0.03	−0.28±0.04	−0.03±0.05	−9.23±0.04	0.01±0.06	Carbon star	BD2004, 2 obs.
11†	92333	0.50126	−15.49678	–	21.39±0.02	1.58±0.06	0.96±0.02	−7.44±0.13	0.51±0.19	–	Unclassified
12†	93455	0.49988	−15.49480	–	22.14±0.02	−0.29±0.03	−0.05±0.04	−8.89±0.06	0.17±0.10	Late G	2 obs., VAR
13	78469	0.51934	−15.49346	–	21.01±0.01	1.51±0.07	0.99±0.02	−8.96±0.04	0.26±0.05	G-K	–
14	101523	0.48976	−15.48786	−142±26	19.26±0.01	1.64±0.01	0.86±0.01	−9.27±0.04	−0.07±0.06	K1-3 I	K0-1 I, LM2012, 2 obs., CaT=9.9±0.3
15†	112858	0.47521	−15.48523	–	21.01±0.01	1.60±0.03	0.96±0.01	−8.66±0.03	0.25±0.08	Back. galaxy	z=0.39, 2 obs.
16†	113729	0.47403	−15.48050	−40±3	18.83±0.01	1.50±0.01	1.03±0.01	−10.30±0.04	0.04±0.05	M1-3 II, For.	2 obs., CaT=5.2±0.1
17	106415	0.48364	−15.47721	−145±4	21.31±0.01	0.10±0.02	0.22±0.02	−7.29±0.08	0.40±0.12	Em. l. star	$H\alpha$ source, MMO2007
18	99700	0.49205	−15.46671	–	20.54±0.01	1.36±0.01	0.74±0.01	−9.28±0.03	0.33±0.04	–	Unclassified, 2 obs.

† – targets added to fill the free space on the MXU mask. Targets with the following comments are: "BD2004" – Battinelli & Demers (2004), "LM2012" – Levesque & Massey (2012), "MMO2007" – Massey et al. (2007b). "2 obs." – targets observed twice in different masks. Targets with the comment "VAR" refer to newly identified dusty variable AGB stars from Boyer et al. (2015a). For. – Foreground giants.

Table 4.5: Characteristics and classification of observed targets in WLM (continuation).

Name	DUSTiNGS ID	R.A.(J2000) (deg)	Decl.(J2000) (deg)	RV (km s^{-1})	V (mag)	$B-V$ (mag)	$V-R$ (mag)	$M_{[3.6]}$ (mag)	[3.6] – [4.5] (mag)	Spectral class	Notes
19	92197	0.50146	−15.49637	–	21.39±0.02	1.58±0.06	0.96±0.02	−8.79±0.04	-0.18±0.10	K	–
20	74091	0.52535	−15.47827	−214±14	21.68±0.01	1.64±0.15	1.18±0.02	−8.66±0.03	0.20±0.31	K	–
21†	88592	0.50603	−15.47669	–	21.81±0.02	1.55±0.11	1.11±0.03	−9.37±0.05	0.03±0.05	Carbon star	BD2004
22†	83875	0.51208	−15.46514	−145±4	–	–	–	−9.31±0.04	0.32±0.05	Unclassified	BD2004, 2 obs., VAR
23	85741	0.50967	−15.46217	−135±5	19.45±0.01	0.09±0.01	0.37±0.01	−9.54±0.03	0.63±0.04	Em. l. star	$H\alpha$ source, MMO2007
24†	96047	0.49661	−15.45020	–	21.93±0.02	−0.38±0.03	−0.02±0.03	−9.42±0.03	−0.06±0.05	Carbon star	BD2004
25†	75513	0.52343	−15.55465	–	–	–	–	−9.41±0.03	0.05±0.05	Carbon star	BD2004
26	77794	0.52028	−15.54894	–	21.45±0.01	0.56±0.02	0.45±0.01	−8.57±0.04	0.78±0.05	Quasar	z=0.62
27	58933	0.54626	−15.53583	–	20.17±0.01	1.40±0.01	0.67±0.01	−8.79±0.04	−0.02±0.08	–	Unclassified
28†	82225	0.51428	−15.52568	–	21.12±0.01	0.34±0.01	0.26±0.01	−9.28±0.03	0.26±0.05	Unclassified	BD2004, VAR
29	90598	0.50340	−15.52166	−28±11	18.69±0.01	1.78±0.01	0.91±0.01	−10.08±0.04	−0.11±0.06	K1-3 I	K0-1 I, LM2012, CaT=13.1±0.1
30	94581	0.49837	−15.51678	−44±13	18.97±0.01	1.78±0.01	0.90±0.01	−9.70±0.03	−0.10±0.06	K3-5 I	K2-4 I, LM2012, CaT=12.9±0.1
31	83414	0.51268	−15.50950	−48±16	18.67±0.01	1.97±0.01	1.04±0.01	−10.61±0.04	−0.11±0.06	K4-5 I	K5 I, LM2012, CaT=13.8±0.1

† – targets added to fill the free space on the MXU mask. Targets with the following comments are: "BD2004" – Battinelli & Demers (2004), "LM2012" – Levesque & Massey (2012), "MMO2007" – Massey et al. (2007b). "2 obs." – targets observed twice in different masks. Targets with the comment "VAR" refer to newly identified dusty variable AGB stars from Boyer et al. (2015a). For. – Foreground giants.

Table 4.6: Characteristics and classification of observed targets in WLM. P95 observing run.

Name	DUSTiNGS ID	R.A.(J2000) (deg)	Decl.(J2000) (deg)	RV (km s^{-1})	$M_{[3.6]}$ (mag)	[3.6] – [4.5] (mag)	Notes
1-P95	78491	0.519299	-15.454340		−9.36±0.04	0.45±0.05	
2-P95	79964	0.517339	-15.525577	−124±3	−9.46±0.04	0.02±0.05	Bright and blue, For.
3-P95	83414	0.512683	-15.509500	−94±6	−10.61±0.04	−0.11±0.06	K5I, LM2012, BBM2014
4-P95	83875	0.512081	-15.465138		−9.31±0.03	0.32±0.05	BBM2014
5-P95	86526	0.508648	-15.450670		−9.77±0.03	0.46±0.05	
6-P95	86598	0.508562	-15.439708	−88±13	−9.92±0.04	0.05±0.05	M5, dwarf?
7-P95	88720	0.505814	-15.487849		−9.59±0.05	0.53±0.06	
8-P95	90598	0.503403	-15.521162	−108±6	−10.08±0.03	−0.11±0.06	K0I, LM2012, BBM2014, K3I?
9-P95	94581	0.498370	-15.516783	−168±4	−9.70±0.03	−0.10±0.06	K2/3I, LM2012,BBM2014, K3I
10-P95	96709	0.495804	-15.505663		−9.44±0.04	0.34±0.05	
11-P95	97051	0.495405	-15.501128		−7.97±0.10	–	
12-P95	96974	0.495471	-15.541072		−10.13±0.03	0.41±0.05	
13-P95	97035	0.495379	-15.470988		−9.15±0.03	0.61±0.05	
14-P95	98086	0.494067	-15.435750		−9.00±0.03	0.27±0.04	
15-P95	99502	0.492291	-15.461046	16±2	−11.97±0.04	−0.12±0.05	Bright and blue, $H\alpha$
16-P95	99581	0.492176	-15.467833		−9.02±0.04	0.42±0.05	
17-P95	101111	0.490272	-15.518739		−10.02±0.04	0.56±0.05	
18-P95	103310	0.487502	-15.498477	−165±3	−9.72±0.04	−0.12±0.05	K0I, LM2012, J000157.01-152954.0
19-P95	103756	0.486942	-15.522984		−9.69±0.03	−0.13±0.05	K0I, LM2012, J000156.87-153122.3
20-P95	104054	0.486522	-15.477794	−94±7	−11.34±0.03	−0.12±0.04	K2I, LM2012, J000156.77-152839.6
21-P95	108689	0.480663	-15.512545		−11.82±0.04	−0.09±0.05	Bright and blue, For.
22-P95	114857	0.472440	-15.474608		−9.73±0.04	0.57±0.05	
23-P95	127157	0.455256	-15.529089		−9.89±0.03	−0.01±0.05	For. M3-5-type

"BBM2014" – refers to targets previously observed by Britavskiy et al. (2014), "LM2012" – Levesque & Massey (2012). For. – Foreground giants.

Table 4.7: Characteristics and classification of observed targets in IC 10.

Name/Obs. Name	DUSTiNGS ID	R.A.(J2000) (deg)	Decl.(J2000) (deg)	RV (km s^{-1})	$M_{[3.6]}$ (mag)	[3.6] – [4.5] (mag)	Notes
1	128619	4.9865770	59.2769393	44±12	−10.26±0.03	−0.04±0.05	For., B?
2	107761	5.0460181	59.3180999	19±7	−8.80±0.07	0.24±0.09	For. F-G?
3	112657	5.0324745	59.2714500	54±25	−8.84±0.04	−0.05±0.06	For., K 1-3 III
4	103677	5.0575594	59.2875137	–317±10	−9.58±0.04	−0.15±0.05	RSG1, K 3-5
5	117107	5.0198626	59.2903671	–305±13	−9.86±0.04	−0.08±0.05	RSG2, M0-2
6	96020	5.0788016	59.2634048	87±16	−10.32±0.03	0.07±0.05	For., B?
7	126841	4.9916567	59.3216438	57±10	−9.48±0.05	0.17±0.06	For., B?
8	94159	5.0840334	59.3429145	–4±6	−9.19±0.08	–	For., Late G - Early K
9	95408	5.0804367	59.3092765	–250±6	−10.71±0.04	−0.03±0.06	RSG3, M1-3
10	99773	5.0684976	59.2951965	–252±6	−9.80±0.03	−0.03±0.05	RSG4, M0-2
11	85592	5.1077690	59.3035316	–261±8	−10.08±0.03	−0.22±0.04	RSG5, M1-3
12	107961	5.0455651	59.2827033	–321±17	−10.09±0.03	−0.18±0.04	RSG6, K 3-5

For. – Foreground giants.

Among the observed targets we emphasize several groups of dusty massive stars that are described in the subsections below.

4.1 Red and yellow supergiants

In total, we identify 28 RSGs, 21 of which are new discoveries; 7 were previously published in the independent study of Levesque & Massey (2012), which used optical selection criteria. Specifically, we have identified 3 RSGs in IC 1613, 7 RSGs in Sextans A, 2 RSGs in Sextans B, 1 RSG in Phoenix, 2 RSGs in Pegasus, and 6 RSGs in IC 10.

In Figure 4.13 we show spectra of 13 identified RSGs from 4 dIrr galaxies and one candidate yellow supergiant (Sex A 4), ordered by spectral type. This sample of RSGs was observed on VLT/FORS2 spectrograph during the P90 and P91 observational runs. Most of the RSGs have K spectral type, apart from 2 M-type RSGs. The low resolution of our spectral data does not allow us to resolve individual lines, which are indicators of

Table 4.8: Characteristics and classification of observed targets in IC 1613.

Name/Obs. Name	DUSTiNGS ID	R.A.(J2000) (deg)	Decl.(J2000) (deg)	RV (km s^{-1})	$M_{[3.6]}$ (mag)	[3.6] − [4.5] (mag)	Notes
1	97761	16.237533	2.078947		−9.34±0.03	−0.12±0.05	RSG1, K1-3
2	107793	16.224805	2.099375		−9.19±0.03	−0.12±0.05	–
3	115974	16.214523	2.056277		−9.57±0.05	0.03±0.06	M0-1
4	132449	16.194620	2.060652		−9.22±0.03	−0.11±0.05	–
5	161666	16.158910	2.112404		−9.25±0.04	−0.05±0.05	RSG BBM2014
6	138020	16.187889	2.046187	−102±19	−11.92±0.03	−0.06±0.05	K1-3

"BBM2014" – refers to targets previously observed by Britavskiy et al. (2014)

Table 4.9: Characteristics and classification of observed targets in Sextans B.

Name/Obs. Name	DUSTiNGS ID	R.A.(J2000) (deg)	Decl.(J2000) (deg)	RV (km s^{-1})	$M_{[3.6]}$ (mag)	[3.6] − [4.5] (mag)	Notes
1	82970	150.017166	5.309929	390±20	−10.06±0.04	−0.07±0.06	RSG2, K1-3
2	100179	149.994064	5.326573	337±10	−10.32±0.03	0.05±0.05	RSG1, K1-3
3	120428	149.966735	5.356087	25±11	−10.65±0.04	−0.01±0.05	For., M1-3
4	94161	150.002227	5.373697	128±6	−13.41±0.05	−0.016±0.06	For., B?
5	128477	149.955780	5.338477	–	−9.95±0.03	0.05±0.05	For., M1-3

For. – Foreground giants.

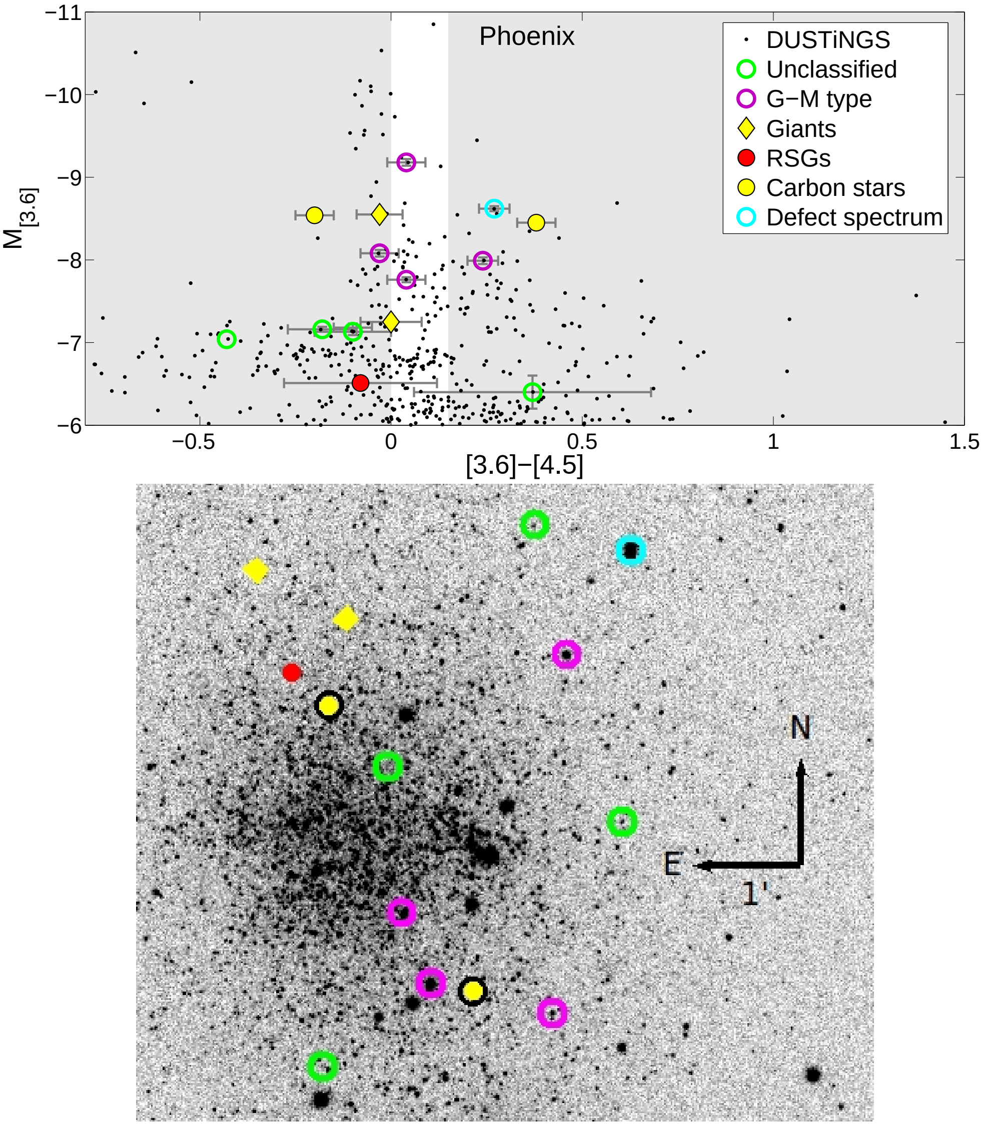

Figure 4.3: Top panel: $M_{[3.6]}$ vs. [3.6] – [4.5] CMD for the Phoenix dIrr galaxy. The stars that we have observed are labeled by different symbols according to their classification, given in Table 4.1 as explained in the legend. For each target on the CMD we indicate the error bars for the colors and magnitudes by grey lines. The regions that satisfy our selection criteria are marked in light grey (the left region corresponds to the RSGs area, the right region corresponds to the LBVs and sgB[e] area, see text for more details). Bottom panel: The spatial distribution of the observed targets, superposed on *V*-band images of the Phoenix galaxy (Massey et al. 2007c).

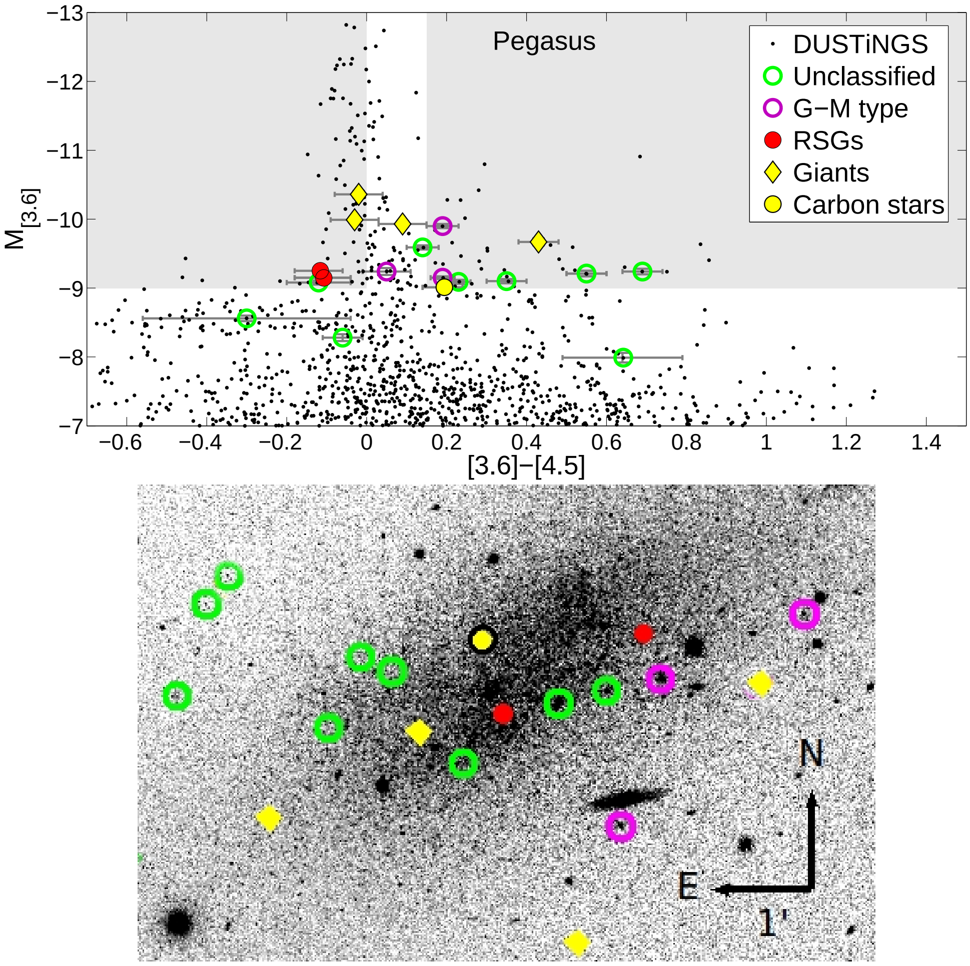

Figure 4.4: Same as Figure 4.3, but for the Pegasus dIrr galaxy. The stars that we have observed are labeled by different symbols according to their classification, given in Table 4.2.

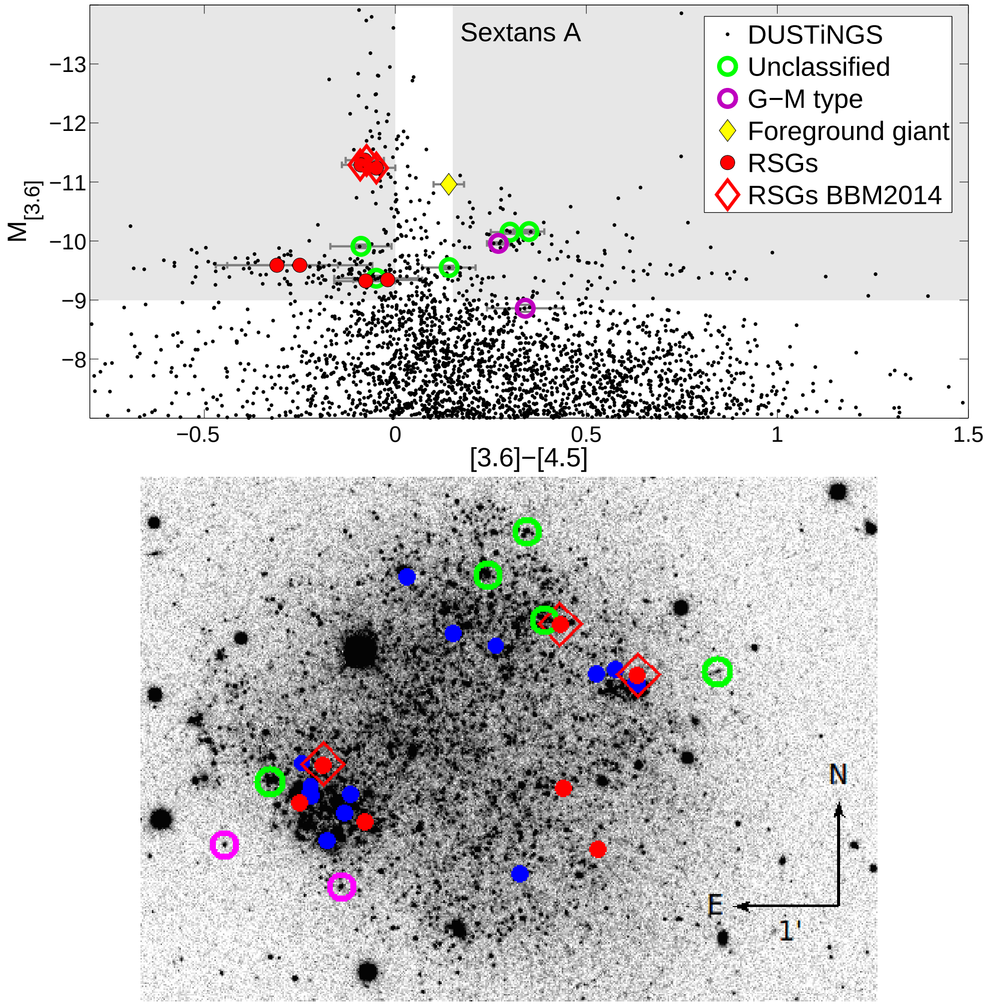

Figure 4.5: Same as Figure 4.3, but for the Sextans A dIrr galaxy. The stars that we have observed are labeled by different symbols according to their classification, given in Table 4.3. All previously known RSGs are marked by open red diamonds. The sample of blue supergiants is marked by blue colors (From Camacho et al. 2015).

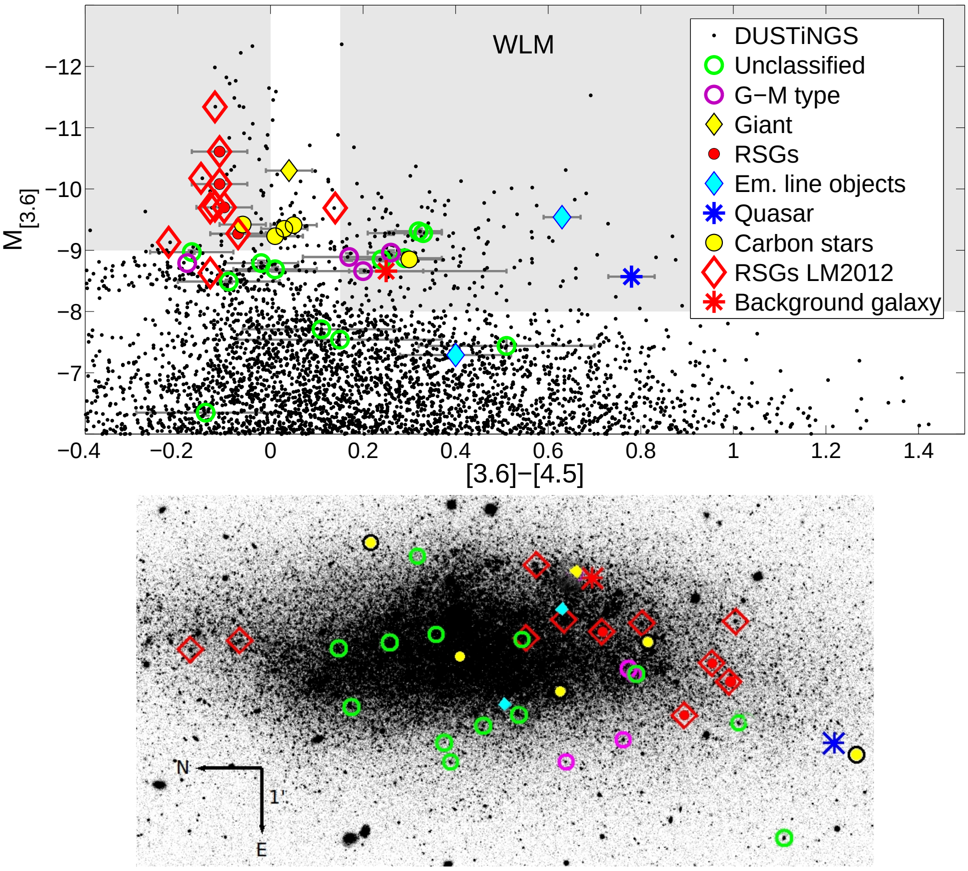

Figure 4.6: Same as Figure 4.3, but for the WLM dIrr galaxy. The stars that we have observed are labeled by different symbols according to their classification, given in Tables 4.4 and 4.5. Also, all previously known RSGs are marked by open red diamonds, emission line objects are marked by blue filled diamonds, background objects are marked by different color stars.

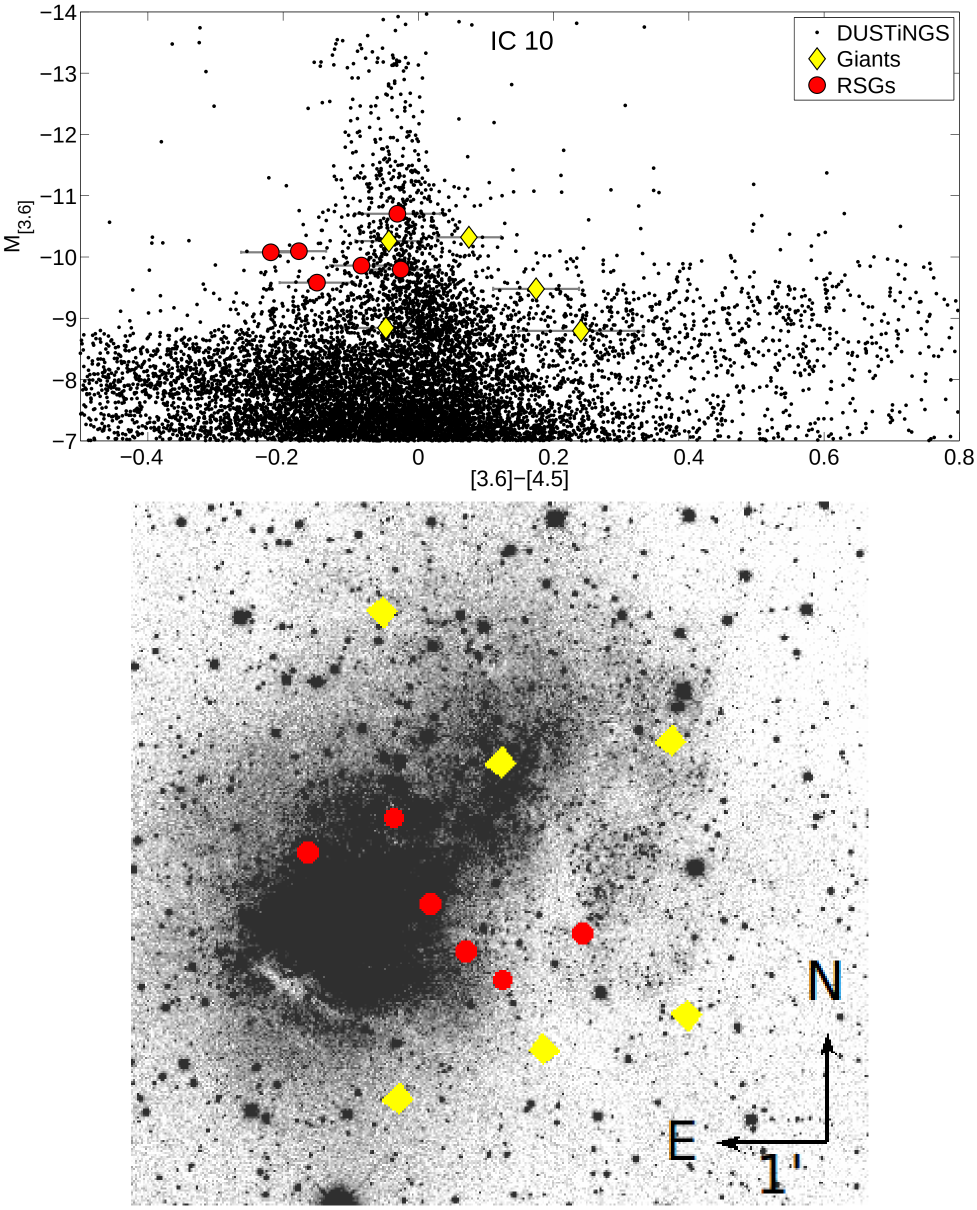

Figure 4.7: Same as Figure 4.3, but for the IC 10 galaxy. The stars that we have observed are labeled by different symbols according to their classification, given in Table 4.7.

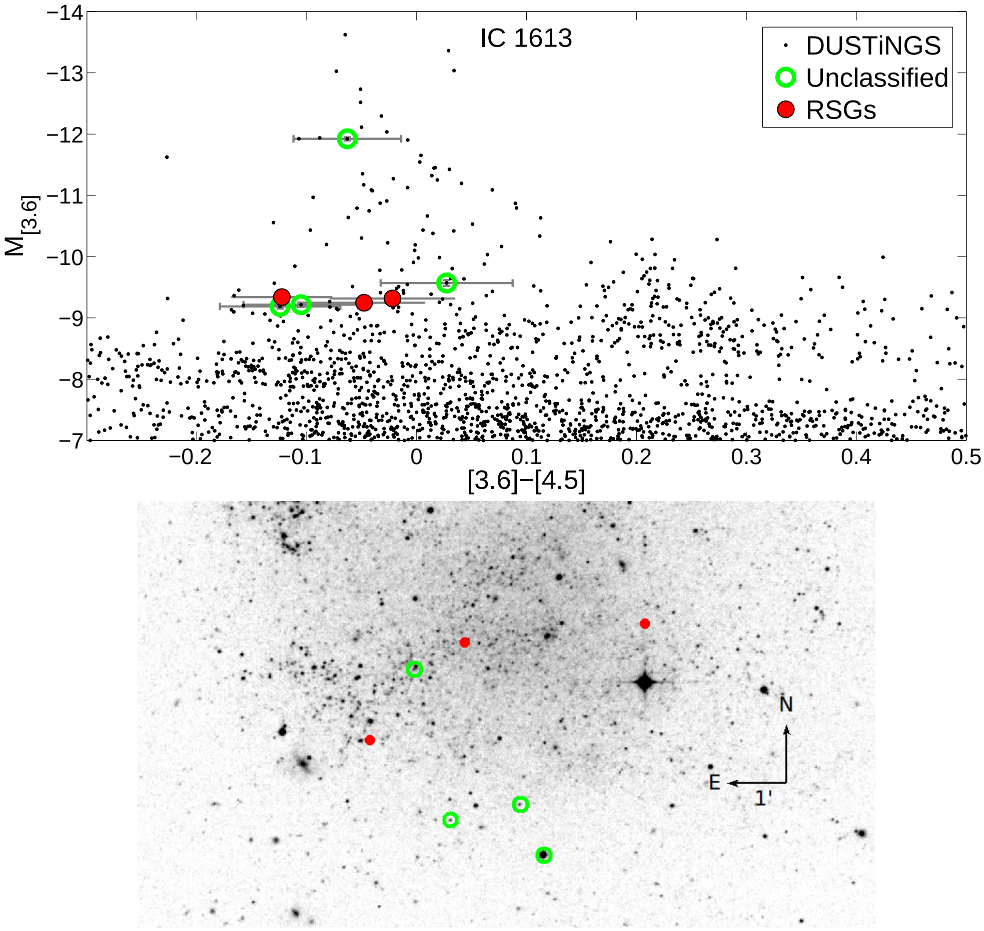

Figure 4.8: Same as Figure 4.3, but for the IC 1613 dIrr galaxy. The stars that we have observed are labeled by different symbols according to their classification, given in Table 4.8. The image taken from SuperCOSMOS Sky Survey (Hambly et al. 2001).

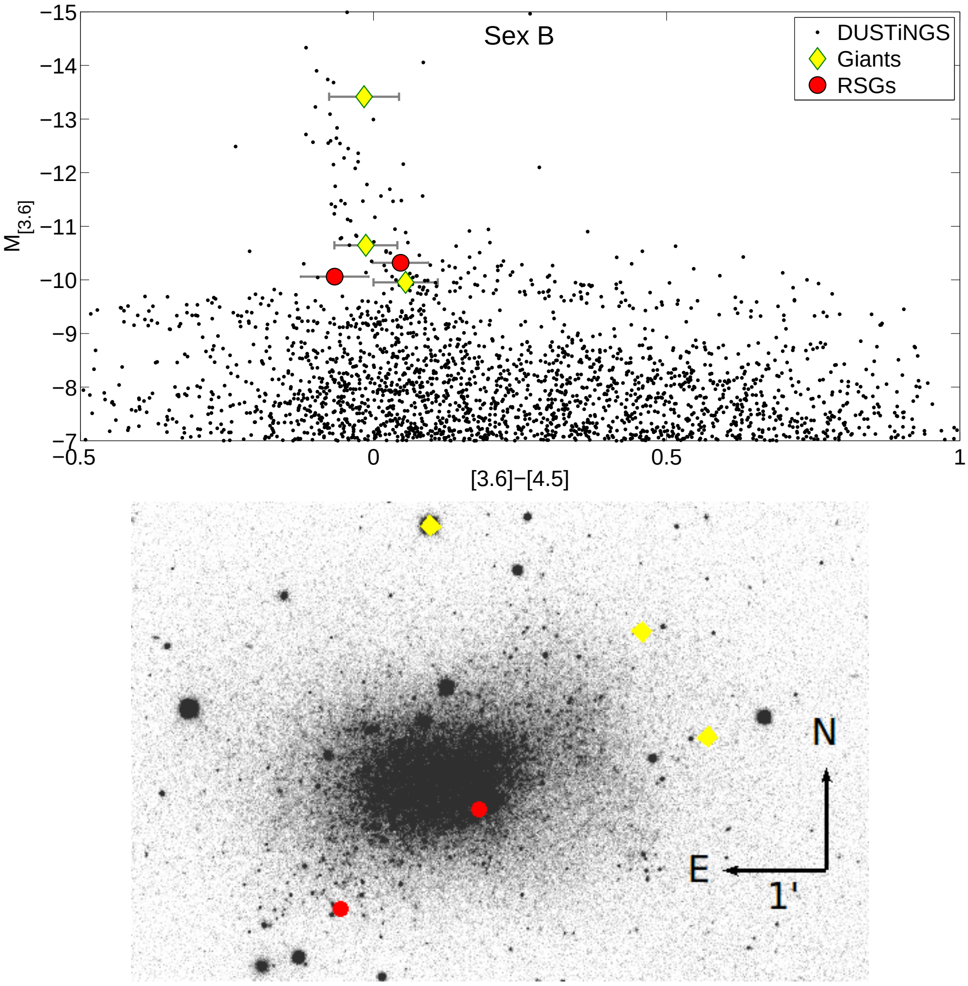

Figure 4.9: Same as Figure 4.3, but for the Sextans B dIrr galaxy. The stars that we have observed are labeled by different symbols according to their classification, given in Table 4.9.

luminosity class or spectral type. The main features that are visible is the Ca II triplet and dominant TiO bands in the optical part of RSGs spectra (see Figure 4.13). Thus, only the molecular blends are visible in the spectra. In the early-type spectrum of Sex A 4 it was possible to resolve some additional lines. An example of more detailed spectral type and luminosity class identification for red and yellow supergiants from optical wavelength range spectra can be found in Ginestet et al. (1994); Negueruela et al. (2012b); Drout et al. (2012); Britavskiy et al. (2014). The spectrum of Sex A 4 has strong hydrogen lines from Paschen series in the Ca II triplet region, however the main feature of this type, the O I 7774 Å triplet is absent. The presence of strong absorption lines of $H\alpha$ and $H\beta$ in the Sex A 4 spectrum, suggest a G or F spectral type for this target.

The positions of all spectroscopically confirmed RSGs on the CMD are predicted by our selection criteria, nevertheless, as we can see in Figure 4.6 one RSG in WLM (object J000158.14-152332.2 in Levesque & Massey 2012) is located on the "red" part ($[3.6] - [4.5] > 0.15$) of the CMD. This color behavior might be explained by a lack of molecular CO and SiO features in the [4.5] band (Verhoelst et al. 2009). Alternatively, the explanation could be found in the photometric variability of these RSGs (see Chapter 5.3).

The low radial velocity values of RSGs in WLM, namely WLM 29, WLM 30, WLM 31, in contrast with other objects from this galaxy (i.e. WLM 14, WLM 17 etc, see Tables 4.4, 4.5), as well as their spatial distribution (these 3 RSGs are located close to each other, to the south with respect to the main body of WLM, see Fig. 4.6) suggest a high rotation velocity for this galaxy. The extragalactic origin of the observed targets was determined by considering the radial velocities, together with the spectral and luminosity class determination, as radial velocities alone do not always distinguish foreground objects from extragalactic ones.

Object Sex A 3 (from GTC/OSIRIS observation set, Britavskiy et al. 2014) deserves particular attention. We included this luminous mid-IR source among our targets to explore its nature, even though this object only satisfies our luminosity selection criteria. The radial velocity analysis indicates an extragalactic nature of this star, while the comparison with the ESO spectral library and the presence of Hα reveals that this object has an F spectral type. For F-type supergiants the O I λ 7774 line is stronger than in dwarfs due to non-LTE effects (Przybilla et al. 2000) and the six hydrogen Paschen series in the region of the Ca II triplet ($\lambda\lambda$ P14 8598, P12 8750, P11 8863 and the three lines contaminated by calcium lines: P13 8502, P15 8545, P16 8665) should also be visible (Drout et al. 2012). However, the O I line is absent in the spectrum of Sex A 3 and the Paschen lines are not distinguishable. In addition, the Ca II triplet is weaker than the template spectra. We conclude that this object is most likely an extragalactic giant, but to give a definitive answer about the nature of this star it is necessary to obtain a higher-resolution spectrum.

This thesis together with Britavskiy et al. (2014, 2015), increased the sample of spectroscopically confirmed RSGs in dIrr galaxies in the Local Group by 21 (47 %) by employing mid-IR criteria. Prior to these works, there where 44 RSGs spectroscopically confirmed in dIrrs of the Local Group: 33 RSGs were known in NGC 6822 (Massey 1998; Levesque & Massey 2012; Patrick et al. 2015) and 11 RSGs were known in WLM (Levesque & Massey 2012). By applying our mid-IR selection criteria we selected 7 RSGs in WLM independently from Levesque & Massey (2012). Given two separate spectroscopic observations of these 7 objects, carried out 4 years apart, we can compare their spectral type and check for spectral variability (Massey et al. 2007a; Levesque 2010). Our spectroscopic analysis (see Tables 4.4 and 4.5 and Figures 4.14, 4.15) does not show any significant difference in spectral type.

The impact of different metallicities on the observed properties of RSGs is significant. As it was first reported in Elias et al. (1985) and Massey & Olsen (2003) for sample of RSGs in the SMC and the LMC, and later on a sample of more metal poor galaxies in the Local Group (Levesque & Massey 2012), the average spectral type of RSGs move toward earlier types at lower metallicities of host galaxies. Indeed, as we can see in Figure 4.10 taken from Levesque & Massey (2012), an average spectral type of RSGs in the Milky Way is M2, SMC RSGs have an average spectral type of K5-7, in WLM, as a most metal poor galaxy in this sample, RSGs have an average spectra type K1-3. The explanation of this effect, can be found in behavior of the TiO bands, that used as the primary indicator of spectral type classification. At lower metallicities these molecular bands become weaker, and as a result the comparison of observed RSG spectra with (Kurucz 1993) Atlas 9 models, suggests the early spectral types of RSGs.

Our sample of newly identified RSGs in more metal poor galaxies than WLM (e.g. Sextans A), follow the trend of RSG spectral types behavior described above. In Figure 4.11 we presented the histograms for newly identified RSGs, where we grouped by spectral type the number of RSGs for each program dIrr galaxy, apart from WLM.

In WLM we identified 7 RSGs but they were all already observed by Levesque & Massey (2012), therefore the corresponding histogram was analyzed by the same authors (see Figure 4.10). The majority of RSGs identified in our program galaxies have early K spectral type (see also Table 5.2), with the exception of the RSGs in IC10. This dIrr galaxy has the same metallicity as WLM ($[Fe/H] \approx -1.3$ dex), however the average spectral type in IC10 is K5-M0 while in WLM the range is K0-3. The source of this discrepancy in mean spectral type remains unclear and its worth addressing in future studies. One of the explanations could be found in different value metallicity that should be adopted for IC 10. However, due to small number statistics, it is not possible to draw firm conclusions for galaxies with fewer than 5 objects classified (e.g. Pegasus, IC 1613).

4.1.1 Foreground giants

We identified 17 K-M spectral type giants that are foreground stars in the Milky Way. Namely, 6 giants in IC 10, 3 in Sextans B, 2 giants in Phoenix, 4 giants in Pegasus, and 1 giant in both Sextans A and WLM dIrr galaxies. Due to their late spectral types they

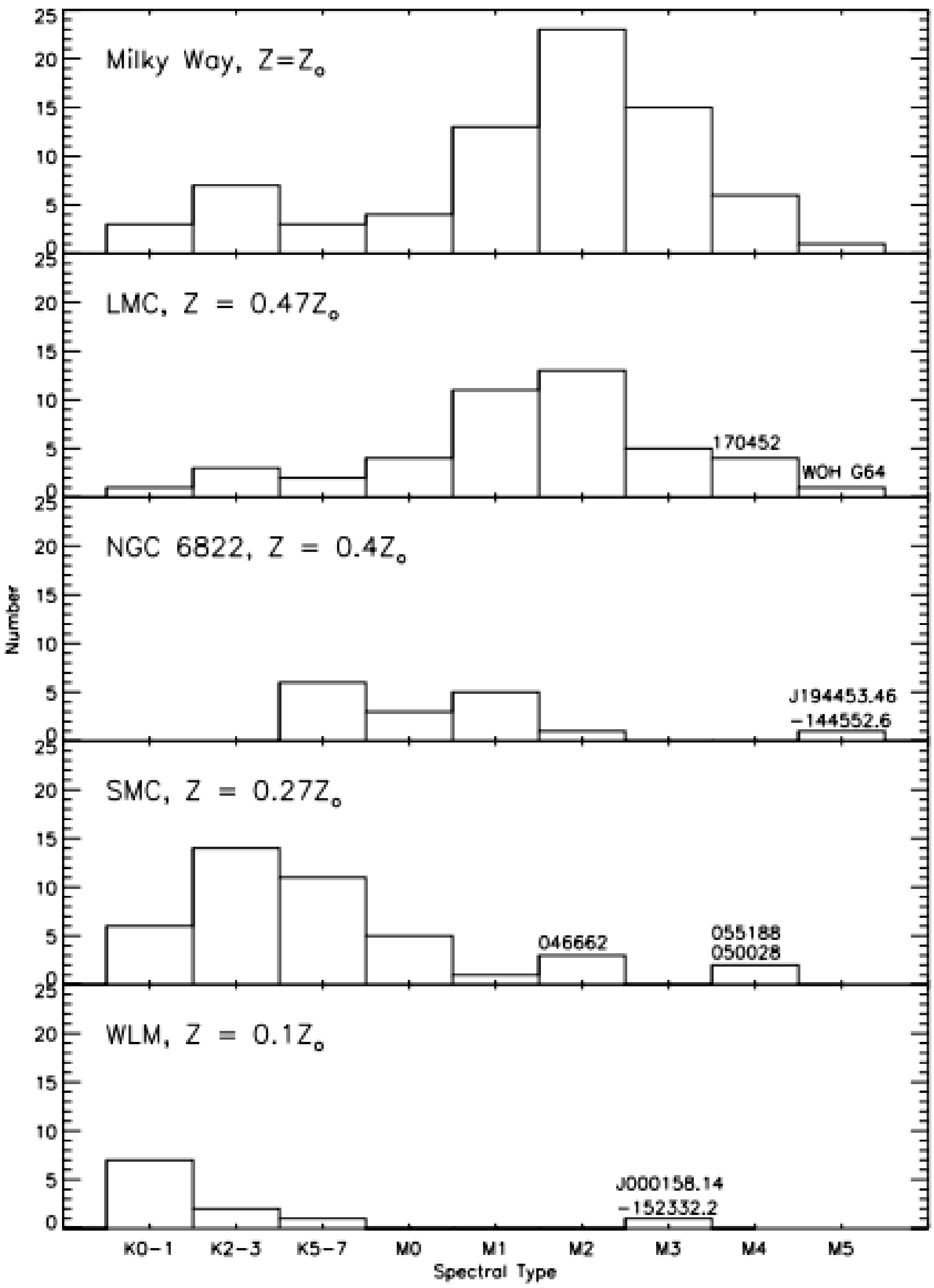

Figure 4.10: Histograms of RSG spectral types found in five different Local Group galaxies, plotted from top to bottom in order of decreasing metallicity (taken from Levesque & Massey 2012). This comparison, shows the progression of the dominant spectral type toward earlier types at lower metallicities.

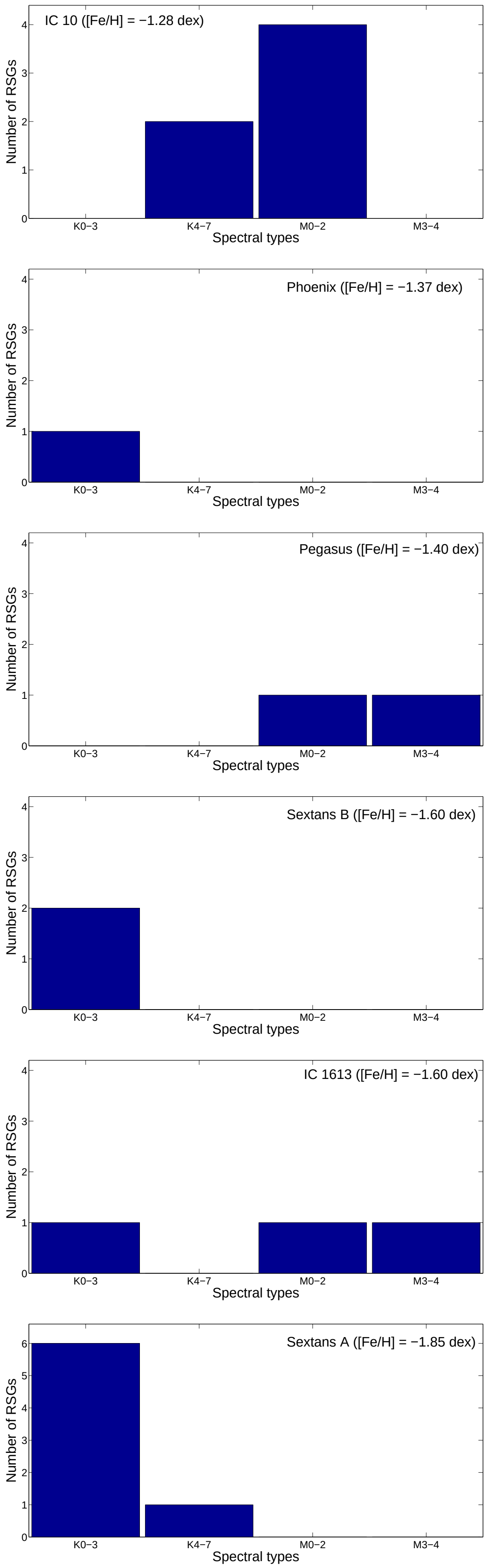

Figure 4.11: Histograms of RSG spectral types for a sample of newly identified RSGs in program dIrr galaxies. This comparison, shows the progression of the dominant spectral type toward earlier types at lower metallicities for each dIrr galaxy apart from WLM.

have the same magnitude and position on the CMD diagrams as RSGs. In the context of the mid-IR selection criteria, giants are hardly distinguishable from RSGs, as discussed further in Chapter 5. Their classification as giants was based on the relatively weak Ca II triplet and smaller radial velocities compared with RSGs in the same host galaxies.

4.2 Emission line stars

We discovered 2 rare emission line objects in WLM (WLM 17 and WLM 23), whose spectra are presented in Figure 4.16. A list of identified emission lines for each spectrum is presented in Table 4.10. Line identification was performed by using the spectral atlas of η Car (Zethson et al. 2012) and the spectral atlas of early type hypergiants, including LBVs and sgB[e] stars (Chentsov et al. 2003). The spectral resolution does not allow us to perform an accurate spectroscopic classification of these targets, neither investigate the hydrogen line profiles, however we can provide some information about the nature of these sources.

Besides strong hydrogen lines in emission, object WLM 17 has some forbidden lines of high excitation potential, such as [O II] and [Ar III], which indicate a high temperature of the stars, about $T_{eff} \approx 30\,000$ K. The presence of "nebular" lines [N II] 6583 Å and [S II] 6717 Å and 6731 Å, indicates that there is an envelope surrounding this star. The position of this object in the Hα image of WLM (Massey et al. 2007c), shows that this object lies inside an HII region. Furthermore, according to Hodge & Miller (1995), WLM 17 is located near an identified HII region, and spectroscopic features such as [O III] 5007, He I 5876, N II 6984, He I 6678, [Ar III] 7135 Å, originate from the HII region. We conclude that this object is an evolved, hot, and young massive star near an HII region.

Object WLM 23 has strong hydrogen emission, however the absence of He lines and forbidden Fe lines, indicates a lower temperature for this star, $T_{eff} < 20\,000$ K. The spectrum exhibits both the Ca II triplet and Paschen hydrogen series in emission. Furthermore, dominant Fe II emission lines in the spectrum suggest that this object is an iron star (see Section 2.2 in Humphreys et al. 2014). These two objects have been selected as candidate LBVs or sgB[e] stars ([3.6] − [4.6] > 0.15 mag, see Figure 4.6). He emission lines and forbidden lines of Fe should exist in these types of stars, but we do not detect them. By taking into account the abundance of Fe II emission lines and the high absolute magnitude ($M_{[3.6]}$ = −9.54 mag), we suggest that object WLM 23 is a hypergiant that belongs to the class of Fe II emission stars, which were defined by Clark et al. (2012). This object is the first identified Fe II emission line star in the dIrr galaxies of the Local Group.

4.3 Carbon stars

Among the bright sources in mid-IR colors, carbon stars also satisfy our selection criteria. Despite the fact that some candidates were listed in the literature as candidates for carbon stars (Battinelli & Demers 2000, 2004; Menzies et al. 2008), we still observed them to fill the free space on MXU masks. In total we observed 10 photometric candidates, 8 of which are spectroscopically confirmed as carbon stars in this work and are presented in Figure 4.17. For the other 2 carbon star candidates it was not possible to determine the spectral type. The typical spectroscopic molecular features of carbon stars, CN at 6900 – 7500 Å and 7900 – 8400 Å are detected in all spectra. For a more precise determination of the spectral type we used template spectra of various carbon stars from the SDSS-III archive. From the behavior of the dominant C2 Swan bands in the 4600 ~ 5600 Å region, we conclude that these objects are all late-type carbon stars, presumably C-N 6-7 series, which, according to the spectral classification in Keenan (1993), are equivalent to early M-type stars. For a diagnostic of the luminosity class we used the ratio of the C2 5165 Å band to Mg I 5186 Å, which suggests that these objects have a low surface gravity, $\log g < 1$, corresponding to giants. Some of the identified carbon stars are listed as newly identified variable dusty massive AGB stars, according to Boyer et al. (2015a). These

Table 4.10: Identified emission lines in WLM 17 and WLM 23

WLM 17		WLM 23	
Ion	Wavelength (A)	Ion	Wavelength (A)
$H\gamma$	4340	$H\gamma$	4340
$H\beta$	4861	–	4501
$[O\ II] + [Fe\ II]$ or	4957	$H\beta$	4861
$[O\ III]$?	4960	$Fe\ II$	4925
$[Fe\ II]$ or $[O\ III]$	5008	$[O\ II] + [Fe\ II]$	4957
$[Fe\ II]$	5045	$[Fe\ II]$	5008
$S\ II$	5453	$Fe\ II$	5020
$Fe\ II$	5582	$Fe\ II$	5170
$[Fe\ II]$	5655	$Fe\ II$	5236
$[Fe\ II]$	5871	$Fe\ II$	5277
$He\ I$	5876	$Fe\ II$	5318
$Fe\ II$	6249	$Fe\ II$	5536
$H\alpha$	6564	$Ne\ I$?	6165
$[N\ II]$	6584	$Fe\ II$	6249
$He\ I$	6678	$[O\ I]$	6300
$[S\ II]$	6717	$Fe\ II$	6458
$[S\ II]$	6731	$Fe\ II$	6518
$[Ar\ III]$	7135	$H\alpha$	6564
$He\ I$	7283	$O\ I$?	7774
$O\ II$	7321	$O\ I$	8446
–	7723	$H\ I\ P17$	8467
$S\ II$	7852	$Ca\ II$	8498
–	8565	$Ca\ II$	8542
$H\ I\ P14$	8598	$H\ I\ P14$	8600
$Ca\ II$	8662	$Ca\ II$	8662
$Fe\ II$	8674	$H\ I\ P12$	8750
$Cr\ II$	8832	$Cr\ II$	8830
$[S\ III]$?	9071	$H\ I\ P11$	8863
$Fe\ II$	9073	$Fe\ II$	8929
		$H\ I\ P10$	9014
		$H\ I\ P9$	9229

Controversial line identifications are indicated by a question mark.

targets are labeled with a comment "VAR" in Tables 4.1 − 4.5.

4.4 Background objects

We identified two objects among the WLM targets that belong to the background: a quasar (WLM 26) and a background galaxy (WLM 15). By using template spectra from the SDSS-III archive (Data Release 9, Ahn et al. 2012) we determined the redshift of the quasar to be z = 0.62 based on the Hβ and [O III] lines and the redshift of the galaxy is estimated to be z = 0.39 based on the Ca II 3968 Å line. The spectra of these two objects are presented in Figure 4.18. The absence of emission lines in the spectrum of the galaxy implies that it is an early type galaxy, according to the SDSS-III classification. One of the applications of these objects could be as probes of the interstellar medium in WLM (an example of using radio pulsars for this purpose is presented in Kondratiev et al. 2013). Also, background quasars can be used to determine the proper motion of dIrr galaxies in the Local Group, as done in the Magellanic Clouds (Kozłowski et al. 2013).

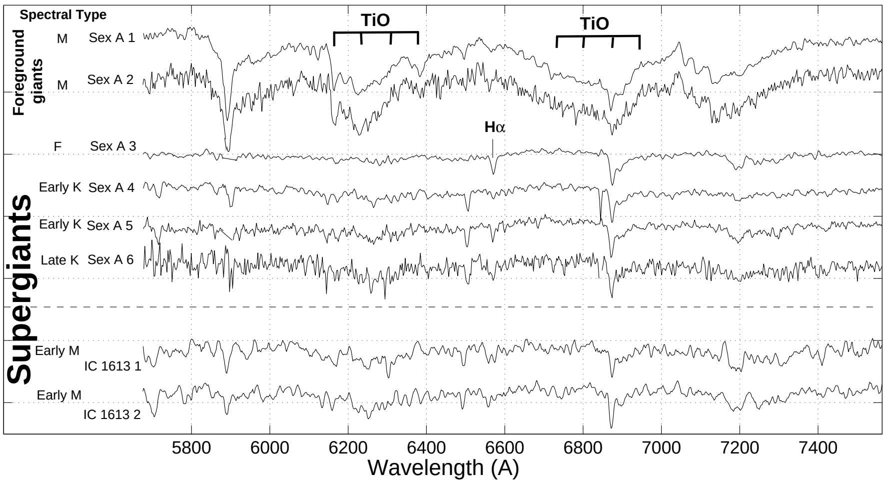

Figure 4.12: Spectra of our eight program stars which were observed with the GTC/OSIRIS and du Pont/WFCCD spectrographs, in the optical range ordered by spectral type, showing the evolution of the TiO bands from early to late spectral types (Britavskiy et al. 2014).

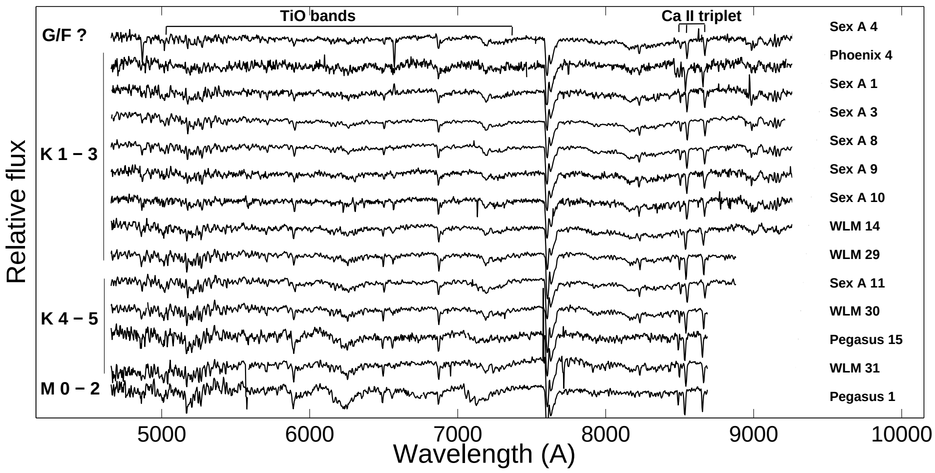

Figure 4.13: Spectra of 13 RSGs and one candidate yellow supergiant (Sex A 4), which were oberved on VLT/FORS2 spectrograph, in the optical range, ordered by spectral type, labeled on left. Names are given on right. The region where TiO bands dominate, along with the Ca II triplet are marked (Britavskiy et al. 2015).

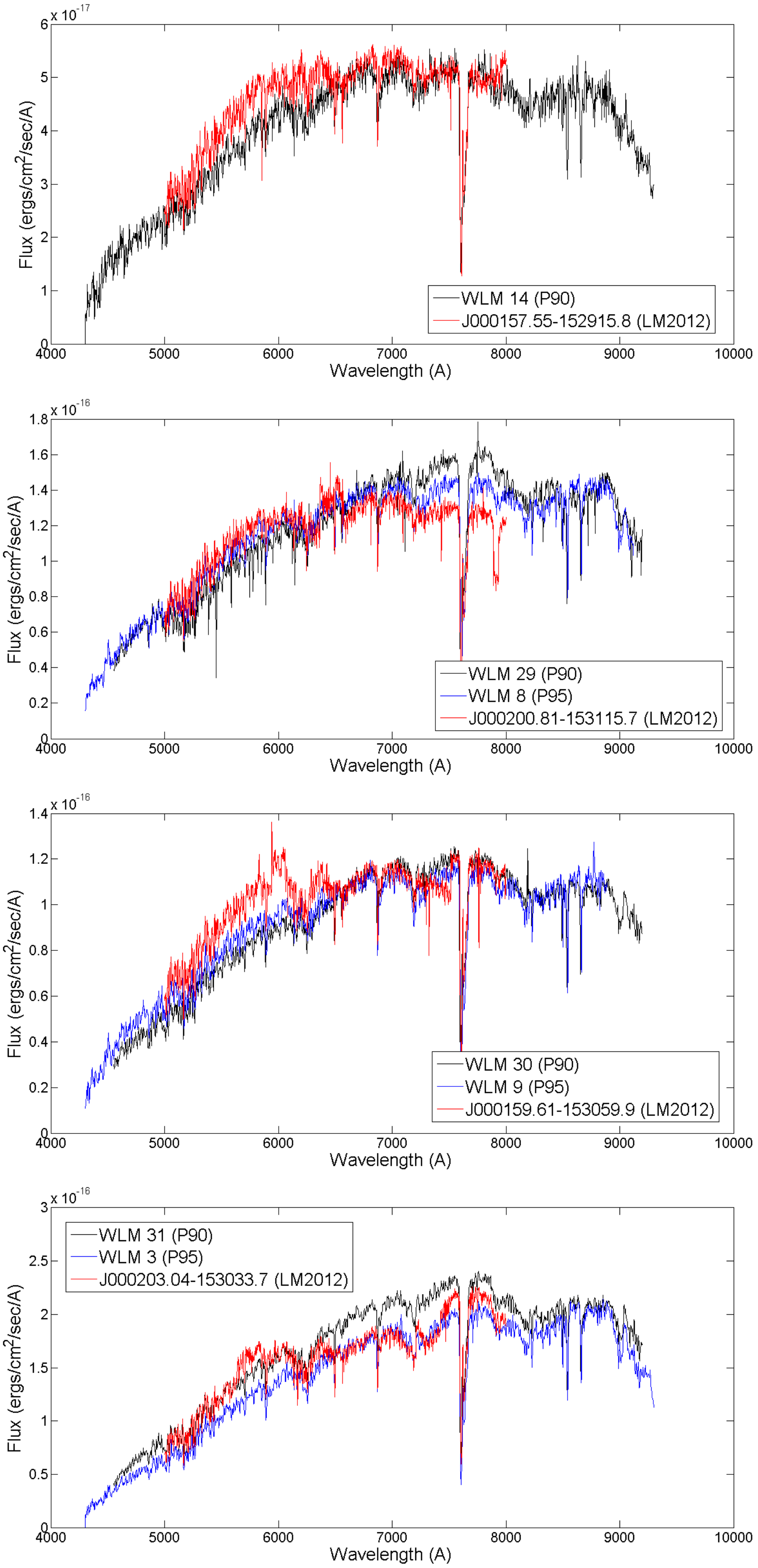

Figure 4.14: Comparison of 4 FORS2 spectra (P90 and P95 observational run) out of 7 previously known RSGs in WLM with the spectra of Levesque & Massey (2012) (red).

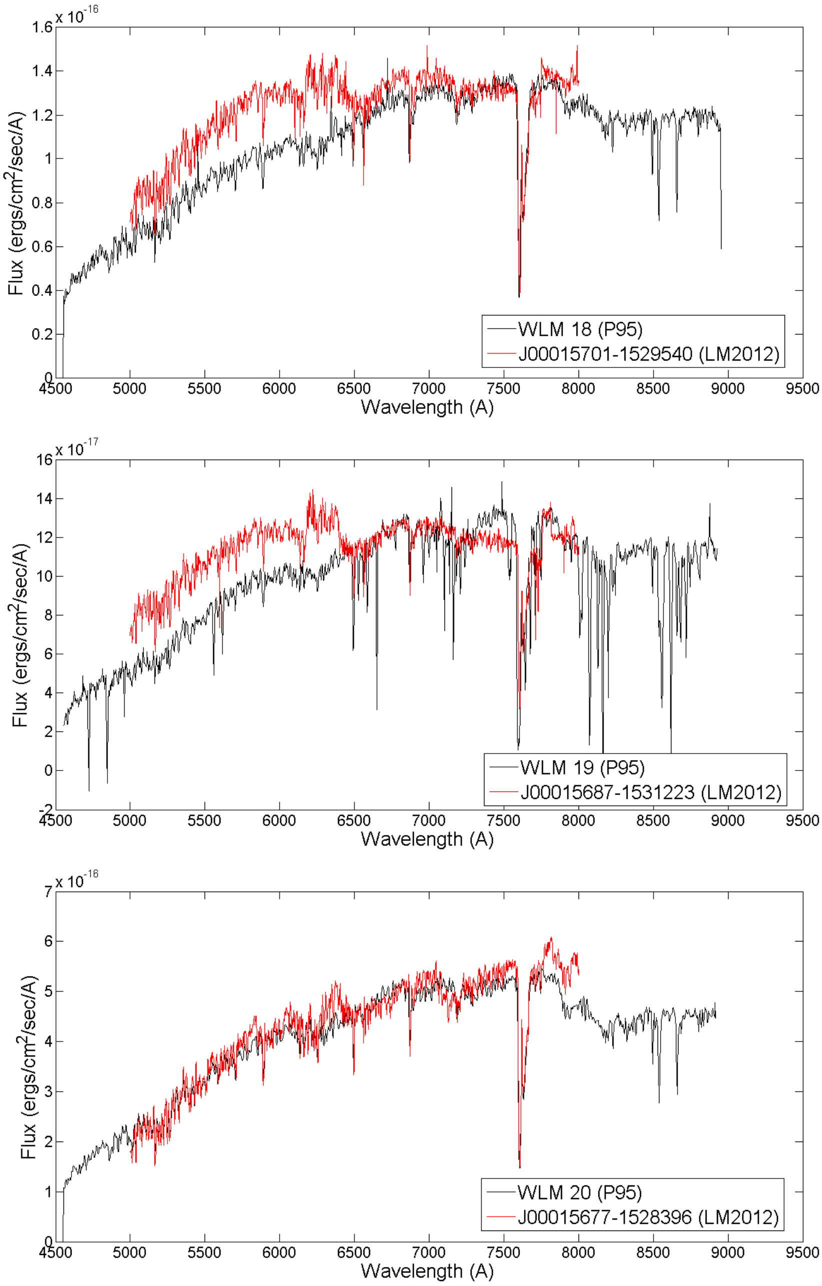

Figure 4.15: Comparison of 3 FORS2 spectra (P95 observational run) out of 7 previously known RSGs in WLM with the spectra of Levesque & Massey (2012) (red).

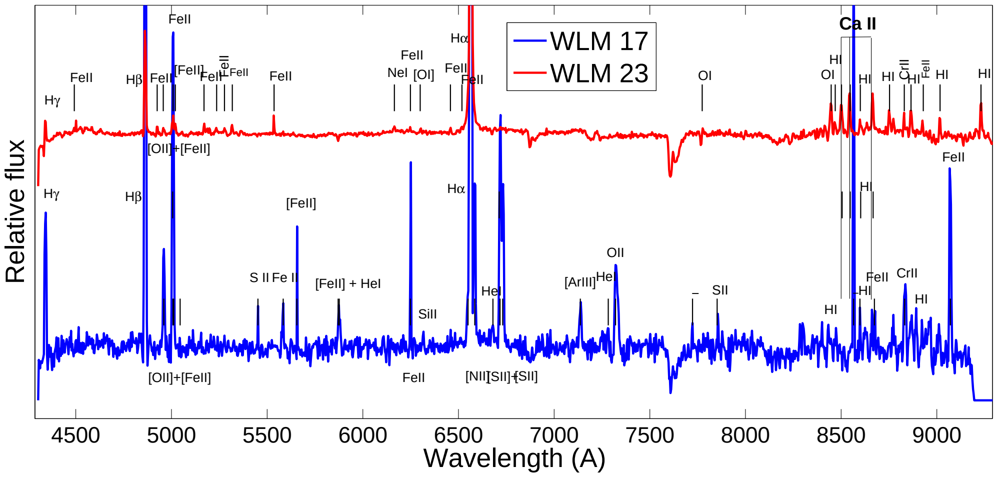

Figure 4.16: Normalized spectra of 2 emission line objects from WLM. Prominent spectral features are labeled.

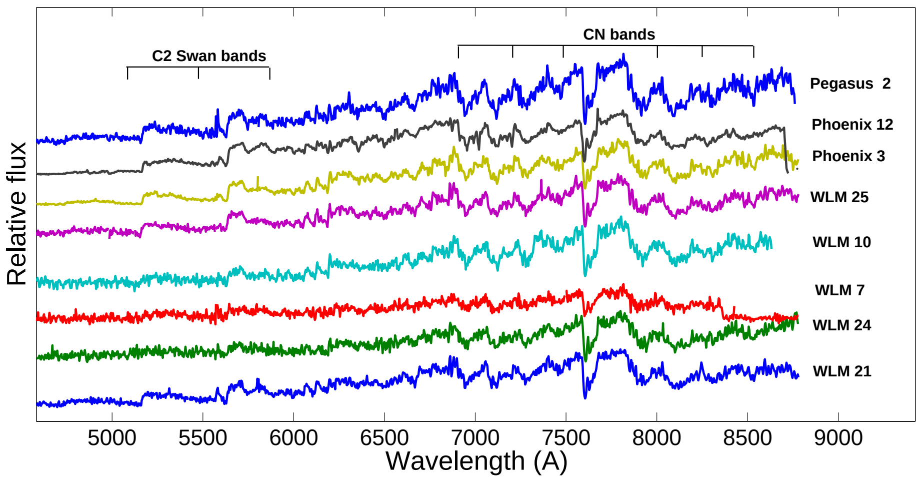

Figure 4.17: Spectra of all carbon stars in our sample, with the main molecular features labeled.

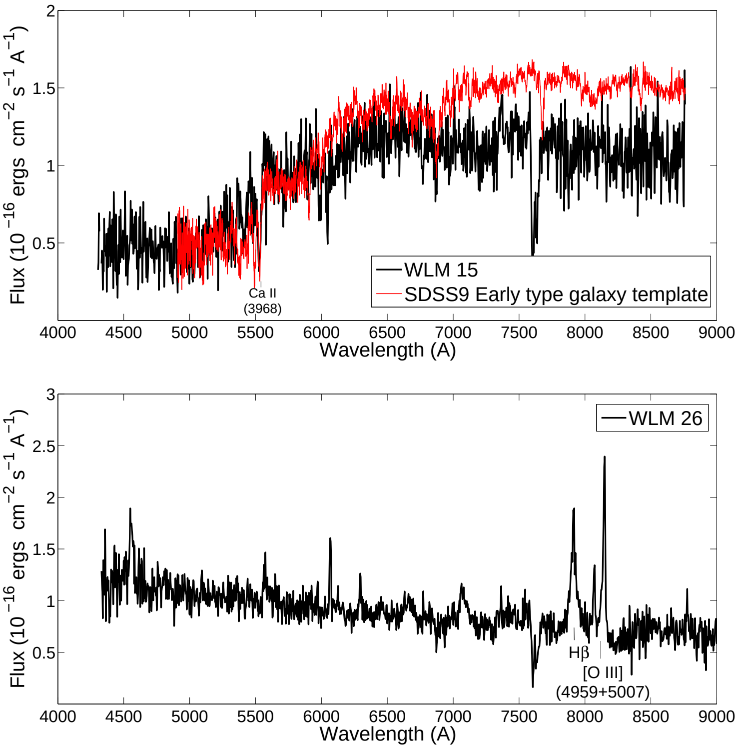

Figure 4.18: Spectra of the background galaxy WLM 15 (upper panel) and quasar WLM 26 (lower panel). An SDSS-III early-type galaxy template (red) is superposed on the spectrum of WLM 15 (black).

Chapter 5

Results and discussion

5.1 RSG selection criteria

To validate our target classification in Britavskiy et al. (2014) we used photometry from the optical *UBVRI* survey conducted for Sextans A by Massey et al. (2007d) and unpublished photometry for IC 1613 (M. Garcia, private comm.) described in Garcia et al. (2009). In Fig. 5.1 we present a $B - V$ versus $V - R$ diagram for Sextans A, indicating targets that have been observed in Britavskiy et al. (2014) except for IC 1613 1, because accurate photometry does not exist for this target. Moreover, we plotted on the same diagram the RSGs that have been identified in Sextans A by Britavskiy et al. (2015). All targets that were selected as massive star candidates are marked by green squares. Massey (1998) showed that stars with a high $B - V$ value at a given $V - R$ are expected to be supergiants, and therefore these colors are a useful tool for distinguishing supergiants from foreground giants, although in practice the method is not 100% efficient. We found that the objects Sex A 4, 5, 6, and IC 1613 2 occupy the supergiant region on this color-color diagram, while the objects Sex A 1 and 2 are found below the supergiant sequence, as expected for foreground objects. The object Sex A 3 remains controversial. The position of this object on the diagram, compared with the location of RSGs, indicates a higher

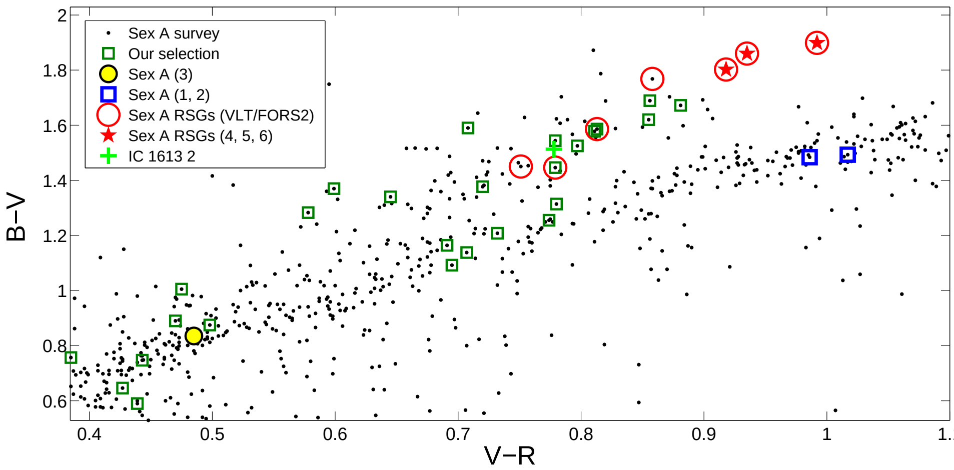

Figure 5.1: Two-color diagram for stars in Sextans A (from Massey et al. 2007c), which is a useful tool for distinguishing RSGs from foreground giants (Massey 1998). The positions of our investigated targets are labeled using different symbols. All targets in Sextans A that satisfy our selection criteria are marked by green squares. The RSGs that have been observed with VLT/FORS2 spectrograph (Britavskiy et al. 2015) are marked separately by red open circles, the other targets have been observed on GTC and du Pont telescope (Britavskiy et al. 2014).

surface gravity and earlier spectral type for this object, which is consistent with an F-type giant.

5.2 Revision of RSG Selection Criteria

Since the main goal of this work was to identify as many dusty massive stars as possible, the critical question is the efficiency of the selection criteria. The discovery of new RSGs and emission line stars provides an opportunity to test the success rate of our criteria. In Table 5.1 we present the classification of targets in each program galaxy. We provide the following seven categories: (i) "Unclassified" – targets mainly with low S/N spectra, for which we were not able to provide a classification; (ii) "Spectral type only" – targets for which only the spectral type identification was performed; (iii) "Giants" – foreground giants; (iv) "RSGs"; (v) "Em. line objects" – emission line objects; (vi) "Background objects" – quasar (WLM 26) and background galaxy (WLM 15); (vii) "Carbon stars". The number of targets satisfying our selection criteria are marked in bold font, while the number of targets that were randomly selected to fill the free space on the MXU masks are listed in parentheses. The percentage of the selected targets belonging to each of these categories is listed in the last line of the table. The percentage of evolved massive targets is 35% for RSGs and 3% for emission line objects. The accuracy of the mid-IR photometry that was used for the selection process is likely responsible for the low percentages. Also, we expect that evolved massive stars exist among the "unclassified" and "spectral type only" targets, which we could not identify due to absence of the Ca II region in the observed spectra. Moreover, among the "Unclassified" spectra there are some targets that lie on the red part of the CMDs ($[3.6] - [4.5] > 0.2$ mag). These targets could be extreme (dusty) AGB stars, especially the targets for which the spectra are very noisy.

Among our sample of dIrr galaxies the most numerous class of spectroscopically confirmed dusty massive stars is RSGs. We can compare the success of the mid-IR photometric selection criteria with the "classical" optical selection criteria (Massey 1998; Levesque & Massey 2012). Massey (1998) presented the first attempt to provide a tool to distinguish RSG candidates from foreground stars. Using the Kurucz (1992) ATLAS9 stellar atmospheres, it was shown that it is possible to separate RSGs from foreground giants from a two-color diagram ($B - V$ vs. $V - R$). The least-squares model fit, in the formalism of the B, V and R bands, for separating RSGs from foreground contaminants is: $B - V = -1.599 \times (V - R)^2 + 4.18 \times (V - R) - 1.04 + \delta$. The empirical coefficient δ is added to fit the positions of spectroscopically confirmed RSGs in the program galaxies. Massey (1998), Massey et al. (2009), and Drout et al. (2012) adopted $\delta = 0.1$ by fitting the positions of spectroscopically confirmed RSGs in NGC 6822, M31 and M33. All targets that lie above this curve are considered to be candidate RSGs, while targets below the line are considered to be foreground contaminants. The generalization of this dividing curve as a line $B - V = 1.25 \times (V - R) + 0.45$ has also been used in Levesque & Massey (2012).

In Figure 5.2 we plot all identified RSGs and giants for all program galaxies, including 2 RSGs in IC 1613, 3 in Sextans A from Britavskiy et al. (2014), 11 RSGs in WLM from Levesque & Massey (2012), and 26 in NGC 6822 from Levesque & Massey (2012); Patrick et al. (2015), on both the optical $B - V$ vs. $V - R$ two-color diagram and the mid-IR color-magnitude diagram. For targets in NGC 6822 we used *Spitzer* photometry at [3.6] and [4.5] bands from Khan et al. (2015). Optical colors are taken from Massey et al. (2007c). On the two-color diagram we show both the empirical parabolic curve and the line, discussed above, for separating RSGs from the giants. To compare how the positions of our RSG sample match these cut-off criteria, we calculate the probability density function (PDF) of the position of RSGs on the $B-V$ vs. $V-R$ color magnitude by using a gaussian kernel density estimation. In Figure 5.2 we indicate the contours of the 1σ PDF of the location of RSGs and foreground giants on the mid-IR CMD (upper panel), and on the optical two-color diagram (lower panel). The colorbar corresponds to the relative value of the probability density that RSGs are located in this specific region. We find that all RSGs are grouped in the narrow region predicted on the two-color diagram, above the empirical cut-off lines. Moreover, the 1σ interval of the PDF for the RSG region completely agrees with this parabolic equation. Our analysis indicates that both linear and parabolic cut-off lines (from Massey 1998) can be applied as a tool to separate RSGs from foreground giants. Taking into account that we plotted RSGs from different galaxies with slightly different metallicities, we provide evidence that this dividing line is universal and might be used for all galaxies for which precise optical photometry does exist.

The situation is different with the mid-IR selection criteria. As we see from the upper panel of Figure 5.2, the RSGs have a large dispersion, and a high probability of foreground contaminants (as shown by the 1σ contour of the PDF of the foreground giants from our sample). These effects make our mid-IR selection criteria less efficient than the optical colors as a tool for separating RSGs from foreground giants. Furthermore, the cutoff line $[3.6] - [4.5] < 0$ that we used for selection, does not include all spectroscopically confirmed RSGs. To generalize this statement we plotted all spectroscopically confirmed RSGs in the SMC: 59 from Bonanos et al. (2010), 83 from González-Fernández et al. (2015), and the LMC: 96 from Bonanos et al. (2009), 96 from González-Fernández et al. (2015) together with RSGs from our sample of dIrr galaxies in Figure 5.3. We plot the WISE W1 (3.353 μm) and W2 (4.603 μm) photometry of the RSGs from González-Fernández et al. (2015), which are very close to the *Spitzer* [3.6] and [4.5] bands. We find the majority of new RSGs in the SMC and the LMC to be fainter compared with the previously known RSGs. The difference in absolute magnitude is likely due to the fact that the WISE photometry has better sensitivity, despite worse resolution than the *Spitzer* photometry for the Magellanic Clouds. Also, there is a difference in the $[3.6] - [4.5]$ colors for the RSGs in the LMC vs. SMC. The maximum (peak) of the PDF for RSGs from the LMC has a bluer color ($[3.6] - [4.5] = -0.17$ mag) and brighter magnitude ($M_{[3.6]} = -10.15$ mag) than the position of the maximum PDF for the RSGs from the SMC ($[3.6] - [4.5] = -0.02$ mag, $M_{[3.6]} = -9.51$ mag). This difference, originates in the different metallicities of the LMC and the SMC, which affect the depth of CO bands at [4.5] μm, and as a result the $[3.6] - [4.5]$ color.

We added the same sample of RSGs from the Magellanic Clouds on the optical two-color diagram (lower panel of Figure 5.3). Optical colors for this sample of RSGs are taken from Massey (2002). For such a big sample of RSGs we can see a big scatter of their position on the two-color diagram, which is mainly due to the accuracy of the optical photometry. Nevertheless, the majority (≈ 70 %) of spectroscopically confirmed RSGs satisfy the optical selection criteria. Comparing this success rate in the optical selection criteria with a number of RSGs that satisfy the mid-IR selection criteria (≈ 90

%), we can conclude that the mid-IR selection criteria are useful for selecting dusty massive stars, however these criteria are not so efficient for separating them from foreground contaminants, in contrast with the optical selection criteria (as shown in Figure 5.2).

We find that RSGs group in a broader region in the mid-IR CMD, in contrast to the narrow region defined on the optical two-color diagram, which makes optical selection criteria more reliable, when high-quality optical photometry exists for the investigated galaxies. However, the mid-IR criteria are useful for the large number of galaxies with *Spitzer* imaging that lack deep optical photometry.

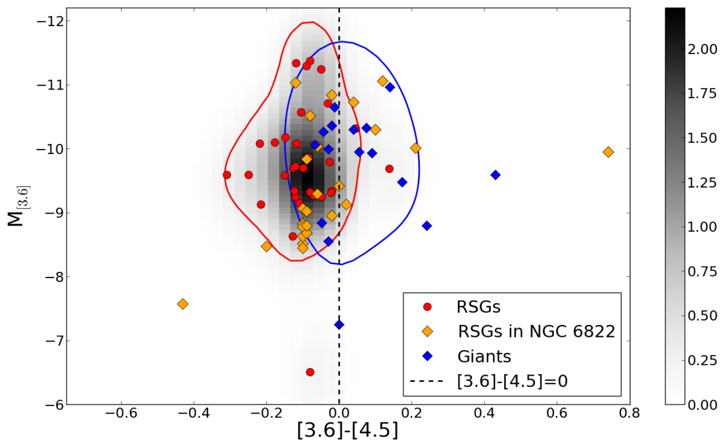

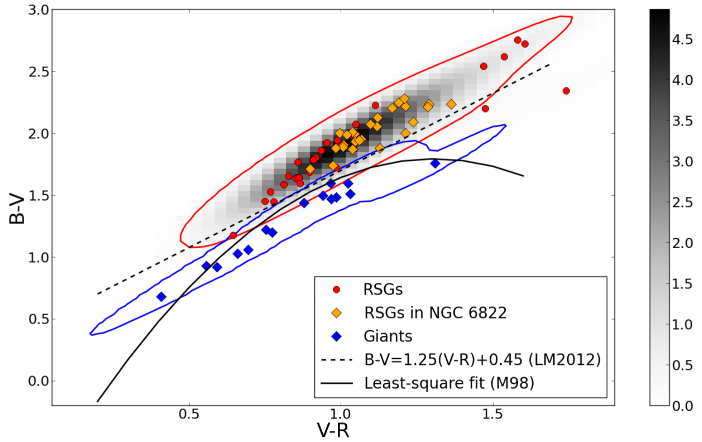

Figure 5.2: $M_{[3.6]}$ vs. [3.6] – [4.5] CMD (upper panel) and two-color optical diagram (lower panel) for all spectroscopically confirmed RSGs and giants in our 7 program galaxies, including known RSGs from literature in WLM (Levesque & Massey 2012), NGC 6822 (Patrick et al. 2015). RSGs in NGC 6822 are marked separately, due to the different source mid-IR photometry. RSGs are labeled by red filled circles, giants are labeled by blue filled diamonds, the color contours correspond to a 1σ dispersion of the gaussian PDF. The probability density function for the whole sample of RSGs is shown in gray, the colorbar corresponds to relative value of the PDF. The dashed line at [3.6] – [4.5] = 0 demarcates our mid-IR selection criteria for identifying RSGs. The dashed line on the two-color diagram corresponds to the empirical dividing line that separates RSGs from foreground giant candidates defined in Levesque & Massey (2012). The solid line corresponds to a least-square fit model of separating RSG candidates from foreground candidates, provided in Massey (1998).

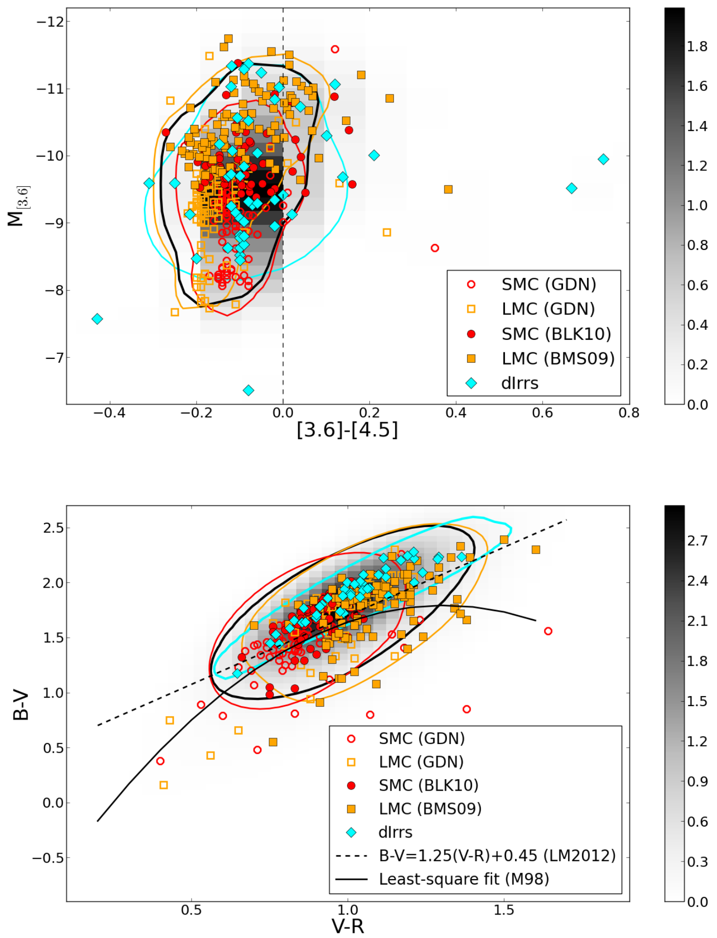

Figure 5.3: $M_{[3.6]}$ vs. $[3.6]-[4.5]$ CMD (upper panel) and $B-V$ vs. $V-R$ diagram (lower panel) for spectroscopically confirmed RSGs in 6 Local Group dIrrs (Phoenix, Pegasus, Sextans A, WLM, IC 1613 and NGC 6822), the LMC, and the SMC. The RSGs from González-Fernández et al. (2015) have a label "GDN"; RSGs with labels "BLK10" and "BMS09" are from Bonanos et al. (2010, 2009) respectively. The color contours correspond to a 1σ dispersion of the PDF for all RSGs for each galaxy, respectively. The black contour corresponds to a 1σ dispersion for the PDF of all RSGs in listed galaxies. The probability density function for all RSGs is marked in gray, the colorbar corresponds to relative values of the PDF. The dashed line at $[3.6]-[4.5] = 0$ demarcates our selection criteria for identifying RSGs. The dashed line and the solid line on the two-color diagram have the same meaning as in Figure 5.2. Optical photometry for RSGs in the Magellanic Clouds is from Massey (2002).

Table 5.1: Summary classification of our 104 observed targets (apart from P95 run observations).

ID	All observed targets	Unclassified	Spectral type only	Giants	RSGs	Em. line objects	Background objects	Carbon stars
Pegasus	**11** (+8)	**2** (+7)	**3**	**4**	**2**	**0**	**0**	(+1)
Phoenix	**2** (+12)	**0** (+5)	**2** (+2)	**0** (+2)	**0** (+1)	**0**	**0**	(+2)
Sextans A	**15**	**5**	**2**	**1**	**7**	**0**	**0**	(0)
WLM	**15** (+16)	**5** (+8)	**3** (+1)	**0** (+1)	**4**	**2**	**1** (+1)	(+5)
IC 10	**12**	**0**	**0**	**6**	**6**	**0**	**0**	**0**
IC 1613	**8**	**3**	**2**	**0**	**3**	**0**	**0**	**0**
Sextans B	**5**	**0**	**0**	**3**	**2**	**0**	**0**	**0**
Total	**68** (+36)	**15** (+20)	**12** (+3)	**14** (+3)	**24** (+1)	**2**	**1** (+1)	(+8)
%	**100**	**22**	**18**	**21**	**35**	**3**	**1**	–

The number of targets that satisfy our selection criteria are marked by bold font. Targets that were randomly selected to fill the MXU slits are given in parentheses.

5.3 Contamination from other luminous sources

The most probable contaminants of normal RSGs on the mid-IR CMDs, given our selection criteria, are the AGB stars and, in particular, the super-AGB stars (Garcia-Berro & Iben 1994; Herwig 2005). Messineo et al. (2012) provided new criteria to separate RSGs and LBVs from AGB stars, which are based on near-IR indices, $Q1$ and $Q2$. These indices measure the deviation from the reddening vector in the $H - K_s$ versus $J - K_s$ plane and the $J - K_s$ versus $K_s - [8.0]$ plane, respectively. We applied this technique in Britavskiy et al. (2014) to our sample of sources (see Table 3.1) and found that six targets satisfied the proposed criteria for RSGs. The range of these parameters for RSGs should be $0.1 < Q1 < 0.5$ and $-1.1 < Q2 < 1.5$. The exceptions are the object Sex A 3 (in Britavskiy et al. 2014), for which we have no precise [8] color.

The general conclusion that we can make is that during the selection process it is very important to consider contamination by oxygen-rich AGB stars, because there is an overlap in color indices (especially in $[3.6] - [4.5]$) between LBVs and AGBs and in both color indices and luminosities for RSGs and super-AGB stars as well. Nevertheless, there is a spectroscopic indicator of AGB stars; the line Li I 6708 Å should be visible in high-resolution spectra of O-rich AGB stars and may be used as a reference line for distinguishing AGB stars from RSGs (García-Hernández et al. 2013).

5.4 Variability

Another effect that we took into account is the variable nature of massive stars (e.g. Kourniotis et al. 2014). Szczygieł et al. (2010) showed that the majority of the identified variable massive stars in the LMC are RSGs, while the RSGs and AGB stars in M33 have been the subject of variability studies in the near-IR (Javadi et al. 2011) and mid-IR (McQuinn et al. 2007). RSGs and AGB stars often have a quite similar long-period variable (LPV) nature (Wood et al. 1983). In fact, it is possible to separate RSGs from AGB stars by using the difference in variability properties, which is important for the luminosity of super-AGB stars that can contaminate our sample. The distinction is based on the difference of absolute K magnitude against variability period for these groups of stars (see Fig. 2 in Wood et al. 1983). Another difference between supergiants and AGB stars is in the amplitude of their variability. The AGB stars have a larger variable amplitude than RSGs. Variability does affect the color indices through a pulsation cycle, thus we may obtain different conclusions about the nature of a star depending on the observational epoch. The variable nature of massive stars might be connected with the phenomenon of unusual spectral type of RSGs with respect to the average spectral type among the host galaxy (discussed in Levesque 2010; Levesque & Massey 2012). The effect consists in a progression of the dominant spectral type toward earlier types at lower metallicities.

5.5 Dusty massive stars beyond the Local Group

Our mid-IR selection criteria were applied by Williams et al. (2015) to the galaxy M83, to identify the RSG candidates. M83 is outside the Local Group at a distance of ≈ 4.8 Mpc. It has the fifth highest $H\alpha$ luminosity in the local 11 Mpc volume (Kennicutt et al. 2008). The large $H\alpha$ luminosity is an indication of a high star formation rate (Murphy et al. 2011). M83 has also been host to six historical SNe, five of which have been identified as core-collapse supernovae. These points of evidence indicate M83 has a rich supply of massive stars. The RSG candidates in M83 have been selected via a process starting with objects identified initially by their position on a [3.6] versus [3.6] – [4.5] CMD (see Figure 2.3). Then, the final sample of candidates were selected based on a CMD of [3.6] versus $J-[3.6]$, where massive stars exist in regions with $M_{[3.6]}$ fainter than -12 mag. and $J-[3.6] > 1.0$ according to Figure 2.4. Also, candidates from photometry were visually checked in the *Hubble Space Telescope* images, in order to select isolated, point sources candidates. This additional check prevented contamination by young massive clusters.

For spectroscopic follow up of RSG candidates, the VLT/KMOS instrument was used (Proposal ID: 095.D-0189, see Appendix for details). In total we selected 18 targets in the central region of the galaxy M83. The observations were performed in J-band, which is ideal for objects that are bright in the mid-IR.

As was shown by Gazak et al. (2014) for a resolving power R≈3000, prominent spectral features of Fe I $\lambda\lambda$ 1.198 and 1.189 μm and Mg I λ 1.183 μm may be used to identify later spectral type objects like red supergiants, while He I λ 1.197 μm is present in early-type stars. These lines allow for a radial velocity measurement using the templates from Gazak et al. (2014), ensuring the objects are extragalactic and are part of M83. The spectral data were reduced and extracted using the standard KMOS pipeline. According to the radial velocity and spectral features analysis of obtained spectra 10 of 18 targets appear to be RSGs. The analysis of these spectra is still in progress, and a publication is in preparation. An example of a KMOS spectrum of one candidate RSG in M83 in J-band is presented in Figure 5.4. Up to this date, these newly identified RSGs in M83, are the most distant RSGs known.

5.6 Determination of the fundamental parameters of RSGs

In order to derive the fundamental parameters, such as effective temperature (T_{eff}), surface gravity ($log\ g$), microturbulent velocity (v_{mic}) of newly discovered RSGs we fitted the optical region (5000 – 8000 Å) of their spectral energy distribution (SED) with MARCS stellar atmosphere models (Gustafsson et al. 2008), which are one-dimensional (1D) spherical hydrostatic models. This region of the spectrum is dominated by TiO absorption bands, which classically serve as an important spectral type indicator. To make the proper fitting we degrade the resolution of MARCS grid from R = 500 000 to 500, which is an average of the flux calibrated spectra of our RSG sample. We fixed the following parameters: $log\ g$ = 0, v_{mic} = 5 $km\ s^{-1}$, $[Fe/H]$ = -1 dex, as the most appropriate

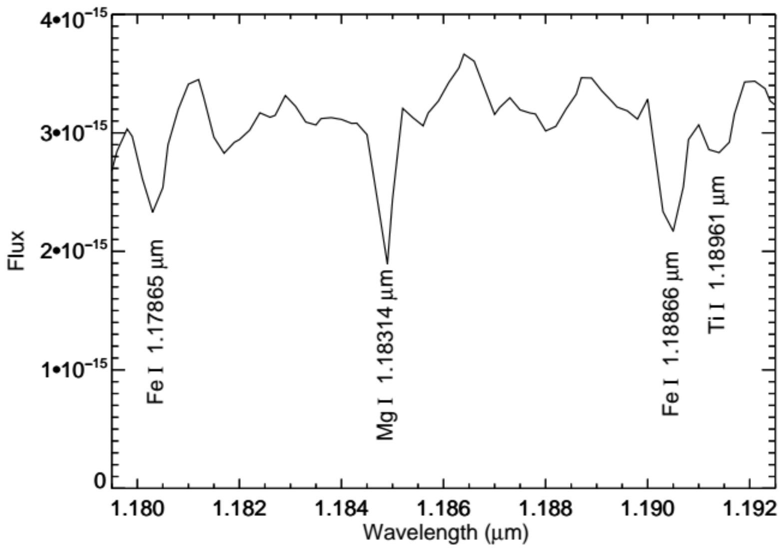

Figure 5.4: The spectrum one of the observed RSG in M83 in J-band, with prominent spectral features indicated.

for RSGs in dIrr galaxies and we varied only the effective temperature and extinction (A_V) in order to get the best match of the modeled and observed SED of RSGs.

The first step of the analysis was devoted to getting some estimates of the radius (R) and reddening $E(B-V)$ for each RSG. This step is presented in the Appendix with the Matlab routine in "Script 1". In this step, we followed this procedure: for each value of radius that varies in the range of 300 to 1300 $R_\odot$ with a step 100 $R_\odot$ (in some cases we increased the upper limit of the radius up to 2300 $R_\odot$), we found the best fit between observed and modeled SEDs by varying T_{eff} (from 3400 K to 4380 K with a step 20) and R_V (from 1 to 6, with a step 0.2). At this step we varied the total to selective absorbtion extinction R_V, which is defined as $R_V = A_V/E(B-V)$. (For calculation of the extinction across all spectral wavelength range we used extinction law from Cardelli et al. (1989). Both versions of routines for optical and mid-IR wavelength range are presented in the Appendix.) This provided an additional check of the fitting result, because R_V is adopted as a constant for each galaxy, for example for the LMC and SMC, R_V is equal to 2.7 and

3.4 respectively (Gordon et al. 2003). However, in the case of RSGs, this value cannot be constant, due to the high and unpredictable mass loss rate; nevertheless we expect for R_V to lie in a reasonable range (from 2 to 4) at the value of radius that corresponds to a best fit of observed and modeled spectral energy distribution of RSGs. Moreover, inside this procedure we varied the value of reddening $E(B-V)$ from 0.1 to 0.3 mag in order to find the best match for each solution of T_{eff} and R_V at given stellar radius.

For each value of radius we found the best fitting SED and the residual minimum of χ_2. The absolute minimum of χ^2 gives us the appropriate value of radius. At this final value of radius, R_V should be realistic (i.e. R_V between $2-4$). If the derived values of R_V are not in this range, it means that we need to change the initial assumptions about stellar radius or $E(B-V)$. If the final value of R_V is within this range, the algorithm returns the final values of R, and $E(B-V)$, which are used in the next step. Also it returns a first estimate of T_{eff} and extinction A_V.

In the next step, (see "Script 2" in Appendix) we also applied the χ^2 minimization that returns the final values of T_{eff} and A_V which correspond to the best fit of the observed and modeled SEDs by varying T_{eff} (from 3400 to 4380, with a step of 20 K) and A_V (0.1 to 6, with a step 0.1). At this step we fixed the radius and $E(B-V)$ that we found in the previous step. Moreover, we used Monte Carlo simulations, which vary the radius with uncertainties $\pm$ 50 $R\odot$ and $E(B-V)$ with in uncertainties $\pm$ 0.1, as they were found in our previous step.

The χ^2 minimization and the resulting best-fit SEDs for 16 program RSGs are presented in Figures 5.5 – 5.18. In each Figure on the top panel presents the SEDs χ^2 minimization in 3D visualization, while on the bottom panel the final fit of observed and modeled SEDs. The preliminary derived values of T_{eff}, A_V, R_V and R for 16 RSGs that were analyzed so far are presented in Table 5.2. The names of RSGs in each plot are consistent with Table 5.2.

The determined values of T_{eff} and A_V were used to place our program RSG from

different dIrr galaxies on the H-R diagram. To do so, we calculated the luminosities of RSGs by using their T_{eff}, A_V, V-band magnitude, and the distance (d) of the host galaxy. For that we also computed the bolometric correction (BCv) by using the empirical equation from Levesque et al. (2006) that converts T_{eff} to BCv at SMC metallicity:
$BCv = -120.102 + 82.3070 \times \left(\frac{T_{eff}}{1000}\right) - 19.0865 \times \left(\frac{T_{eff}}{1000}\right)^2 + 1.48927 \times \left(\frac{T_{eff}}{1000}\right)^3$.

We used this equation for the SMC because it is the lowest metallically ([Fe/H] = -1 dex), for which this equation is valid and exist so far. However, this assumption is not accurate because the metallicities of program dIrr galaxies are lower, for example the metallicity of Sextans A galaxy is [Fe/H] = -1.85 dex. Moreover, there is another problem in our analysis, at a given temperature the MARCS stellar atmosphere models do not predict the proper strength of TiO bands which dominate in the optical region in the spectra of RSGs (Davies et al. 2013). Thus, the derived physical parameters of RSGs, from the optical wavelength range fitting of SEDs, can only be used as preliminary values.

In Figure 5.19 we present the evolutionary tracks from Ekström et al. (2012) and Brott et al. (2011) at the same metallicity, together with preliminary derived physical parameters of RSGs from different dIrr galaxies. Also, as a reference, we plotted the RSGs in the LMC and the SMC for which the fundamental parameters have been derived by Davies et al. (2013). It can be seen, that almost all RSGs in dIrr galaxies have higher temperatures than RSGs in the MCs. This occurs mainly due to the lower metallicities of RSGs in dIrrs than in the MCs - as a result the TiO bands are weaker, and the best-fit MARCS models show higher temperatures. In the future it is necessary to improve the bolometric correction relation at lower metallicities and, also obtain the near mid-IR spectra to include this wavelength region of the RSG spectra during the fitting with the MARCS models, because it appears more reliable for the derivation of physical parameters compared to the optical region (Davies et al. 2013). Some interesting objects can be already found on this HR diagram, for instance, three RSGs in Sextans A with extremely high luminosities. The preliminary result shows that they are extremely massive, with radii <

1500 $R_\odot$, however this statement requires further confirmation. Another object that should be point out, the RSG in Phoenix dIrr galaxy, according to the MARCS model fitting we obtained relatively low luminosity. That can be a hint about not RSG nature of this star, more probable this is AGB or super-AGB star.

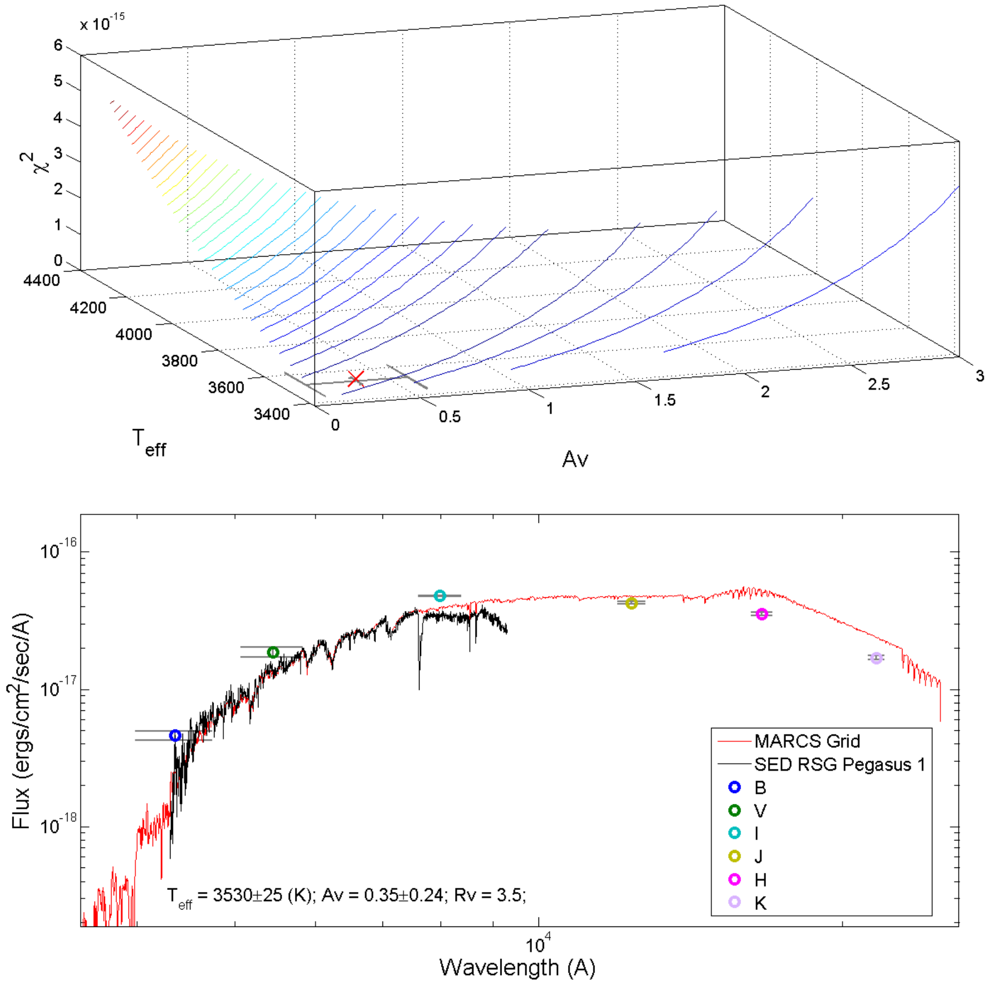

Figure 5.5: Top panel: Result of the χ^2 minimization of the MARCS model SED fitting by varying the values of T_{eff} and A$_V$ for Pegasus 1 RSG. The "x" symbol corresponds to the best fit parameters, with included error bars. Bottom panel: Best fit of MARCS model spectral energy distribution to the spectrum of Pegasus 1 RSG and available optical and near-IR photometry. The best fit parameters are indicated on the figure.

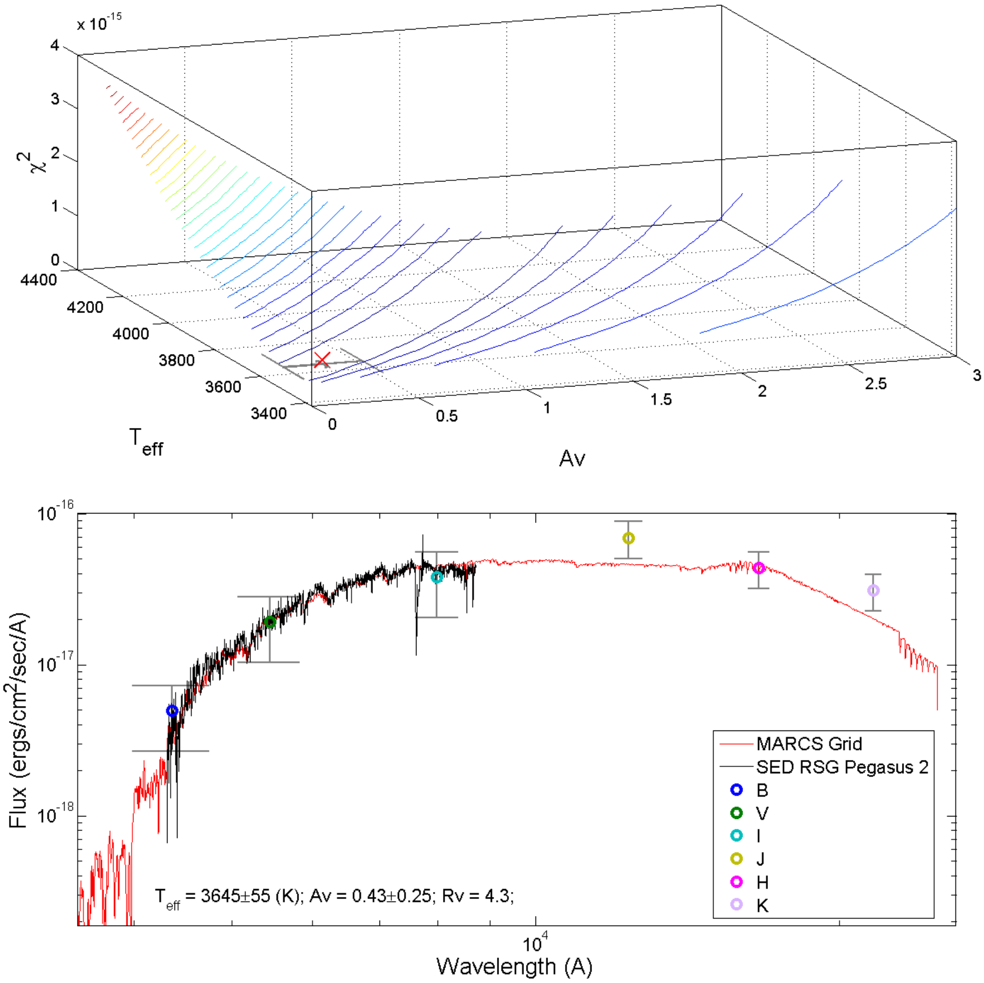

Figure 5.6: Same as Figure 5.5, but for Pegasus 2 RSG.

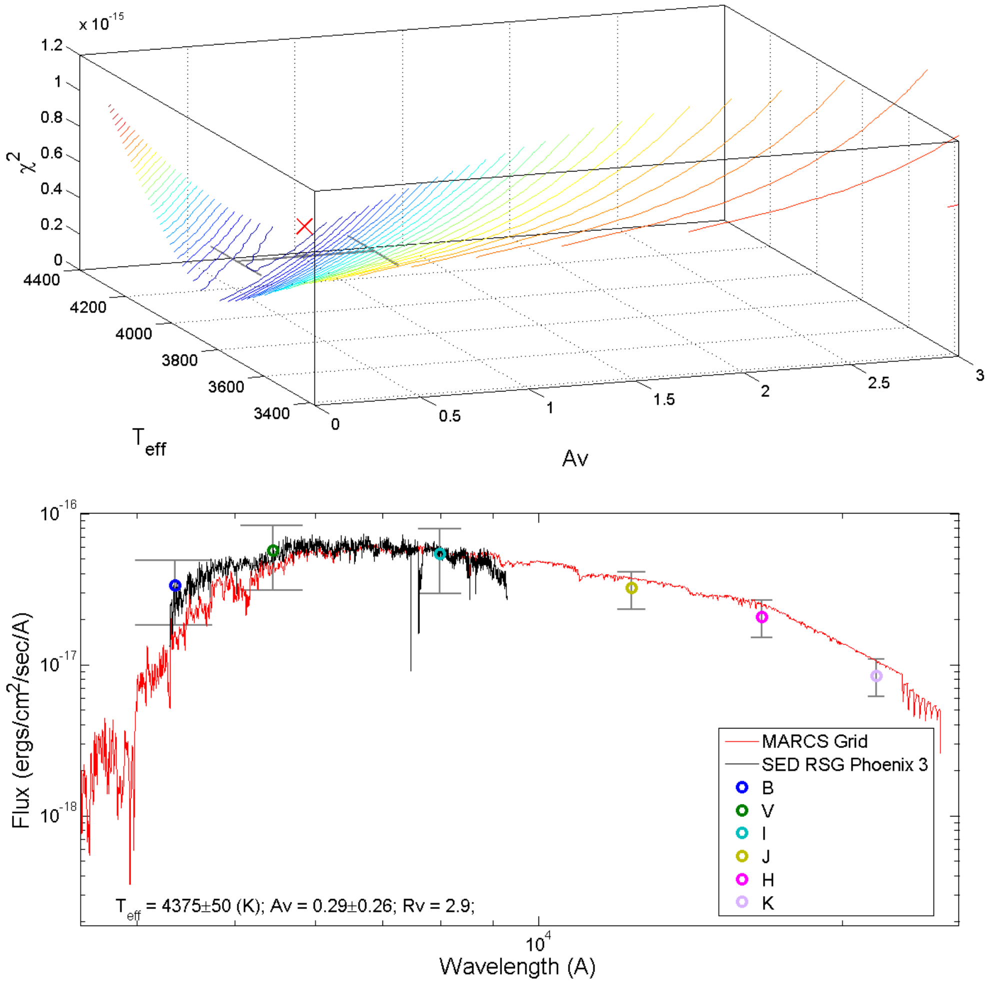

Figure 5.7: Same as Figure 5.5, but for Phoenix 3 RSG.

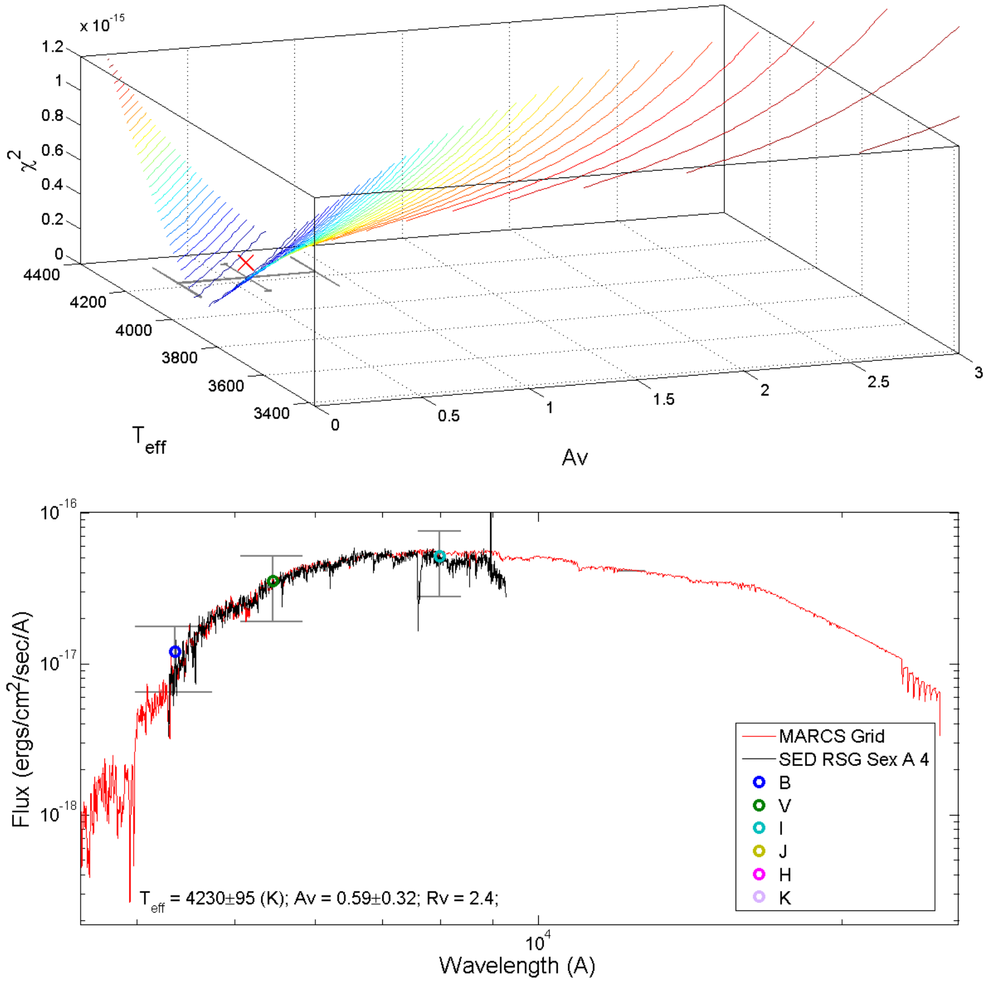

Figure 5.8: Same as Figure 5.5, but for Sextans A 4 RSG.

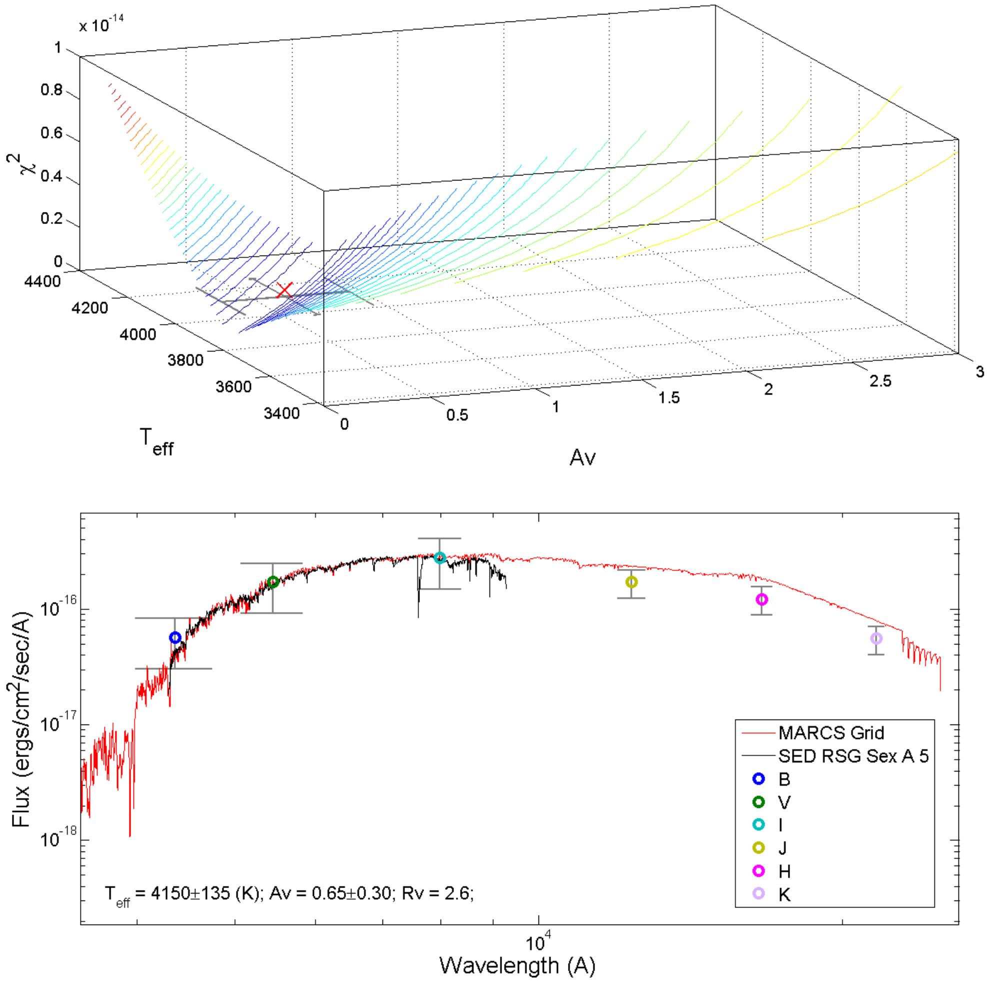

Figure 5.9: Same as Figure 5.5, but for Sextans A 5 RSG.

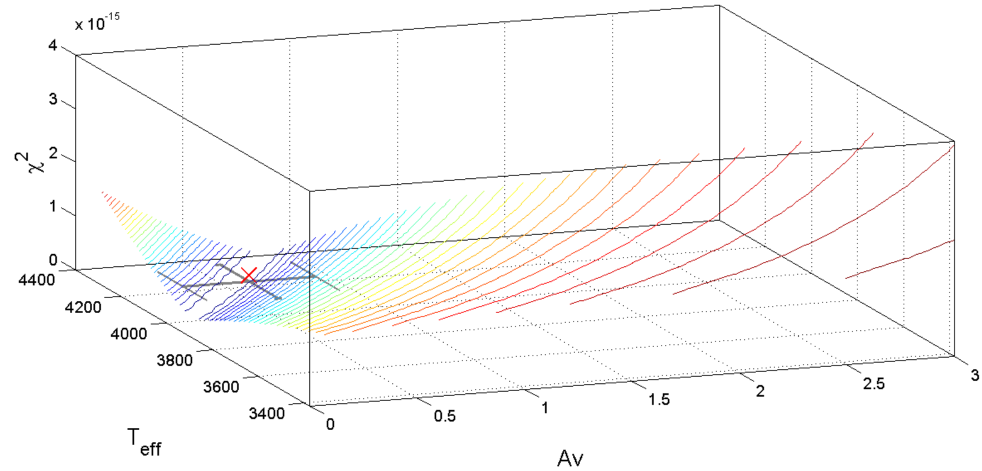

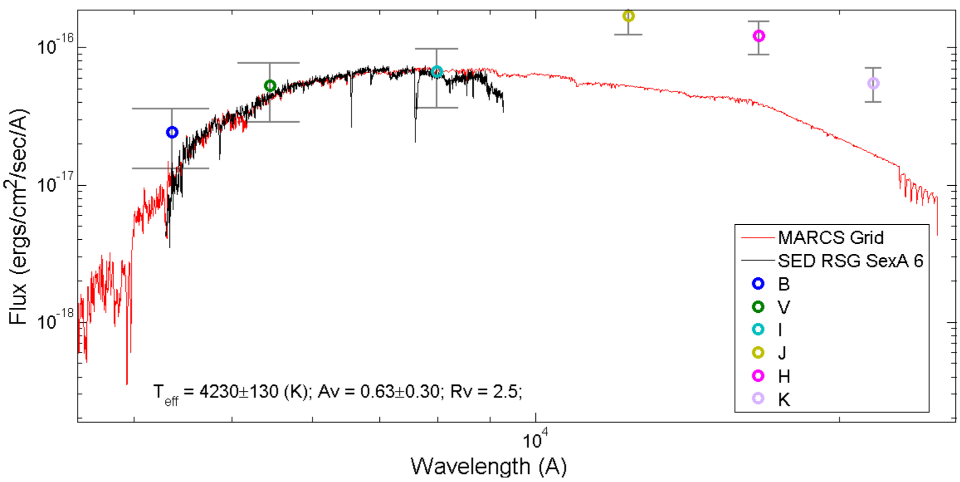

Figure 5.10: Same as Figure 5.5, but for Sextans A 6 RSG.

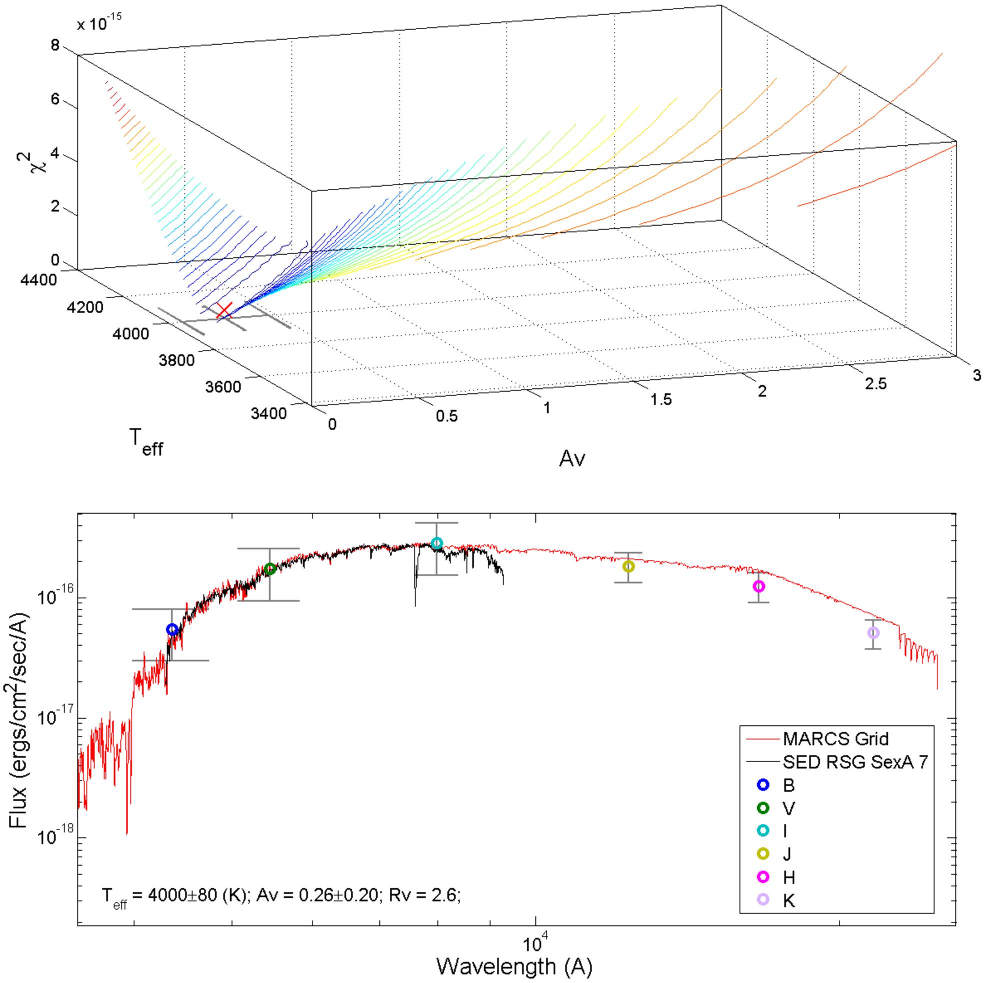

Figure 5.11: Same as Figure 5.5, but for Sextans A 7 RSG.

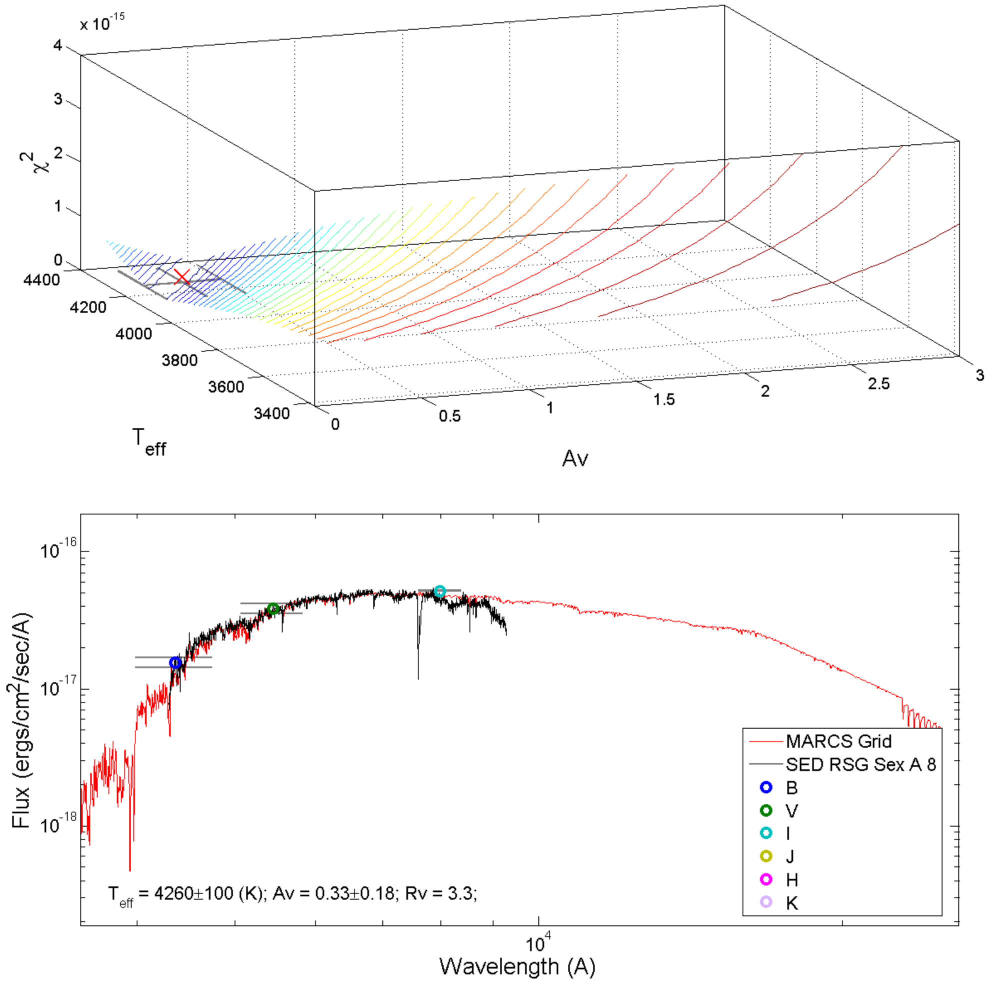

Figure 5.12: Same as Figure 5.5, but for Sextans A 8 RSG.

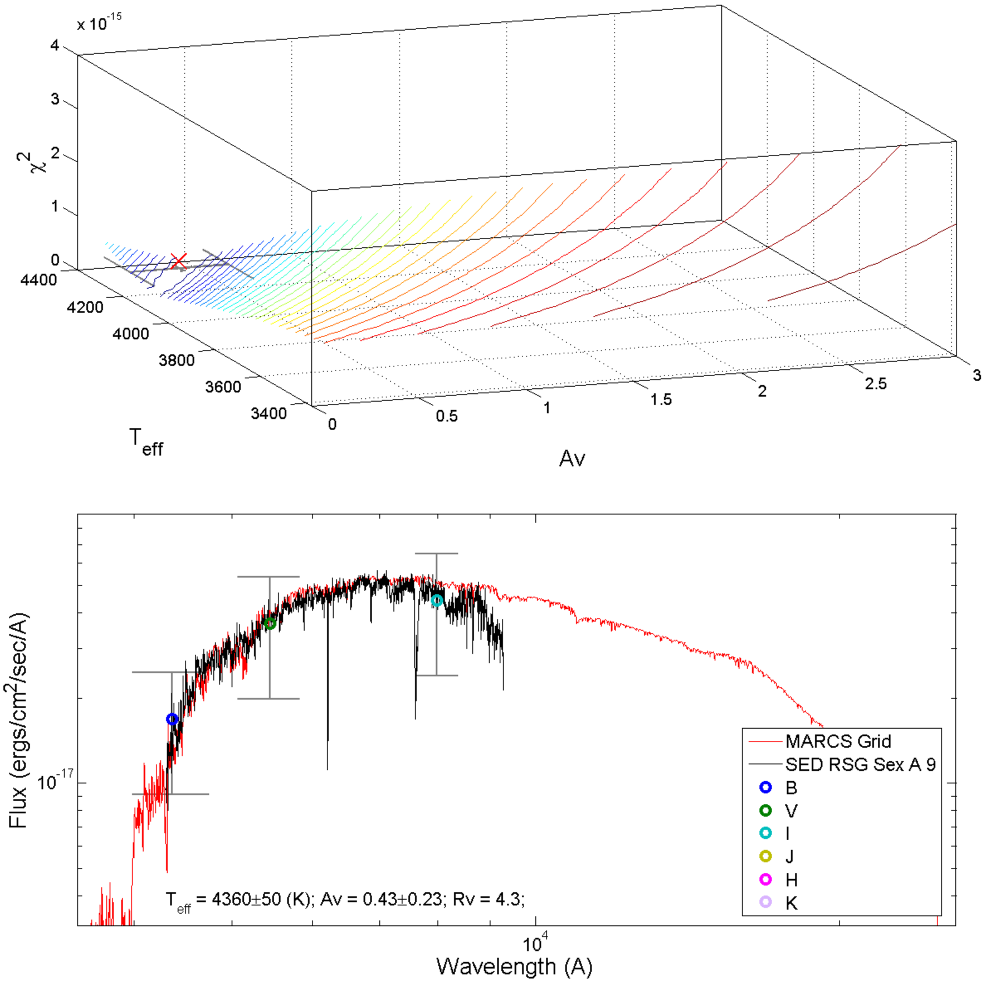

Figure 5.13: Same as Figure 5.5, but for Sextans A 9 RSG.

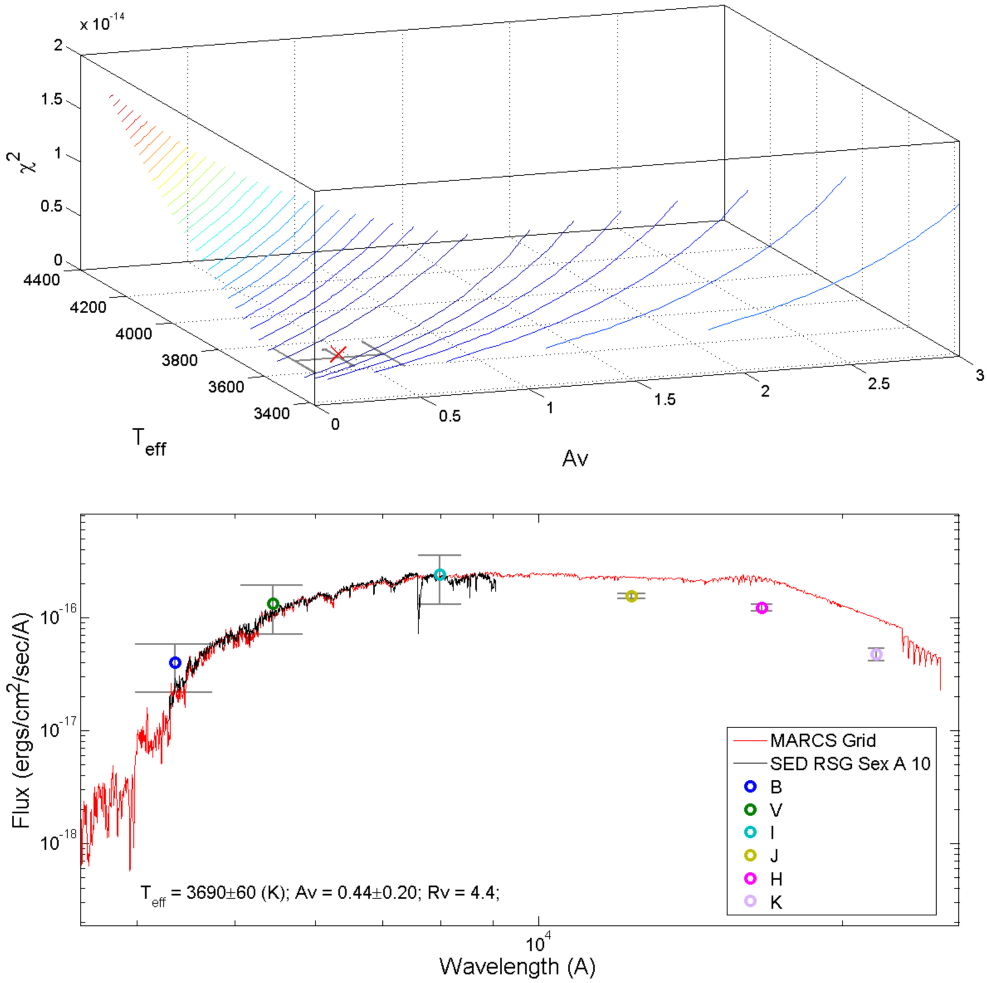

Figure 5.14: Same as Figure 5.5, but for Sextans A 10 RSG.

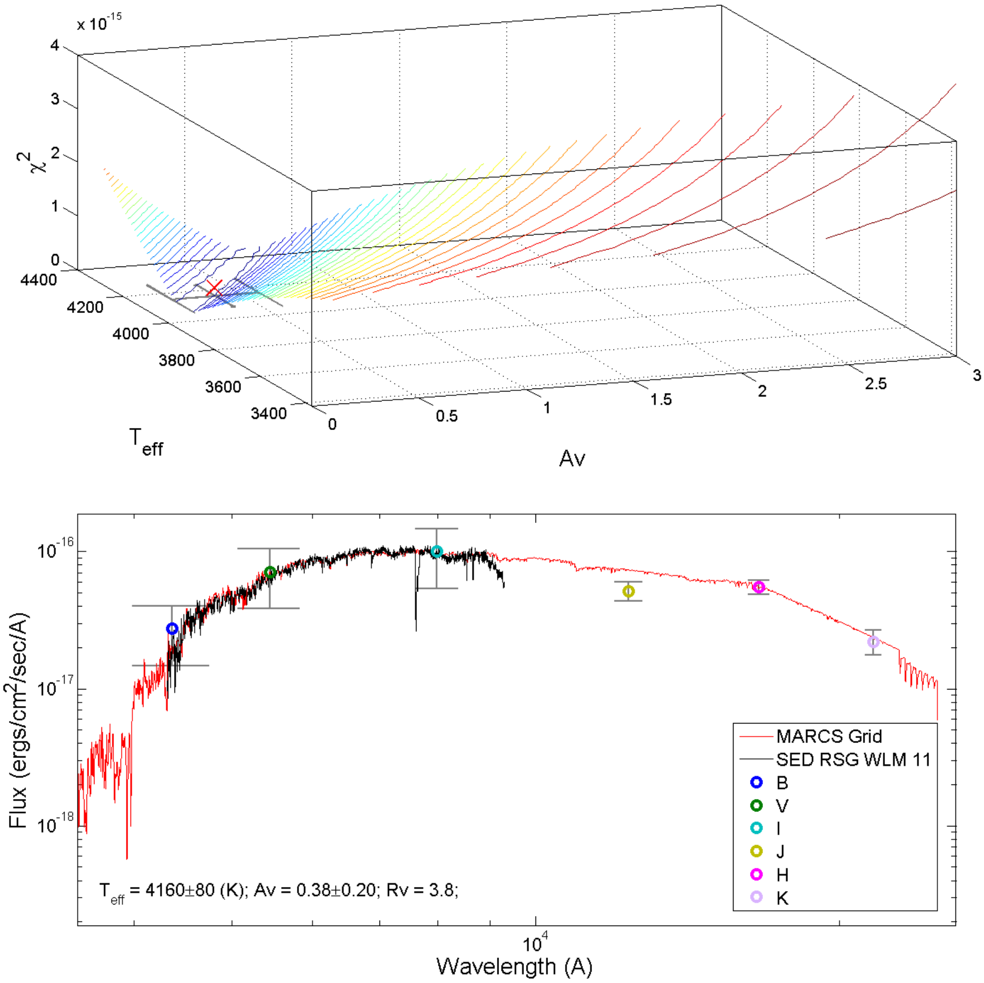

Figure 5.15: Same as Figure 5.5, but for WLM 11 RSG.

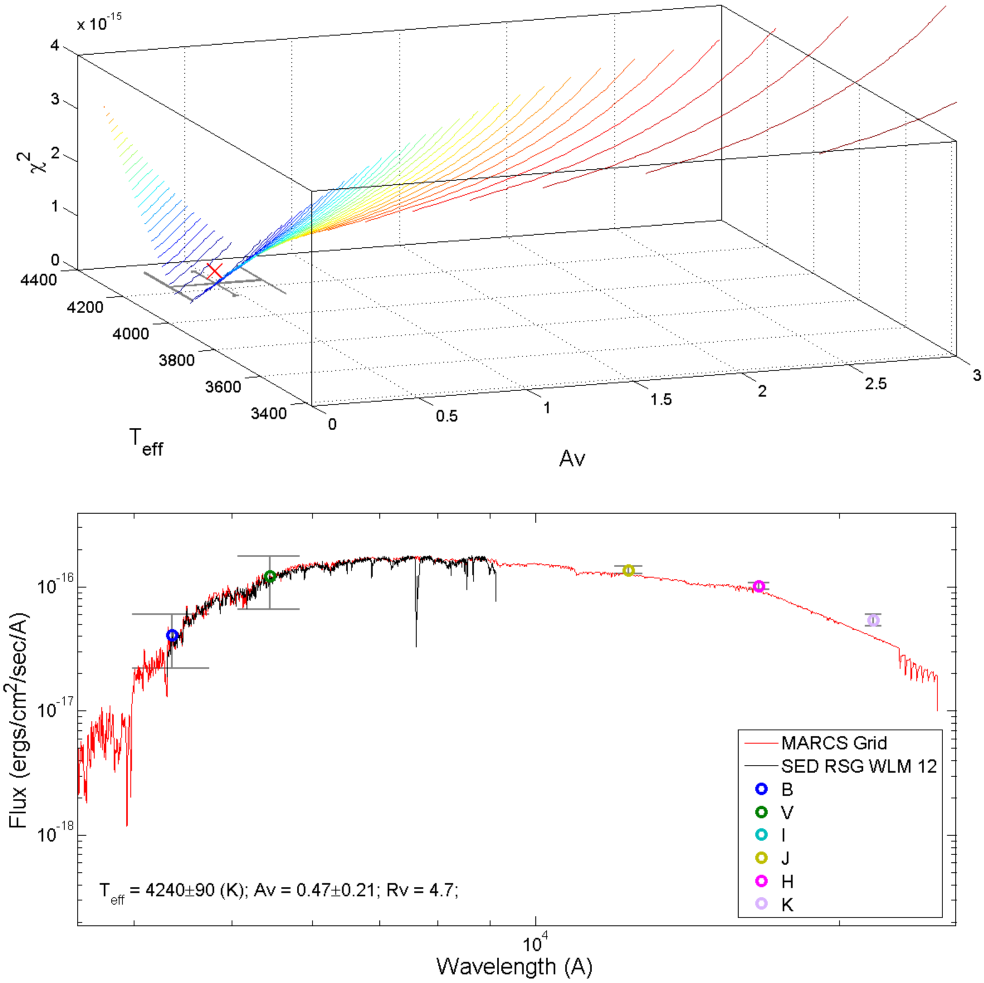

Figure 5.16: Same as Figure 5.5, but for WLM 12 RSG.

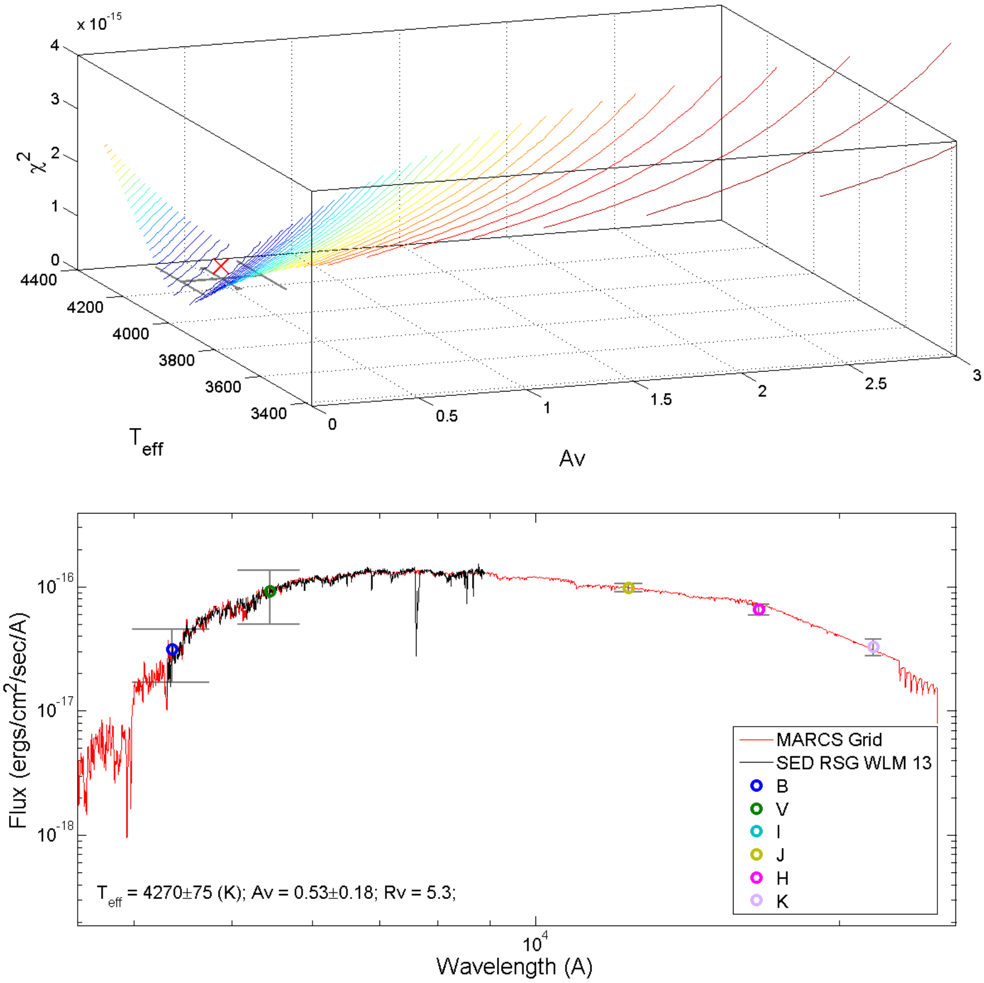

Figure 5.17: Same as Figure 5.5, but for WLM 13 RSG.

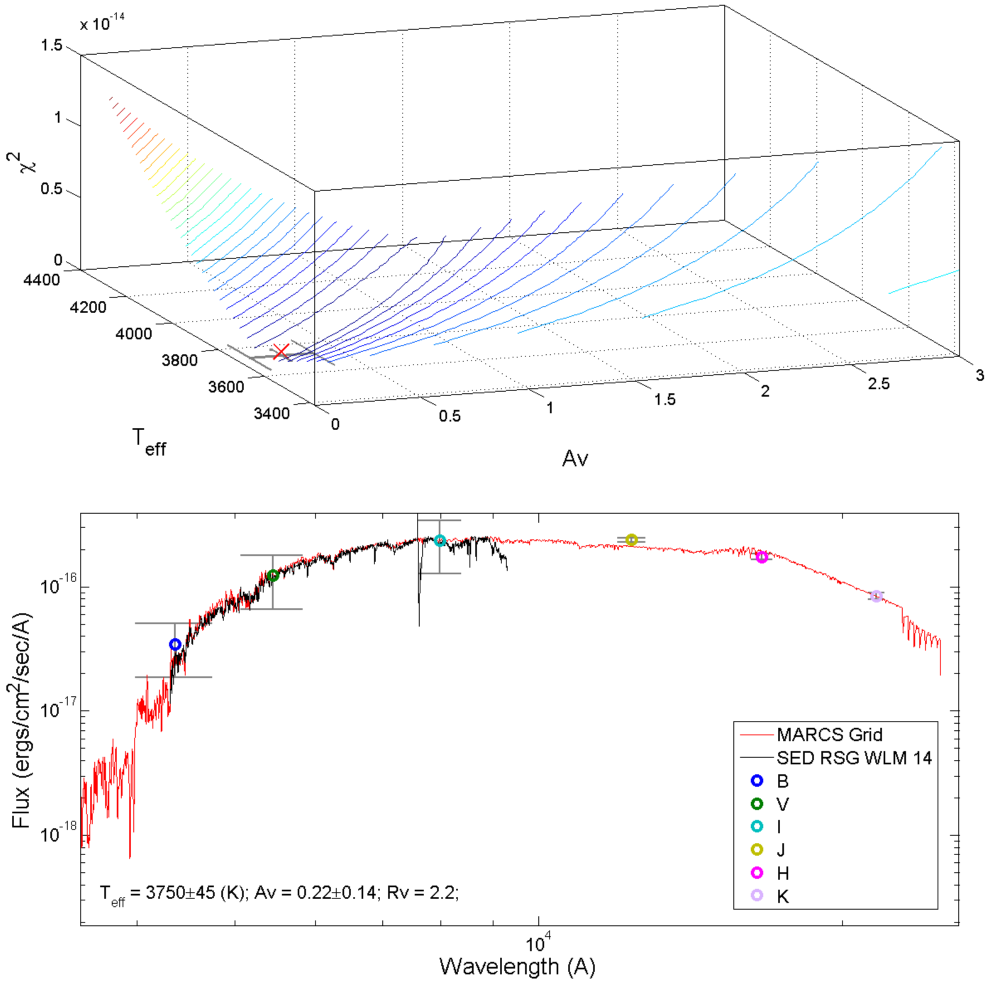

Figure 5.18: Same as Figure 5.5, but for WLM 14 RSG.

Table 5.2: *Preliminary* fundamental parameters for all identified RSGs in dIrr galaxies.

RSG Name	DUSTiNGS ID	R.A. (deg)	Decl. (deg)	T_{eff}(TiO) (K)	A_V(TiO)	R(TiO) ($R_\odot$)	R_V(TiO)	Sp. Class Britavskiy et al. (2014, 2015)
Pegasus 1	116706	352.14938	14.73709	3530±25	0.35±0.24	800	3.5	M0-2 I
Pegasus 2	136294	352.12616	14.74971	3645±55	0.43±0.25	700	4.3	K4-5 I
Phoenix 3	119803	27.79501	−44.41927	4374± limit	0.29±0.26	200	2.9	K1-2 I (AGB ?)
Sex A 4	77330	152.76654	−4.70795	4230±95	0.59±0.32	800	2.4	K1-3 I
Sex A 5	72683	152.77316	−4.69916	4150±135	0.65±0.30	2000 (?)	2.6	K1-3 I
Sex A 6	70373	152.77670	−4.70510	4230±120	0.63±0.30	900	2.5	YSG ??
Sex A 7	106505	152.72426	−4.68539	4000±80	0.26±0.20	1900 (?)	2.6	K1-3 I
Sex A 8	102187	152.73050	−4.71217	4260±100	0.33±0.18	700	3.3	K1-3 I
Sex A 9	98470	152.73587	−4.70284	4360±50	0.43±0.23	700	4.3	K1-3 I
Sex A 10	98112	152.73636	−4.67753	3690±60	0.44±0.20	2400 (?)	4.4	K3-5 I
WLM 11	101523	0.48976	−15.48786	4158±80	0.38±0.20	700	3.8	K1-3 I
WLM 12	90598	0.50340	−15.52166	4240±90	0.47±0.21	900	4.7	K1-3 I
WLM 13	94581	0.49837	−15.51678	4270±75	0.53±0.18	800	5.3	K1-3 I
WLM 14	83414	0.51268	−15.50950	3750±45	0.22±0.14	1400 (?)	2.2	K4-5 I
IC 10 1	103677	5.0575594	59.2875137	–	–	–	–	K3-5 I
IC 10 2	117107	5.0198626	59.2903671	–	–	–	–	M0-2 I
IC 10 3	95408	5.0804367	59.3092765	–	–	–	–	M1-3 I
IC 10 4	99773	5.0684976	59.2951965	–	–	–	–	M0-2 I
IC 10 5	85592	5.1077690	59.3035316	–	–	–	–	M1-3 I
IC 10 6	107961	5.0455651	59.2827033	–	–	–	–	K3-5 I
IC 1613 1	161666	16.158911	2.112404	4366±16 (?)	0.42±0.22	550	4.2	M0-2 I
IC 1613 2	119457	16.210361	2.106991	4358±20 (?)	0.42±0.13	600	4.2	M2-4 I
IC 1613 3	97761	16.237533	2.078947	–	–	–	–	K1-3 I
Sex B 1	100179	149.994064	5.326573	–	–	–	–	K1-3 I
Sex B 2	82970	150.017166	5.309929	–	–	–	–	K1-3 I

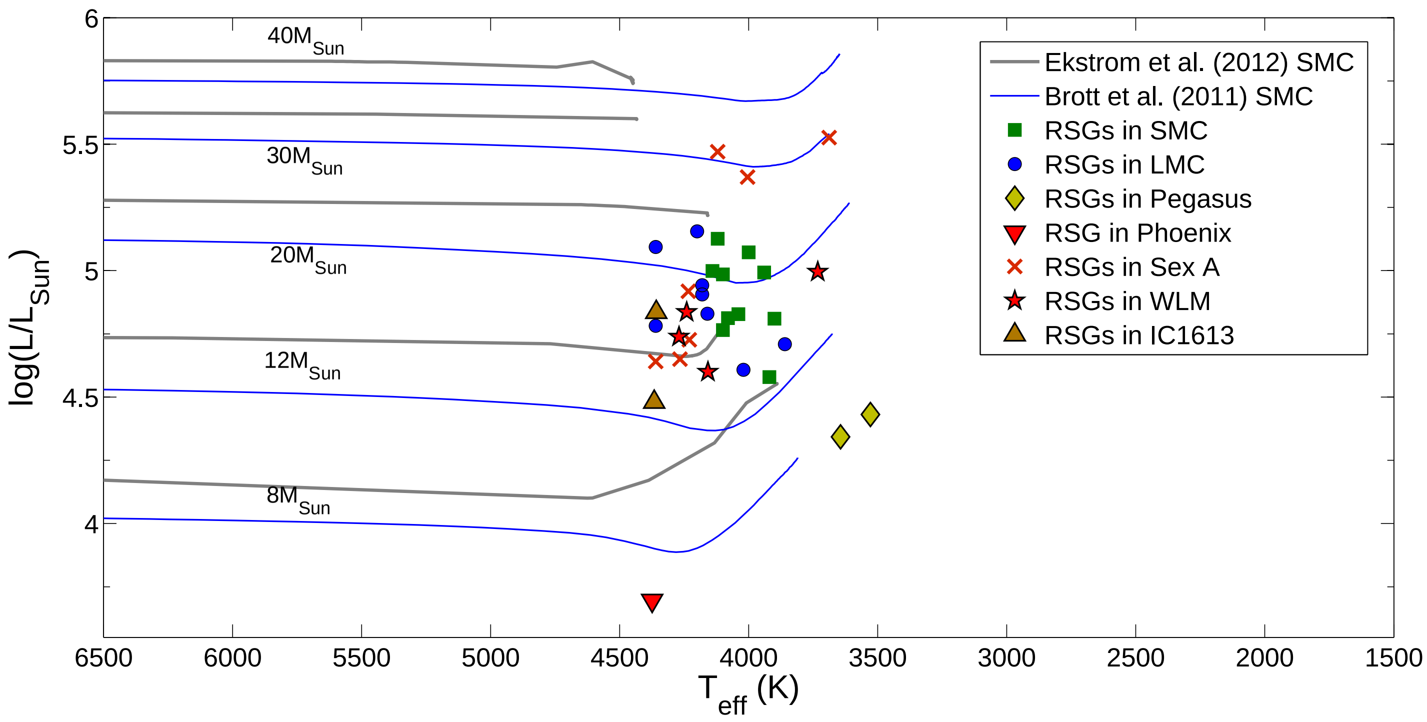

Figure 5.19: The "RSG region" of the Hertzsprung-Russell diagram, with evolutionary tracks from Ekström et al. (2012) and Brott et al. (2011) for the SMC metallicity. The sample of investigated RSGs from the SMC and LMC (Davies et al. 2013) is plotted together with the dIrr RSGs from Britavskiy et al. (2014, 2015) with preliminary derived fundamental parameters.

Chapter 6

Conclusions

In this PhD Thesis we initiated the census of dusty massive stars in the Local Group with existing episodic mass loss phenomena, namely in RSG, sgB[e], LBV stars. We increased statistics of such spectroscopically confirmed objects in star forming dwarf irregular galaxies that will shed the light on the role of episodic mass loss in massive star evolution, which is one of the most important open questions of current stellar evolution theory. Moreover, discoveries of dusty massive stars in the Local Group will help to constrain the massive star evolution theory on context of different metallicities of host galaxies.

For selecting dusty massive stars we used 3.6 μm and 4.5 μm photometry from archival *Spitzer* Space Telescope images of nearby galaxies. We applied mid-IR selection criteria to 7 dIrr galaxies: Sextans A, Sextans B, Phoenix, Pegasus, IC 10, IC 1613 and WLM. We observed and classified 124 luminous in mid-IR sources, and the main results of this PhD Thesis are:

i) We identified 28 RSGs, 21 of them are new discoveries, that increases the sample of known RSGs in dIrr galaxies in the Local group by 47%. Newly identified RSGs are 3 in IC 1613, 7 RSGs in Sextans A, 2 RSGs in Sextans B, 1 RSG in Phoenix, 2 RSGs in Pegasus, and 6 RSGs in IC 10. For these dIrr galaxies this sample of RSGs is the first spectroscopic identifications of RSGs. Also, we independently identified 7 RSGs in WLM, which have been previously identified in Levesque & Massey (2012). The spectral type comparison of previously observed and our observations of RSGs in WLM shows no spectral type variability for this sample of RSGs. Majority of identified RSGs have early K spectral type, which is predicted for such low metallicity galaxies.

ii) We identified 2 new rare emission line stars (iron stars) in WLM dIrr galaxy, also, 8 carbon stars (AGB), background galaxy and a quasar, as contaminants. These two iron stars are the first identification of such objects in dIrr galaxies in the Local Group.

iii) We revised optical and mid-IR selection criteria for selecting dusty massive stars (RSGs, LBVs, sgB[e]); We computed and compared the efficiency of mid-IR and optical selection criteria for RSGs. The mid-IR selection criteria have lower efficiency in separating foreground giants from extragalactic RSGs than optical selection criteria. However, comparing success rate in the optical selection criteria ($\approx$ 70 %) with a number of RSGs that satisfy the mid-IR selection criteria ($\approx$ 90 %), we can conclude that the mid-IR selection criteria are useful for selecting dusty massive stars, however these criteria are not so efficient in separating them from foreground contaminants. Moreover, with available *Spitzer* mid-IR photometry (Boyer et al. 2015b) for 13 dwarf irregular galaxies in the Local Group, our tool provides an opportunity to select candidate dusty massive stars in star-forming dIrrs in cases where accurate optical photometry does not exist or is not deep enough.

iv) So far we derived fundamental physical parameters (R, T_{eff}, A_V, etc) for 16 RSGs; in principle this RSG survey will become more important with the next generation telescopes - TMT, E-ELT (Evans et al. 2012) and JWST. These telescopes and their instruments will be optimized for observations at infrared wavelengths (where the

RSGs are the most luminous stellar sources in galaxies), thus, the survey of known RSGs will help develop tools for understanding of the physics of these objects which will be observed out of 100 Mpc, and their host galaxies.

6.1 Future Work

The underlying physics of RSGs remains poorly understood. RSGs belong to the short but critical stage of massive star evolution, thus due to the low number of well-studied objects, there are discrepancies in stellar evolutionary model predictions of the parameters of RSGs compared to the observed properties of RSGs (such as temperature, gravity, etc.). In addition, the physical characteristics of RSGs vary at different metallicities (Elias et al. 1985; Levesque et al. 2006; Levesque & Massey 2012), but the number of known RSGs beyond the Milky Way, and as a result in more metal poor host galaxies, is low. The exception is the number of known RSGs in the distant and massive M31, M33 galaxies and MCs. In the last 10 years nearly 200 RSGs were discovered and spectroscopically confirmed in the Small Magellanic Cloud (SMC, 105 - Massey et al. 2002, 83 - from Gonzalez-Fernandez et al. 2015), 250 RSGs in the Large Magellanic Cloud (LMC, 158 - Massey et al. 2002, 96 - Gonzalez-Fernandez et al. 2015). The situation is different in more distant dwarf irregular (dIrr) galaxies - in total 58 RSGs are known in 8 dIrrs in the Local Group. There are 11 RSGs spectroscopically confirmed in WLM (Levesque & Massey 2012), 26 in NGC 6822 (Levesque & Massey 2012; Patrick et al. 2015), 2 in Pegasus, 1 in Phoenix, 7 in Sextans A, 2 in Sextans B, 6 in IC 10 and 3 in IC1613 (Britavskiy et al. 2014, 2015, in prep.). This sample of dIrr galaxies together with the MCs provides an ideal laboratory for investigating the physical properties of RSGs over a wide range of host galaxy metallicities from [Fe/H] = -0.5 dex (LMC) to [Fe/H] = -1.85 dex (Sextans A). By taking into account the previously listed problems, we propose a continuation of our work that will grow in two main directions: 1) derive the physical parameters and mass loss rates of RSGs, 2) perform a chemical abundance analysis of RSGs. For measuring the mass loss rate it is necessary to spectroscopically observe a broad wavelength range including the near-IR. This will allow us to make a fit of the RSGs spectral energy distribution (SED) in conjunction with the fluxes at near-IR bands (e.g. J, H, and K photometric bands) from the dust radiative transfer model DUSTY (Ivezic et al. 1999). Along with a stellar atmosphere model of the star, the infrared excess, which occurs due to dust (Lobel et al. 2000, van Loon et al. 2005) may be related to the mass loss rate. By combining the SED of RSGs with their IR photometry from 2MASS, Spitzer images (Boyer et al. 2015), and WISE (Cutri et al. 2012) it will be possible to get accurate measurements of the mass loss rates in RSGs. The most suitable instruments for doing this analysis are the near-IR spectrographs e.g. FIRE on Magellan telescopes, or XSHOOTER and KMOS spectrographs on VLT. Moreover, the spectra from moderate resolution spectrographs (e.g $R \approx 5000$ for XSHOOTER) will be very useful for determining accurate physical parameters of RSGs from fitting the spectra with MARCS stellar atmosphere models (as shown in Davies et al. 2013). Armed with accurate stellar atmosphere parameters of RSGs, we can proceed to perform chemical abundance analysis of our confirmed RSGs. Recent studies have shown a chemical abundances of RSGs are best derived from moderate resolution spectra (R about 3000) in the near infrared J band (Davies et al. 2010, Gazak et al. 2014). So far, chemical abundances analyses of RSGs in the Local Group using KMOS spectrograph have been performed for 60 RSGs, namely, 9 RSGs in the LMC, 10 in the SMC (Davies et al. 2015), 11 in NGC 6822 (Patrick et al. 2015) and for 30 RSGs beyond the Local Group: 27 in NGC 300 (Gazak et al. 2015) 3 in NGC 4038 (Lardo et al. 2015). As a main goal of future work we are planning to perform detailed spectroscopic investigations of 47+ spectroscopically confirmed RSGs in 7 dIrr galaxies (Pegasus, Phoenix, Sextans A, Sextans B, WLM, IC 10, IC 1613) by using near-IR band spectrographs, with a final goal to derive the abundances and fundamental parameters of RSGs at low metallicity. This will increase the sample of well-studied RSGs in the Local Group by more than a factor of two, which will make a strong basis for constraining evolutionary models.

Chapter 7

Appendix

7.1 Publications

1. **Identification of dusty massive stars in star-forming dwarf irregular galaxies in the Local Group with mid-IR photometry.** N.E. Britavskiy, A.Z. Bonanos, A. Mehner, M.L. Boyer, K.B.W. McQuinn, Astronomy & Astrophysics, 2015, 584, A33

2. **Chemical abundances of solar neighbourhood RR Lyrae stars.** E. Pancino, N.E. Britavskiy, D. Romano, C. Cacciari, A. Mucciarelli, G. Clementini, MNRAS, 2015, 447, 2404

3. **Identification of red supergiants in nearby galaxies with mid-IR photometry.** N.E. Britavskiy, A.Z. Bonanos, A. Mehner, D. García-Álvarez, J. L. Prieto, N. I. Morrel, Astronomy & Astrophysics, 2014, 562, A75

7.1.1 Conference Proceedings

1. **Luminous Infrared Sources in the Local Group: Identifying the Missing Links in Massive Star Evolution.**, N.E. Britavskiy, A.Z. Bonanos, A. Mehner, IAU Sym-

posium, 307, 92

2. **A New Technique for Identifying Massive Stars in the Local Group.** N.E. Britavskiy, 11th Conference of Hellenic Astronomical Society, 41

7.2 Allocations of Telescope Time

1. Aristarchos 2.3m, Helmos Observatory, Greece:

   (a) "Probing for spectroscopic variability in dusty, luminous objects in M31 and M33", M. Kourniotis, A. Bonanos, N. Britavskiy, S. Williams, P. Boumis, 2 nights in 2015

   (b) "Luminous Infrared Sources in the Local Group: Identifying the Missing Links in Massive Star Evolution", 2 nights in 2014

2. VLT/FORS2, Paranal Observatory, Chile:

   (a) "Luminous Infrared Sources in Nearby (Dwarf) Irregular Galaxies: Identifying the Missing Links in Massive Star Evolution", A. Mehner & A. Bonanos, 11 hrs (090.D-0009)

   (b) "Luminous Infrared Sources in Nearby (Dwarf) Irregular Galaxies: Identifying the Missing Links in Massive Star Evolution", A. Mehner & A. Bonanos, 3.4 hrs (091.D-0010)

   (c) "Luminous Infrared Sources in WLM: Completing the Census of Dusty Massive Stars", N. Britavskiy, A. Bonanos, A. Mehner, 2.7 hrs (095.D-0313)

3. VLT/KMOS, Paranal Observatory, Chile: "The Massive Stellar Content of M83", S. Williams, A. Bonanos, N. Britavskiy, 3 hrs (095.D-0189)

4. Subaru, Mauna Kea Observatories, Hawaii, USA: "Near-infrared spectroscopy of dusty, massive stars in the M33 and WLM galaxies", Chien-Hsiu Lee, A. Bonanos, M. Kourniotis, N. Britavskiy, 1 night (October 4, 2015)

5. OSIRIS/GTC, Roque de los Muchachos Observatory, La Palma, Canary Islands, Spain: "Luminous Infrared Sources in the Local Group: Identifying the Missing Links in Massive Star Evolution", D. Garcia Alvarez, N. Britavskiy, M. Kourniotis, A. Bonanos, A. Mehner, S. Williams, P. Boumis, 10.6 hrs (Semester 2014B)

7.3 Conferences and Schools

- “High-precision studies of RR Lyrae stars", 19 – 22 October, 2015, Visegrad, Hungary (**Talk**)

- IAU XXIX General Assembly, Focus Meeting 17, 12 – 14 August, 2015, Honolulu, Hawaii, US (Poster)

- IAU XXIX General Assembly, Focus Meeting 16, 3 – 5 August, 2015, Honolulu, Hawaii, US (**Talk**)

- 12th Conference of the Hellenic Astronomical Society, 28 June – 2 July 2015, Thessaloniki, Greece (**Talk**)

- IAU 307, “New Windows on Massive Stars", 23 – 27 June 2014, Geneva, Switzerland (Poster)
  Proceedings: “Luminous Infrared Sources in the Local Group: Identifying the Missing Links in Massive Star Evolution", IAU Symposium, 307, 92

- 10th Summer School in Statistics for Astronomers, 2 – 6 June 2014, Penn State, US (Participant)

- 11th Conference of Hellenic Astronomical Society, 8 – 12 September 2013, Athens, Greece (**Talk**)

  Proceedings: “A New Technique for Identifying Massive Stars in the Local Group", 41

- GREAT Astrostatistics School, 17 – 21 June 2013, Alicante, Spain (Participant)

- “Massive Stars: From α to Ω" conference, 10 – 14 June 2013, Rhodes, Greece (**Talk, LOC member**)

- International school of Astrophysics “Francesco Lucchin” and GREAT-ITN, 11-15 June 2012, Teramo, Italy

- International conference “Variable Stars - 2010", August 2010, Odessa, Ukraine (**Talk**)

- III, IV International conference “Astronomy in XXI century", May 2010, 2011, Niepolomice, Poland (**Talk**)

- 36th International student conference “Physics of Space", 29 Jan – 2 Feb 2007, Yekaterinburg, Russia (**Talk**)

Seminars

- IAASARS, National Observatory of Athens, 13 January 2016, Athens, Greece (**Seminar**)

- Carnegie Observatories, 31 July 2015, Pasadena, California, US (**Lunch Talk**)

- IPAC, California Institute of Technology, 29 July 2015, Pasadena, California, US (**Lunch Talk**)

- University of Bologna, 7 November 2013, Bologna, Italy (**Seminar**)

7.4 Acknowledgments

This work presented in this thesis was supported by the European Union (European Social Fund) and National Resources under the "ARISTEIA" action of the Operational Programme "Education and Lifelong Learning" in Greece.

I would like to gratefully and sincerely thank Alceste for the big support as Supervisor and the patient guidelines in everything. Thanks to all people of the National Observatory of Athens for their support, and warm hospitality during these 3 years, especially thanks to Stephen Williams, Michalis Kourniotis, Zoi Spetsieri, Ektoras Pouliasis, Maria Ida Moretti, Felice Cusano, Giorgio Lanzuisi and Letizia Cassara.

This is the main chapter of a story how Eugene Britavskiy and I for the first time looked through a telescope at the sky in the year 2000. Thanks to my family (specially to my mother for my first telescope) and friends for being always around.

7.5 MATLAB routine

Algorithm for calculating extinction across the optical and near-IR wavelengths (Cardelli et al. 1989).

```
% Calculating of the extinction in optical range (0.3 \mu m -- 1.1 \mu m)
function Afv=reddening_test_Opt(wave,Av,Rv)

lam=wave./10000;
x=1./lam;

    y=x-1.82;

    a=1+0.17699.*y - 0.50447.*(y.^2) - 0.02427.*(y.^3) + 0.72085.*(y.^4) + 0.01979.*(y.^5) - 0.77530.*(y.^6) + 0.32999.*(y.^7);
    b=1.41338.*y + 2.28305.*(y.^2) + 1.07233.*(y.^3) - 5.38434.*(y.^4) - 0.62251.*(y.^5) + 5.30260.*(y.^6) - 2.09002.*(y.^7);

Afv=Av.*(a + b./Rv);


% Calculation of the extinction in near-IR range (1.1 \mu m -- 3.3 \mu m)

function Afv=reddening_test_IR(wave,Av,Rv)

lam=wave./10000;
x=1./lam;

    a=0.574.*(x.^(1.61));
    b=-0.527.*(x.^(1.61));

 Afv=Av.*(a + b./Rv);
```

Script 1

```
function [T2err,R2Err,EBV2err,RV2err,Av2err,temp_str]=RSG_SED_degrade_without(marcs_sed)

c=2.9979E+18;  %              # Light speed in Angstroms/sec
kpc=3.086E+21;  %             # Kpc in cm
Ro=6.96E+10;    %             # Solar radius in cm
con=4*pi;   %


abund=1; %%%   [Fe/H] = -1;
vturb=2; %%%   v_turb = 5;
gravs=1;

V=18.1;

J=14.199;    dJ=0.027;    H=13.507;    dH=0.025;    K=13.295;    dK=0.036;

B=18.771;
R=16.48;

fid = fopen('ic1613_4.txt', 'r');
a = fscanf(fid,'%f %f', [2 inf]);
a=a';
fclose(fid);
w_rsg1=a(:,1)+4;
R_rsg1=a(:,2);   %
%flux_obj=R_rsg1.*(1E-16); eso
flux_obj=R_rsg1;

object_photom(:,:)=[w_rsg1(19),flux_obj(19);  ...   %B
        w_rsg1(347),flux_obj(347);...               %V
        w_rsg1(1115),flux_obj(1115);];        %I


[flB,eflB]=flux(B,dB,-0.602);
[flV,eflV]=flux(V,dV,0);
[flI,eflI]=flux(I,dI,1.271);
[flJ,eflJ]=flux2MASS(J,dJ,1594*c/(12350^2));
[flH,eflH]=flux2MASS(H,dH,1024*c/(16620^2));
[flK,eflK]=flux2MASS(K,dK,666.7*c/(21590^2));

 photo=[4361,flB,eflB;...
    5448,flV,eflV;...
    7980,flI,eflI;...
    12350,flJ,eflJ;...
    16620,flH,eflH;...
    21590,flK,eflK];


D=755*kpc;  %Pegasus D=920;  %Pegasus D=920; %Pegasus D=920; sextans A = 1432; WLM=933 phoenix=415; Sex B=1426; IC1613 = 755

wave_sed=marcs_sed.wave_lo.*10;
```

```
R_test=[400:100:1400];
Rv=[1:0.2:6];
EBv=[0.1:0.3:2];
for t=1:50

spectrum_sed_flux=reshape(marcs_sed.fluxes(t,gravs,abund,vturb,:),11000,1);
temp_str(t,:)=degrade_spec_marcs(wave_sed,spectrum_sed_flux);

end



for e=1:11

for t=1:50
    for j=1:26

        for y=1:5
        spectrum_sed_IR=reshape(temp_str(t,3446:11000),7555,1).*10.^(-0.4.*reddening_test_IR(wave_sed(3446:11000),Rv(j)*EBv(y),Rv(j))).*
        ...*(((R_test(e)*Ro)./D)^2);
        spectrum_sed_Opt=reshape(temp_str(t,1:3445),3445,1).*10.^(-0.4.*reddening_test_Opt(wave_sed(1:3445),Rv(j)*EBv(y),Rv(j))).*
        ...*(((R_test(e)*Ro)./D)^2);
        spectrum_sed_test=[spectrum_sed_Opt;spectrum_sed_IR];

        vq = interp1(wave_sed,spectrum_sed_test,w_rsg1);



         marcs_photom(:,:)=[wave_sed(681),spectrum_sed_test(681);  ...    %B
         wave_sed(1225),spectrum_sed_test(1225);...                      %V
         wave_sed(2455),spectrum_sed_test(2455);...                      %I
         wave_sed(4676),spectrum_sed_test(4676);...                      %J
         wave_sed(6811),spectrum_sed_test(6811);...                      %H
         wave_sed(9296),spectrum_sed_test(9296);];
    razn(t,j,y)=sqrt(sum((((flux_obj(450:1870)-vq(450:1870))).^2)));

        end
      end

end

for y=1:5
    NewMatrix(:,:) = (razn(:,:,y));
    minMatrix(y) = min(NewMatrix(:));
    [Atemp(y),ARv_in(y)] = find(NewMatrix==minMatrix(y));
    AbsMinMatr(y)=NewMatrix(Atemp(y),ARv_in(y));
end
    [ABSMinEBV,indexABS(e)]=min(AbsMinMatr);

FinalEBV(e)=EBv(indexABS(e));

NewMatrixFINEB(:,:) = (razn(:,:,indexABS(e)));
minMatrixFINEB(e) = min(NewMatrixFINEB(:));
[temp(e),Rv_in(e)] = find(NewMatrixFINEB==minMatrixFINEB(e));
T(e)=marcs_sed.params.temps(temp(e));

Rv_fin(e)=Rv(Rv_in(e);
```

```
figure1 = figure('PaperType','a4letter','PaperSize',[30.98 39.68]);

axes('Parent',figure1,'FontSize',14);

annotation(figure1,'textbox',...
    [0.035871156661786 0.826032280027234 0.0661786237188872 0.0899108313663783],...
    'String',{'R = ' R_test(e),'Rv=' Rv_fin(e)},...
    'FitBoxToText','off',...
    'LineStyle','none');

 xlim([0.5 6.4]);

 ylim([3380 4400]);
box('on');
hold('all');
contour3(Rv(1:26),marcs_sed.params.temps(1:50),NewMatrixFINEB,30);

plot3(Rv_fin(e),T(e),minMatrixFINEB(e),'X','MarkerSize',15,'Marker','x','LineWidth',2,'LineStyle','none','Color',[0.8 0.8 0.8]);


xlabel('Rv','FontSize',16);
ylabel('T_{eff}','FontSize',16);


set(gcf,'InvertHardcopy','on');
set(gcf,'PaperUnits', 'inches');
papersize = get(gcf, 'PaperSize');

myfiguresize = [0.1, 0.1, 4.58, 4.28];
set(gcf,'PaperPosition', myfiguresize);

% Save the file as PNG
name=num2str(R_test(e));

name_fin = ['Contour R = ' name];
hgexport(gcf, name_fin, hgexport('factorystyle'), 'Format', 'png');

spectrum_sed_IR=reshape(temp_str(temp(e),3446:11000),7555,1).*
...*10.^(-0.4.*reddening_test_IR(wave_sed(3446:11000),Rv_fin(e).*FinalEBV(e),Rv_fin(e))).*
    ...*(((R_test(e)*Ro)./D)^2);
spectrum_sed_Opt=reshape(temp_str(temp(e),1:3445),3445,1).*
...*10.^(-0.4.*reddening_test_Opt(wave_sed(1:3445),Rv_fin(e).*FinalEBV(e),Rv_fin(e))).*
    ...*(((R_test(e)*Ro)./D)^2);
spectrum_sed_t=[spectrum_sed_Opt;spectrum_sed_IR];

vq_t = interp1(wave_sed,spectrum_sed_t,w_rsg1);


figure2 = figure('PaperType','a4letter','PaperSize',[40.98 59.68]);

axes2 = axes('Parent',figure2,'XScale','log','XMinorTick','on',...
    'Position',[0.13 0.149289099526066 0.775 0.772511848341232],...
    'FontSize',12);
```

```
xlim(axes2,[3710.32084904897 23505.1933201674]);
ylim(axes2,[-0.50575925672911e-17 0.45519712941E-15]);

R_text=num2str(R_test(e));
Av_text= num2str(Rv_fin(e).*FinalEBV(e));
RV_text=num2str(Rv_fin(e));
delta_text=num2str(minMatrixFINEB(e));
T_text=num2str(T(e));
string_anot = ['R = ' R_text, ' T_{eff} = ' T_text, ' Av = ' Av_text, ' Rv = ' RV_text, ' Delta= ' delta_text];

annotation(figure2,'textbox',...
    [0.146339677891654 0.1165391924696317 0.635651537335286 0.0999108313663783],...
    'String',{string_anot},...
    'FitBoxToText','off',...
    'LineStyle','none');


box('on');
hold('all');
hh = ploterr(photo(:,1), photo(:,2), [], photo(:,3));
set(hh(2),'LineWidth',1,'Color',[0.502 0.502 0.502]);
set(hh(1),'LineStyle','none');

h1=plot(wave_sed,spectrum_sed_t,'-','LineWidth',0.5,'Color',[1 0 0]);
h2=plot(w_rsg1,flux_obj,'-','LineWidth',0.5,'Color',[0 0 0]);
h3=plot(4361,flB,'o','MarkerSize',10,'LineWidth',3);
h4=plot(5448,flV,'o','MarkerSize',10,'LineWidth',3,'LineStyle','none','Color',[0 0.498 0]);
h5=plot(7980,flI,'o','MarkerSize',10,'LineWidth',3,'LineStyle','none','Color',[0 0.749 0.749]);
h6=plot(12350,flJ,'o','MarkerSize',10,'LineWidth',3,'LineStyle','none','Color',[0.749 0.749 0]);
h7=plot(16620,flH,'o','MarkerSize',10,'LineWidth',3,'LineStyle','none','Color',[1 0 1]);
h8=plot(21590,flK,'o','MarkerSize',10,'LineWidth',3,'LineStyle','none','Color',[0.8549 0.702 1]);
legend([h1,h2,h3,h4,h5,h6,h7,h8],'MARCS Grid','SED Pegasus 1','B','V','I','J','H','K');

xlabel('Wavelength (A)','FontSize',14);
ylabel('Flux (ergs/cm^2/sec/A)','FontSize',14);

name=num2str(R_test(e));
name_fin = ['SED, R = ' name];

end

figure4 = figure('PaperType','a4letter','PaperSize',[30.98 39.68]);

plot(R_test(:),minMatrixFINEB(:),'.');
xlabel('R_{Sun}','FontSize',14);
ylabel('\chi^{2}','FontSize',14);
set(gcf,'InvertHardcopy','on');
set(gcf,'PaperUnits', 'inches');
papersize = get(gcf, 'PaperSize');

myfiguresize = [0.1, 0.1, 4.58, 4.28];
set(gcf,'PaperPosition', myfiguresize);
% Save the file as PNG
name_fin = ['R_{fin}= '];
%saveas(gcf,name_fin,'png');
```

```
%print(name_fin,'-dpdf','-r1400');
hgexport(gcf, name_fin, hgexport('factorystyle'), 'Format', 'png');

[value_good,index_good]=min(minMatrixFINEB(1:end-2));

R2Err=R_test(index_good);
EBV2err=FinalEBV(index_good);
RV2err=Rv_fin(index_good);
T2err=T(index_good);
Av2err=FinalEBV(index_good).*Rv_fin(index_good);
```

Script 2

```
function [T_final,Tsigma,Av_final,Av_sigma,Rv]=RSG_test_test_test(marcs_sed,R2Err,EBV2err,temp_str)

c=2.9979E+18;  %              # Light speed in Angstroms/sec
kpc=3.086E+21;  %             # Kpc in cm
Ro=6.96E+10;      %           # Solar radius in cm
con=4*pi;   %

%RSG8_sexa
V=19.935;
B=21.521; dB=0.086;
R=19.122; dV=0.086;
I=18.347; dI=0.009;
J=15.758;       dJ=0.058;
H=14.898;       dH=0.069;
K=14.896;       dK=0.139;
%

fid = fopen('RSG_8v1_2.txt', 'r'); %
a = fscanf(fid,'%f_%f', [2 inf]);
a=a';
fclose(fid);
w_rsg1=a(:,1)-8;   %
R_rsg1=a(:,2);    %
flux_obj=R_rsg1.*(1E-16).*1.6; %eso
%flux_obj=R_rsg1; ic1613


object_photom(:,:)=[w_rsg1(19),flux_obj(19); ...   %B
         w_rsg1(347),flux_obj(347);...              %V
         w_rsg1(1115),flux_obj(1115);];              %I


[flB,eflB]=flux(B,dB,-0.602);
[flV,eflV]=flux(V,dV,0);
[flI,eflI]=flux(I,dI,1.271);
[flJ,eflJ]=flux2MASS(J,dJ,1594*c/(12350^2));
[flH,eflH]=flux2MASS(H,dH,1024*c/(16620^2));
[flK,eflK]=flux2MASS(K,dK,666.7*c/(21590^2));

 photo=[4361,flB,eflB;...
    5448,flV,eflV;...
    7980,flI,eflI;...
    12350,flJ,eflJ;...
    16620,flH,eflH;...
    21590,flK,eflK];


D=1432*kpc;   %Pegasus D=920; sextans A = 1432; WLM=933 phoenix=415; Sex B=1426; IC = 755

Av_test=[0.1:0.1:6];
wave_sed=marcs_sed.wave_lo.*10;
Ebvn=normrnd(EBV2err,0.03,[1,10]);
```

```
R_fin_n=normrnd(R2Err,40,[1,10]);


for e=1:10

for t=1:50
    for j=1:60


spectrum_sed_IR=reshape(temp_str(t,3446:11000),7555,1).*
...*10.^(-0.4.*reddening_test_IR(wave_sed(3446:11000),Av_test(j),Av_test(j)./Ebvn(e))).*
       ...*(((R_fin_n(e)*Ro)./D)^2);
spectrum_sed_Opt=reshape(temp_str(t,1:3445),3445,1).*
...*10.^(-0.4.*reddening_test_Opt(wave_sed(1:3445),Av_test(j),Av_test(j)./Ebvn(e))).*
       ...*(((R_fin_n(e)*Ro)./D)^2);
spectrum_sed_test=[spectrum_sed_Opt;spectrum_sed_IR];




       vq = interp1(wave_sed,spectrum_sed_test,w_rsg1);

      marcs_photom(:,:)=[wave_sed(681),spectrum_sed_test(681); ...   %B
        wave_sed(1225),spectrum_sed_test(1225);...                  %V
        wave_sed(2455),spectrum_sed_test(2455);...                  %I
        wave_sed(4676),spectrum_sed_test(4676);...                  %J
        wave_sed(6811),spectrum_sed_test(6811);...                  %H
        wave_sed(9296),spectrum_sed_test(9296);];

    razn(t,j)=sqrt(sum((abs(flux_obj(1:967)-vq(1:967))).^2));
    end

end
minMatrix = min(razn(:));
[temp,Av] = find(razn==minMatrix);
T(e)=marcs_sed.params.temps(temp);
Av_fin(e)=Av_test(Av);

end

T_final=mean(T(:));
Av_final=mean(Av_fin(:));

Tsigma=std(T(:));
Av_sigma=std(Av_fin(:));

f = marcs_sed.params.temps(:);
[c index] = min(abs(f-T_final));
T_str_fin = f(index); % Finds first one only!

Rv=Av_final./EBV2err;
```

```
for t=1:50
    for j=1:60

        spectrum_sed_IR=reshape(temp_str(t,3446:11000),7555,1).*
        ...*10.^(-0.4.*reddening_test_IR(wave_sed(3446:11000),Av_test(j),Av_test(j)./EBV2err)).*(((R2Err*Ro)./D)^2);
        spectrum_sed_Opt=reshape(temp_str(t,1:3445),3445,1).*
        ...*10.^(-0.4.*reddening_test_Opt(wave_sed(1:3445),Av_test(j),Av_test(j)./EBV2err)).*(((R2Err*Ro)./D)^2);
        spectrum_sed_test=[spectrum_sed_Opt;spectrum_sed_IR];

        vq = interp1(wave_sed,spectrum_sed_test,w_rsg1);

    marcs_photom(:,:)=[wave_sed(681),spectrum_sed_test(681);  ...    %B
         wave_sed(1225),spectrum_sed_test(1225);...                  %V
         wave_sed(2455),spectrum_sed_test(2455);...                  %I
         wave_sed(4676),spectrum_sed_test(4676);...                  %J
         wave_sed(6811),spectrum_sed_test(6811);...                  %H
         wave_sed(9296),spectrum_sed_test(9296);];

   razn_photo(t,j)=sqrt(sum((abs(flux_obj(1:967)-vq(1:967))).^2)); % eso
    %razn_photo(t,j)=sqrt(sum((abs(flux_obj(450:1870)-vq(450:1870))).^2));    ic1613

    end

end



  spectrum_sed_IR=reshape(temp_str(index,3446:11000),7555,1).*
  ...*10.^(-0.4.*reddening_test_IR(wave_sed(3446:11000),Av_final,Av_final./EBV2err)).*(((R2Err*Ro)./D)^2);
  spectrum_sed_Opt=reshape(temp_str(index,1:3445),3445,1).*
  ...*10.^(-0.4.*reddening_test_Opt(wave_sed(1:3445),Av_final,Av_final./EBV2err)).*(((R2Err*Ro)./D)^2);
  spectrum_sed_t=[spectrum_sed_Opt;spectrum_sed_IR];



vq_t = interp1(wave_sed,spectrum_sed_t,w_rsg1);



figure1 = figure('PaperType','a4letter','PaperSize',[20.98 29.68]);

axes('Parent',figure1,'FontSize',14);
 xlim([0.0 3]);

 ylim([3380 4400]);
box('on');
hold('all');

contour3(Av_test(1:60),marcs_sed.params.temps(1:50),razn_photo,30);
plot3(Av_final,T_final,minMatrix,'X','MarkerSize',15,'Marker','x','LineWidth',2,'LineStyle','none','Color',[0.8 0.8 0.8]);

hh = ploterr(Av_final, T_final, Av_sigma, Tsigma);
set(hh(:),'LineWidth',2,'Color',[0.502 0.502 0.502]);

xlabel('Av','FontSize',16);
```

```
ylabel('T_{eff}','FontSize',16);




figure2 = figure('PaperSize',[20.98 29.68]);
axes('Parent',figure2,'FontSize',16,'YScale','log','YMinorTick','on','XScale','log');


box('on');
hold('all');

hh = ploterr(photo(:,1), photo(:,2), [], photo(:,3));
set(hh(2),'LineWidth',2,'Color',[0.502 0.502 0.502]);

h1=plot(wave_sed,spectrum_sed_t,'-','LineWidth',1,'Color',[1 0 0]);
h2=plot(w_rsg1,flux_obj,'-','LineWidth',1,'Color',[0 0 0]);
h3=plot(4361,flB,'o','MarkerSize',10,'LineWidth',3);
h4=plot(5448,flV,'o','MarkerSize',10,'LineWidth',3,'LineStyle','none','Color',[0 0.498 0]);
h5=plot(7980,flI,'o','MarkerSize',10,'LineWidth',3,'LineStyle','none','Color',[0 0.749 0.749]);
h6=plot(12350,flJ,'o','MarkerSize',10,'LineWidth',3,'LineStyle','none','Color',[0.749 0.749 0]);
h7=plot(16620,flH,'o','MarkerSize',10,'LineWidth',3,'LineStyle','none','Color',[1 0 1]);
h8=plot(21590,flK,'o','MarkerSize',10,'LineWidth',3,'LineStyle','none','Color',[0.8549 0.702 1]);
legend([h1,h2,h3,h4,h5,h6,h7,h8],'MARCS Grid','SED Pegasus 1','B','V','I','J','H','K');

xlabel('Wavelength (A)','FontSize',16);
ylabel('Flux (ergs/cm^2/sec/A)','FontSize',16);
```

Bibliography

Adams, S. M., Kochanek, C. S., Prieto, J. L., et al. 2015, MNRAS, submitted (arXiv:1511.07393)

Ahn, C. P., Alexandroff, R., Allende Prieto, C., et al. 2012, Astrop. J. Supp. , 203, 21

Allen, D. A. & Swings, J. P. 1972, A&A , 10, 83

Allen, D. A. & Swings, J. P. 1976, A&A , 47, 293

Bagnulo, S., Jehin, E., Ledoux, C., et al. 2003, The Messenger, 114, 10

Banerjee, S., Kroupa, P., & Oh, S. 2012, ApJ , 746, 15

Battinelli, P. & Demers, S. 2000, AJ , 120, 1801

Battinelli, P. & Demers, S. 2004, A&A , 416, 111

Bonanos, A. Z., Lennon, D. J., Köhlinger, F., et al. 2010, AJ , 140, 416

Bonanos, A. Z., Massa, D. L., Sewilo, M., et al. 2009, AJ , 138, 1003

Bonanos, A. Z., Stanek, K. Z., Kudritzki, R. P., et al. 2006, ApJ , 652, 313

Bond, H. E., Bedin, L. R., Bonanos, A. Z., et al. 2009, ApJL , 695, L154

Boyer, M. L., McQuinn, K. B. W., Barmby, P., et al. 2015a, ApJ , 800, 51

Boyer, M. L., McQuinn, K. B. W., Barmby, P., et al. 2015b, Astrop. J. Supp. , 216, 10

Boyer, M. L., Skillman, E. D., van Loon, J. T., Gehrz, R. D., & Woodward, C. E. 2009, ApJ , 697, 1993

Britavskiy, N. E., Bonanos, A. Z., Mehner, A., Boyer, M. L., & McQuinn, K. B. W. 2015, A&A , 584, A33

Britavskiy, N. E., Bonanos, A. Z., Mehner, A., et al. 2014, A&A , 562, A75

Brott, I., de Mink, S. E., Cantiello, M., et al. 2011, A&A , 530, A115

Buchanan, C. L., Kastner, J. H., Forrest, W. J., et al. 2006, AJ , 132, 1890

Cardelli, J. A., Clayton, G. C., & Mathis, J. S. 1989, ApJ , 345, 245

Cardiel, N. 2010, indexf: Line-strength Indices in Fully Calibrated FITS Spectra, astrophysics Source Code Library

Cenarro, A. J., Cardiel, N., Gorgas, J., et al. 2001, MNRAS , 326, 959

Cenarro, A. J., Gorgas, J., Cardiel, N., Vazdekis, A., & Peletier, R. F. 2002, MNRAS , 329, 863

Chentsov, E. L., Ermakov, S. V., Klochkova, V. G., et al. 2003, A&A , 397, 1035

Clark, J. S., Castro, N., Garcia, M., et al. 2012, A&A , 541, A146

Conti, P. S. 1984, in IAU Symposium, Vol. 105, Observational Tests of the Stellar Evolution Theory, ed. A. Maeder & A. Renzini, 233

Crowther, P. A. 2007, ARA&A, 45, 177

Crowther, P. A., Schnurr, O., Hirschi, R., et al. 2010, MNRAS , 408, 731

Danchi, W. C., Bester, M., Degiacomi, C. G., Greenhill, L. J., & Townes, C. H. 1994, AJ , 107, 1469

Danielson, R. E., Woolf, N. J., & Gaustad, J. E. 1965, ApJ , 141, 116

Davies, B., Kudritzki, R.-P., Gazak, Z., et al. 2015, ApJ , 806, 21

Davies, B., Kudritzki, R.-P., Plez, B., et al. 2013, ApJ , 767, 3

Dolphin, A. E., Saha, A., Skillman, E. D., et al. 2003, AJ , 125, 1261

Dolphin, A. E., Saha, A., Skillman, E. D., et al. 2001, ApJ , 550, 554

Drout, M. R., Massey, P., & Meynet, G. 2012, ApJ , 750, 97

Ekström, S., Georgy, C., Eggenberger, P., et al. 2012, A&A , 537, A146

Elias, J. H., Frogel, J. A., & Humphreys, R. M. 1985, Astrop. J. Supp. , 57, 91

Evans, C. J., Barbuy, B., Bonifacio, P., et al. 2012, in Society of Photo-Optical Instrumentation Engineers (SPIE) Conference Series, Vol. 8446, Society of Photo-Optical Instrumentation Engineers (SPIE) Conference Series, 7

Figer, D. F. 2005, Nature , 434, 192

Fox, O. D., Filippenko, A. V., Skrutskie, M. F., et al. 2013, AJ , 146, 2

Freudling, W., Romaniello, M., Bramich, D. M., et al. 2013, A&A , 559, A96

Fullerton, A. W., Massa, D. L., Prinja, R. K., et al. 2006, in Astronomical Society of the Pacific Conference Series, Vol. 348, Astrophysics in the Far Ultraviolet: Five Years of Discovery with FUSE, ed. G. Sonneborn, H. W. Moos, & B.-G. Andersson, 130

Gallart, C., Martínez-Delgado, D., Gómez-Flechoso, M. A., & Mateo, M. 2001, AJ , 121, 2572

Garcia, M., Herrero, A., Vicente, B., et al. 2009, A&A , 502, 1015

Garcia-Berro, E. & Iben, I. 1994, ApJ , 434, 306

García-Hernández, D. A., Zamora, O., Yagüe, A., et al. 2013, A&A , 555, L3

Gazak, J. Z., Kudritzki, R., Evans, C., et al. 2015, ApJ , 805, 182

Georgy, C., Ekström, S., Meynet, G., et al. 2012, A&A , 542, A29

Ginestet, N., Carquillat, J. M., Jaschek, M., & Jaschek, C. 1994, A&A Supp. , 108, 359

González-Fernández, C., Dorda, R., Negueruela, I., & Marco, A. 2015, A&A , 578, A3

Gustafsson, B., Edvardsson, B., Eriksson, K., et al. 2008, A&A , 486, 951

Hambly, N. C., MacGillivray, H. T., Read, M. A., et al. 2001, MNRAS , 326, 1279

Herwig, F. 2005, ARA&A, 43, 435

Hodge, P. & Miller, B. W. 1995, ApJ , 451, 176

Hodge, P. W., Dolphin, A. E., Smith, T. R., & Mateo, M. 1999, ApJ , 521, 577

Humphreys, R. M. & Davidson, K. 1994, PASP , 106, 1025

Humphreys, R. M., Weis, K., Davidson, K., Bomans, D. J., & Burggraf, B. 2014, ApJ , 790, 48

Ivezic, Z., Nenkova, M., & Elitzur, M. 1999, DUSTY: Radiation transport in a dusty environment, Astrophysics Source Code Library

Jaeger, C., Leitherer, C., & Chavarria, C. K. 1988, in Astrophysics and Space Science Library, Vol. 142, Mass Outflows from Stars and Galactic Nuclei, ed. L. Bianchi & R. Gilmozzi, 223–226

Javadi, A., van Loon, J. T., & Mirtorabi, M. T. 2011, MNRAS , 411, 263

Johnson, H. L. 1967, ApJ , 149, 345

Kastner, J. H., Thorndike, S. L., Romanczyk, P. A., et al. 2008, AJ , 136, 1221

Keenan, P. C. 1993, PASP , 105, 905

Kennicutt, Jr., R. C., Armus, L., Bendo, G., et al. 2003, PASP , 115, 928

Khan, R., Stanek, K. Z., & Kochanek, C. S. 2013, ApJ , 767, 52

Khan, R., Stanek, K. Z., Kochanek, C. S., & Bonanos, A. Z. 2011, ApJ , 732, 43

Khan, R., Stanek, K. Z., Kochanek, C. S., & Sonneborn, G. 2015, Astrop. J. Supp. , 219, 42

Khan, R., Stanek, K. Z., Prieto, J. L., et al. 2010, ApJ , 715, 1094

Kiewe, M., Gal-Yam, A., Arcavi, I., et al. 2012, ApJ , 744, 10

Kondratiev, V., Lorimer, D., McLaughlin, M., & Ransom, S. 2013, in IAU Symposium, Vol. 291, IAU Symposium, ed. J. van Leeuwen, 431–431

Kourniotis, M., Bonanos, A. Z., Soszyński, I., et al. 2014, A&A , 562, A125

Kozłowski, S., Onken, C. A., Kochanek, C. S., et al. 2013, ApJ , 775, 92

Kraus, M., Borges Fernandes, M., & de Araújo, F. X. 2007, A&A , 463, 627

Kraus, M., Cidale, L. S., Arias, M. L., Oksala, M. E., & Borges Fernandes, M. 2014, ApJL , 780, L10

Kudritzki, R.-P. & Puls, J. 2000, ARA&A, 38, 613

Kurucz, R. 1993, ATLAS9 Stellar Atmosphere Programs and 2 km/s grid. Kurucz CD-ROM No. 13. Cambridge, Mass.: Smithsonian Astrophysical Observatory, 1993., 13

Kurucz, R. L. 1992, in IAU Symposium, Vol. 149, The Stellar Populations of Galaxies, ed. B. Barbuy & A. Renzini, 225

Langer, N., Hamann, W.-R., Lennon, M., et al. 1994, A&A , 290, 819

Lardo, C., Davies, B., Kudritzki, R.-P., et al. 2015, ApJ , 812, 160

Levesque, E. M. 2010, New A Rev., 54, 1

Levesque, E. M. 2013, in EAS Publications Series, Vol. 60, EAS Publications Series, ed. P. Kervella, T. Le Bertre, & G. Perrin, 269–277

Levesque, E. M. & Massey, P. 2012, AJ , 144, 2

Levesque, E. M., Massey, P., Olsen, K. A. G., et al. 2005, ApJ , 628, 973

Levesque, E. M., Massey, P., Olsen, K. A. G., et al. 2006, ApJ , 645, 1102

Martínez-Delgado, D., Gallart, C., & Aparicio, A. 1999, AJ , 118, 862

Massey, P. 1998, ApJ , 501, 153

Massey, P. 2002, Astrop. J. Supp. , 141, 81

Massey, P. 2003, ARA&A, 41, 15

Massey, P., Levesque, E. M., Olsen, K. A. G., Plez, B., & Skiff, B. A. 2007a, ApJ , 660, 301

Massey, P., McNeill, R. T., Olsen, K. A. G., et al. 2007b, AJ , 134, 2474

Massey, P. & Olsen, K. A. G. 2003, AJ , 126, 2867

Massey, P., Olsen, K. A. G., Hodge, P. W., et al. 2007c, AJ , 133, 2393

Massey, P., Olsen, K. A. G., Hodge, P. W., et al. 2007d, AJ , 133, 2393

Massey, P., Olsen, K. A. G., Hodge, P. W., et al. 2006, AJ , 131, 2478

Massey, P., Silva, D. R., Levesque, E. M., et al. 2009, ApJ , 703, 420

Mateo, M. L. 1998, ARA&A, 36, 435

Mauerhan, J. C., Smith, N., Filippenko, A. V., et al. 2013, MNRAS , 430, 1801

Mauron, N. & Josselin, E. 2011a, A&A , 526, A156

Mauron, N. & Josselin, E. 2011b, A&A , 526, A156

McConnachie, A. W. 2012, AJ , 144, 4

McQuinn, K. B. W., Woodward, C. E., Willner, S. P., et al. 2007, ApJ , 664, 850

Menzies, J., Feast, M., Whitelock, P., et al. 2008, MNRAS , 385, 1045

Messineo, M., Menten, K. M., Churchwell, E., & Habing, H. 2012, A&A , 537, A10

Negueruela, I., González-Fernández, C., Marco, A., & Clark, J. S. 2011, A&A , 528, A59

Negueruela, I., Marco, A., González-Fernández, C., et al. 2012a, A&A , 547, A15

Negueruela, I., Marco, A., González-Fernández, C., et al. 2012b, A&A , 547, A15

Neill, J. D., Sullivan, M., Gal-Yam, A., et al. 2011, ApJ , 727, 15

Neugent, K. F. & Massey, P. 2011, ApJ , 733, 123

Oey, M. S. & Clarke, C. J. 2005, ApJL , 620, L43

Ofek, E. O., Zoglauer, A., Boggs, S. E., et al. 2014, ApJ , 781, 42

Owocki, S. P. & Puls, J. 1999, ApJ , 510, 355

Pastorello, A., Cappellaro, E., Inserra, C., et al. 2013, ApJ , 767, 1

Patrick, L. R., Evans, C. J., Davies, B., et al. 2015, ApJ , 803, 14

Porter, J. M. 2003, A&A , 398, 631

Prieto, J. L., Kistler, M. D., Thompson, T. A., et al. 2008, ApJL , 681, L9

Przybilla, N., Butler, K., Becker, S. R., Kudritzki, R. P., & Venn, K. A. 2000, A&A , 359, 1085

Rayner, J. T., Cushing, M. C., & Vacca, W. D. 2009, Astrop. J. Supp. , 185, 289

Smith, N. 2014, ARA&A, 52, 487

Smith, N., Li, W., Foley, R. J., et al. 2007, ApJ , 666, 1116

Smith, N., Li, W., Miller, A. A., et al. 2011, ApJ , 732, 63

Smith, N., Mauerhan, J. C., Kasliwal, M. M., & Burgasser, A. J. 2013, MNRAS , 434, 2721

Smith, N. & Tombleson, R. 2015, MNRAS , 447, 598

Stanek, K. Z. & Garnavich, P. M. 1998, ApJL , 503, L131

Stoll, R., Prieto, J. L., Stanek, K. Z., et al. 2011, ApJ , 730, 34

Szczygieł, D. M., Stanek, K. Z., Bonanos, A. Z., et al. 2010, AJ , 140, 14

Thompson, T. A., Prieto, J. L., Stanek, K. Z., et al. 2009, ApJ , 705, 1364

Tolstoy, E. 1999, in IAU Symposium, Vol. 192, The Stellar Content of Local Group Galaxies, ed. P. Whitelock & R. Cannon, 218

van Loon, J. T., Marshall, J. R., & Zijlstra, A. A. 2005, A&A , 442, 597

Verhoelst, T., van der Zypen, N., Hony, S., et al. 2009, A&A , 498, 127

Williams, S. J., Bonanos, A. Z., Whitmore, B. C., Prieto, J. L., & Blair, W. P. 2015, A&A , 578, A100

Wood, P. R., Bessell, M. S., & Fox, M. W. 1983, ApJ , 272, 99

Zethson, T., Johansson, S., Hartman, H., & Gull, T. R. 2012, A&A , 540, A133

Zhang, T., Wang, X., Wu, C., et al. 2012, AJ , 144, 131

Zickgraf, F.-J. 1998, in Astrophysics and Space Science Library, Vol. 233, B[e] stars, ed. A. M. Hubert & C. Jaschek, 1

Zickgraf, F.-J., Wolf, B., Stahl, O., Leitherer, C., & Klare, G. 1985, A&A , 143, 421

Zsargó, J., Hillier, D. J., & Georgiev, L. N. 2008, A&A , 478, 543